

# Materials Advances

Accepted Manuscript

This article can be cited before page numbers have been issued, to do this please use: S. Kumar, P. Kaur, C. Hsu, M. A. Mustafa, J. Kaur, J. Rani and S. Kaushal, *Mater. Adv.*, 2025, DOI: 10.1039/D5MA00494B.



This is an Accepted Manuscript, which has been through the Royal Society of Chemistry peer review process and has been accepted for publication.

Accepted Manuscripts are published online shortly after acceptance, before technical editing, formatting and proof reading. Using this free service, authors can make their results available to the community, in citable form, before we publish the edited article. We will replace this Accepted Manuscript with the edited and formatted Advance Article as soon as it is available.

You can find more information about Accepted Manuscripts in the [Information for Authors](#).

Please note that technical editing may introduce minor changes to the text and/or graphics, which may alter content. The journal's standard [Terms & Conditions](#) and the [Ethical guidelines](#) still apply. In no event shall the Royal Society of Chemistry be held responsible for any errors or omissions in this Accepted Manuscript or any consequences arising from the use of any information it contains.

# 1 Advances in Surface Modification of Biomass and its Nanostructuring for Enhanced 2 Environmental Remediation Applications

3 Sandeep Kumar<sup>a\*</sup>, Parminder Kaur<sup>a,f</sup>, Chou-Yi Hsu<sup>b,c</sup>, Mohammed Ahmed Mustafa<sup>d</sup>, Jyoti Rani<sup>a</sup>, Jasmeen  
4 Kaur<sup>a</sup>, Sandeep Kaushal<sup>e\*\*</sup>

5 <sup>a</sup>Department of Chemistry, Akal University, Talwandi Sabo, Bathinda-151302, Punjab, India.

6 <sup>b</sup>Department of Pharmacy, Chia Nan University of Pharmacy and Science, Tainan City 71710, Taiwan

7 <sup>c</sup>Thunderbird School of Global Management, Arizona State University Tempe Campus, Phoenix, Arizona 85004,  
8 USA.

9 <sup>d</sup>Department of Medical Laboratory Technology, University of Imam Jaafar AL-Sadiq, Iraq.

10 <sup>e</sup>Regional Institute of Education, National Council of Educational Research and Training, Ajmer, Rajasthan, India.

11 <sup>f</sup>Department of Chemistry, Guru Kanshi University, Talwandi Sabo, Bathinda-151302, Punjab, India.

## 13 Corresponding Author:

14 **\*Corresponding Author:** Sandeep Kumar, Email: sandeepchem83@gmail.com (Sandeep Kumar); Department of  
15 Chemistry, Akal University, Talwandi Sabo, Bathinda-151302, Punjab, India.

16 **\*\*Corresponding Author:** Sandeep Kaushal, Email: kaushalsandeep33@gmail.com (Sandeep Kaushal); Regional  
17 Institute of Education, National Council of Educational Research and Training, Ajmer, Rajasthan, India

## 19 Overview:

- 20 1. Introduction:
- 21 2. Surface modification techniques for biomass
  - 22 2.1. Physical modification
    - 23 2.1.1. Pretreatment of biomass
    - 24 2.1.2. Pyrolysis of biomass
    - 25 2.1.3. Hydrothermal carbonization
    - 26 2.1.4. Microwave heating
  - 27 2.2. Chemical modification
    - 28 2.2.1. Acid modification of biomass
    - 29 2.2.2. Alkaline modification of biomass
  - 30 2.3. Physico-chemical activation of biomass
  - 31 2.4. Nanostructuring of biomass and its derivatives.
  - 32 2.5 Comparative analysis of surface modification techniques
- 33 3. Structure of biomass adsorbents
- 34 4. Characterization techniques for biomass and its derived materials
- 35 5. Mechanism involved in contaminant removal
  - 36 5.1. Adsorptive removal
  - 37 5.2 Degradative removal
  - 38 5.3. Synergy between adsorption and degradation mechanism
- 39 6. Environmental remediation application of biomass and its surface modified derivative
  - 40 6.1 Raw biomass as environmental remediation agent
  - 41 6.2 Surface modified biomass as environmental remediation agent
    - 42 6.2.1. Physical modified biomass
    - 43 6.2.2. Chemical modified biomass
    - 44 6.2.3. Physico-chemical modified biomass
    - 45 6.2.4 Nanostructured biomass
      - 46 6.2.4.1. Raw biomass with immobilized metal/metal oxide nanoparticles



- 47 6.2.4.2. Surface modified biomass with immobilized metal/metal oxide nanoparticles  
48 6.3. Reusability and Stability of Modified Biomass Materials  
49 6.4. Economic Viability and Scalability of Biomass Modification Techniques  
50 6.5 Real-World and Pilot-Scale Applications of Surface-Modified and Nanostructured Biomass in  
51 Environmental Remediation  
52 7. Future Prospective  
53 8. Conclusion  
54  
55

56 **Abstract:**

57 The growing concerns over environmental pollution and resource sustainability have encouraged  
58 considerable interest in valorizing biomass waste as functional materials for environmental  
59 remediation. Owing to its abundance, renewability, and diverse surface functionalities,  
60 lignocellulosic biomass holds immense potential as a cost-effective adsorbent and a catalyst.  
61 However, its practical application is hindered by limitations such as low surface area, limited  
62 porosity, and insufficient reactive sites. This review systematically compiles, and critically  
63 analyzes the recent advances in surface modification, and nanostructuring strategies aimed at  
64 enhancing the physicochemical properties of biomass-derived materials for water and wastewater  
65 treatment. The article covers a broad spectrum of modification approaches, including physical  
66 (pyrolysis, hydrothermal carbonization, microwave heating), chemical (acid/alkali activation,  
67 oxidative treatments), and physicochemical techniques, alongside emerging nanocomposite  
68 fabrication methods involving metal and metal oxide nanoparticle immobilization. Key focus is  
69 placed on how these modifications improve surface area, porosity, functional group distribution,  
70 and catalytic activity, thereby augmenting the adsorption and degradation capacities of biomass  
71 materials. Mechanistic insights into contaminant removal processes - adsorptive, degradative, and  
72 synergistic pathways are elaborated, thus correlating material properties with their pollutant  
73 removal efficiencies. Additionally, the review outlines the characterization techniques essential  
74 for evaluating structural, morphological, and surface chemistry alterations in modified biomass  
75 materials. By bridging fragmented literature and integrating mechanistic perspectives with  
76 material design principles, this review highlights the potential of engineered biomass-based  
77 materials as sustainable alternatives for environmental remediation. It also identifies research gaps,  
78 proposing future directions focused on scalable, eco-friendly modification techniques,  
79 performance optimization, and comprehensive environmental impact assessments. This work  
80 aspires to guide the development of next-generation biomass-derived materials for advanced,  
81 sustainable, and economically viable pollutant remediation technologies.



82

83 **Keywords:** Biomass; surface modification techniques; environmental remediation; sustainable  
84 materials; activated carbon; biochar.

85

### 86 **1. Introduction:**

87 Biomass refers to organic matter derived from living organisms, such as plants, animals,  
88 and microorganisms (Fantini, 2017). Examples of biomass include wood, agricultural residues,  
89 animal manure, and organic waste (**Figure 1**). It serves as a renewable energy source that can be  
90 utilized through various processes like combustion, fermentation, and conversion into biofuels  
91 (e.g., ethanol, biodiesel), and other bioproducts. The renewable aspect of biomass lies in its ability  
92 to be replenished relatively quickly compared to fossil fuels, which take millions of years to form  
93 (Amjith & Bavanish, 2022). The substantial quantities of agro-waste pose significant challenges  
94 to effective waste management practices (Phiri et al., 2024). Burning of the crop residues is a  
95 common practice that results in the non-recovery of potential resources and releasing greenhouse  
96 gasses and air pollutants. The crop residues are estimated to contain 80% nitrogen (N), 25%  
97 phosphorus (P), 50% sulfur (S), and 20% potassium (K), all of which are lost during burning  
98 (Bhuyan & Ahmaruzzaman, 2023). Treating biomass as waste can have significant environmental,  
99 economic, social, and sustainability implications. The utilization of biomass offers numerous  
100 environmental advantages, including reducing greenhouse gas emissions, promoting waste  
101 reduction and recycling, and providing an alternative to fossil fuels (Antar et al., 2021). The  
102 implementation of effective waste management strategies that prioritize resource recovery,  
103 recycling, and utilization of biomass can help mitigate these impacts and promote a more  
104 sustainable approach to biomass management (Wan et al., 2019).





105

106 **Figure 1.** Renewable sources of biomass.

107 The waste biomass may act as a clean, sustainable, and renewable energy source that can  
 108 be used as potential resources for converting into valuable products for their use in removing  
 109 pollutants from soil and water. The majority of adsorbents are derived from agricultural sources  
 110 such as leaves, bark, seeds, fruit peels, flowers, fish scales, algae, bacteria, and fungi.  
 111 Lignocellulosic agro-waste is the most abundant renewable energy resource, with additional  
 112 agronomic and environmental applications (S. Mishra et al., 2021). Agricultural biomass residues  
 113 have a similar composition to other lignocellulosic materials, with cellulose (40-50%),  
 114 hemicellulose (20-30%), lignin (20-25%), and ash (1-5%) (Mujtaba et al., 2023). Lignin is an  
 115 aromatic polymer containing various functionalities such as carbonyl (-CO-), hydroxyl (-OH), and  
 116 methyl (-CH<sub>3</sub>) groups etc. Hemicellulose and cellulose are aliphatic compounds with carbonyl,  
 117 hydroxyl, and ether functionalities as a part of their polymeric structure. These functional groups  
 118 contain oxygen atoms, which have a strong tendency to bind positively charged heavy metal ions  
 119 and small organic contaminants by different physical interactions such as hydrogen bonding,



120 electrostatic, or van der Waals interactions (Y. Zhou et al., 2015). Thus, using agricultural waste  
121 for environmental remediation is a beneficial and cost-effective process.

122 Agricultural biomass, derived from various agricultural sources, possesses distinct  
123 characteristics that differentiate it from conventional adsorbents commonly used in environmental  
124 remediation processes. These characteristics include a relatively lower surface area, pore size, and  
125 pore volume compared to traditional adsorbents like activated carbon or zeolites. The lesser  
126 surface area, pore size, and pore volume of agricultural biomass limit its adsorption capacity and  
127 efficiency in removing pollutants from contaminated water or soil (Gale et al., 2021). Adsorption,  
128 a process where contaminants are physically or chemically bound to the surface of the adsorbent  
129 material, relies on the availability of active sites and pore structures for effective pollutant removal  
130 (Nayak et al., 2024). With agricultural biomass having inherently smaller surface area and fewer  
131 pores, its adsorption capacity may be insufficient for efficient pollutant removal, especially for  
132 contaminants present in high concentrations or requiring specific adsorption conditions (Kainth et  
133 al., 2024). To overcome these limitations and harness the potential of agricultural biomass as  
134 adsorbents for environmental remediation, innovative strategies need to be developed. These  
135 strategies may include:

136 *Surface Modification:* The chemical or physical treatments can be applied to agricultural  
137 biomass to enhance its surface properties, increase surface area, and create more active sites for  
138 adsorption. The adsorption performance of biomass can be improved by employing techniques  
139 such as impregnation, chemical activation, or thermal treatment that can modify the surface  
140 chemistry and morphology of biomass (S. Wu et al., 2022).

141 *Nanostructuring:* Incorporating nanomaterials, such as nanoparticles or nanocomposites,  
142 onto the surface of agricultural biomass can enhance its adsorption capacity and selectivity.  
143 Nanostructuring increases the surface area by introducing additional adsorption sites, thus  
144 facilitating the removal of a wide range of pollutants with higher efficiency (H. Han et al., 2019;  
145 Singh, 2023). Moreover, the nanostructured biomass also exhibits enhanced photocatalytic  
146 application for the removal of recalcitrant organic contaminants through Fenton-like  
147 heterogeneous processes (Kumar et al., 2022).

148 *Composite Materials:* Combining agricultural biomass with other adsorbent materials, such as  
149 activated carbon, clay minerals, or polymers, can create composite materials with synergistic



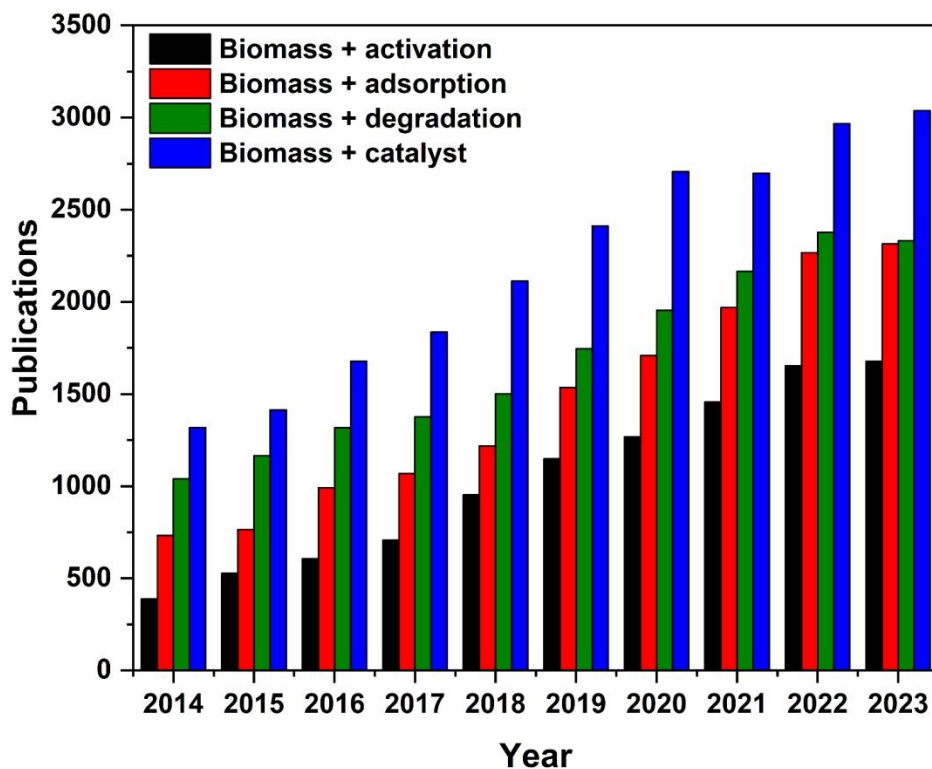
150 adsorption properties. These composite materials combine the strengths and advantages of both  
151 components, resulting in enhanced adsorption performance and versatility for environmental  
152 remediation applications (H. Han et al., 2019).

153 *Functionalization*: By introducing functional groups or chemical moieties onto the surface  
154 of agricultural biomass can modify its surface chemistry and improve its affinity towards specific  
155 pollutants (Rani et al., 2025a). The functionalization allows for targeted adsorption of  
156 contaminants, and enhances the selectivity and efficiency of agricultural biomass-based adsorbents  
157 (P. Zhang et al., 2022).

158 *Optimization of Operating Conditions*: Optimizing process parameters such as pH,  
159 temperature, contact time, and adsorbent dosage can maximize the adsorption efficiency of  
160 agricultural biomass-based adsorbents. By understanding the adsorption mechanisms and kinetics  
161 involved one can help tailor the operating conditions to achieve optimal pollutant removal  
162 performance (Abegunde et al., 2020).

163 By employing these strategies, agricultural biomass can be effectively utilized as  
164 adsorbents for environmental remediation processes, offering a sustainable and cost-effective  
165 solution for pollutant removal from water and soil environments. These advancements not only  
166 address the challenges associated with the inherent properties of agricultural biomass, but also  
167 contribute to the development of innovative and eco-friendly adsorption technologies for  
168 environmental protection and sustainability. Over the past decade, there has been a significant  
169 increase in interest within the research community towards the development of sustainable  
170 technologies for removing contaminants (**Figure 2**). However, existing literature reviews have  
171 predominantly focused either on the adsorptive removal of contaminants using biomass and its  
172 derivatives or on mere compiling the sustainable surface modification techniques, often neglecting  
173 the intricate structural changes within the biomass and its derived nanocomposites, and the  
174 underlying mechanisms of contaminant removal. In this comprehensive review, we provide an  
175 extensive discussion on surface modification techniques, elucidating the structural changes  
176 induced in biomass via various activation processes, while discussing the characterization  
177 techniques employed to analyse surface modifications, and the mechanisms underlying the  
178 contaminant removal. Moreover, we also provide a comprehensive summary of the diverse  
179 environmental remediation applications of biomass and its carbon-rich derivatives, offering a  
180 holistic perspective on the subject.





181

182 **Figure 2.** Research trend of contaminant remediation utilizing biomass-derived materials over the  
 183 past decade. (Searching keywords “biomass + activation; adsorption; degradation; and catalyst;  
 184 Source: Web of Science).

185 The sharp increase in publications after 2017 reflects several converging research trends. First, the  
 186 global emphasis on sustainable and low-cost materials for water and wastewater treatment  
 187 significantly raised the profile of biomass-derived carbons as eco-friendly alternatives to activated  
 188 carbon. Second, advancements in nanostructuring techniques enabled the integration of biomass  
 189 with metal and metal oxide nanoparticles, leading to multifunctional composites that combined  
 190 adsorption with catalytic degradation. Third, the introduction of persulfate- and  
 191 peroxymonosulfate-based advanced oxidation processes, often mediated by biochar or activated  
 192 carbon, opened new avenues for tackling recalcitrant organic contaminants. In parallel, the  
 193 expansion of photocatalytic and electrochemical approaches using biomass-derived supports  
 194 further drove research interest. Collectively, these innovations account for the steep rise in  
 195 scientific output observed after 2017.

196



## 197 2. Surface Modification Techniques for Lignocellulosic Biomass

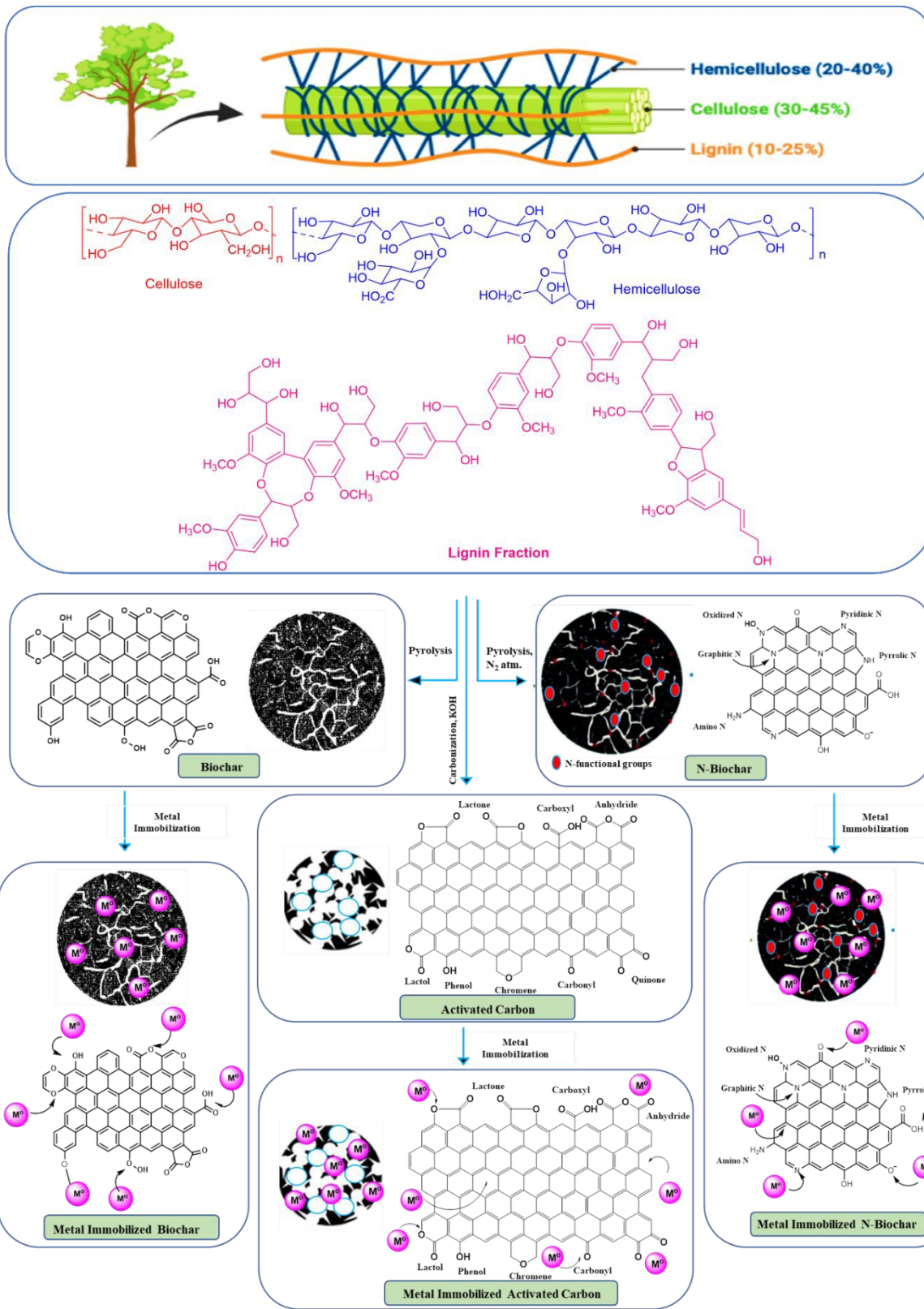
198 Surface modification techniques for biomass involve altering the surface properties of  
199 biomass materials to enhance their performance or functionality for specific applications. To  
200 improve its efficiency in wastewater treatments lignocellulose biomass can be modified with  
201 various physical and chemical treatments (**Figure 3**).

202  
203 **2.1. Physical modification of biomass:** Physical methods of surface modification of biomass  
204 involve altering the surface properties of biomass materials without introducing chemical changes.  
205 Biomass can undergo modification through a variety of physical processes, including cutting,  
206 grinding, ball milling, boiling, steaming, autoclaving, thermal drying, and pyrolysis (Eldhose et  
207 al., 2023). These methods effectively alter the surface area and particle size of the biomass,  
208 enhancing its adsorption capabilities.

209 **2.1.1. Pretreatment of Biomass:** For the synthesis of activated carbon pretreatment of biomass is  
210 the first step which involves: a) acid washing, removes soluble and insoluble metals, ash, and  
211 lignin from the raw precursor, whereas hot water washing primarily removes soluble ions. Alkaline  
212 pretreatment of lignocellulosic biomass removes silicone and expands the internal structure by  
213 dissolving some of the lignin; b) crushing, to obtain a powder sample; c) drying at 100 °C, to  
214 remove moisture and obtain constant weight; and d) sieving, to obtain homogeneous particles in a  
215 specific range (Mankar et al., 2021).

216 **2.1.2. Pyrolysis of biomass:** Pyrolysis presents an alternative technique for transforming biomass  
217 into valuable products like biochar, bio-oil, and syngas under oxygen-deprived conditions at  
218 temperatures spanning from 300 to 900 °C (Amenaghawon et al., 2021). The process of pyrolysis  
219 can be categorized into slow pyrolysis and fast pyrolysis based on factors such as temperature,  
220 heating rate, pressure, and duration. The fast pyrolysis offers significant advantages by boosting  
221 bio-oil yield, reaching up to 75% from biomass, with a rapid heating rate exceeding 200 °C/min  
222 and a residence time of less than 10 s. However, the slow pyrolysis occurs within the temperature  
223 range of 400 to 600 °C, operates at atmospheric pressure, featuring a relatively lengthy residence  
224 time exceeding 1 h and low heating rates of 5-7 °C/min (Kambo & Dutta, 2015). This method  
225 mainly yields biochar while producing limited amounts of condensed bio-oil, syngas, and  
226 hydrocarbons.





Materials Advances Accepted Manuscript

Open Access Article. Published on 09 October 2025. Downloaded on 10/10/2025 21:44:58. This article is licensed under a Creative Commons Attribution 3.0 Unported Licence.



228 **Figure 3.** Schematic representation of biomass-derived carbon materials (biochar, hydrochar,  
229 activated carbon) and their surface modification/metal immobilization pathways for environmental  
230 remediation applications.

231  
232 **2.1.3. Hydrothermal carbonization:** Recently, hydrothermal carbonization has become more  
233 popular for making activated carbon compared to the traditional thermal carbonization method in  
234 an inert atmosphere. This is because the hydrothermal carbonization method doesn't necessitate  
235 the initial step of drying the biomass (Masoumi et al., 2021). In contrast to pyrolysis, it is observed  
236 as a cost-effective way to produce hydrochar because the hydrothermal carbonization is generally  
237 performed at low temperatures (between 180 to 250 °C) under pressure in water. When water is  
238 present, several chemical reactions occur, including hydrolysis, dehydration, decarboxylation,  
239 aromatization, and re-condensation. The resulting hydrochar contains a large number of  
240 oxygenated functional groups like hydroxylic, carboxylic, and phenolic, which make it more  
241 hydrophilic and also improve its ability to adsorb substances (Masoumi et al., 2021).

#### 242 **2.1.4. Microwave heating:**

243 Microwave irradiation for heating has gained significant attention from researchers owing  
244 to its capacity to transfer heat effectively at the molecular level. This enables a more uniform and  
245 rapid thermal conductivity from the heat source. The microwave heating technique can be  
246 integrated with physical and/or chemical activation processes to produce activated carbons (ACs)  
247 with enhanced performance, employing either a single-stage or two-stage activation procedure.  
248 One-step microwave (MW) activation offers distinct advantages such as a more condensed  
249 structure, smaller footprint, and simpler operation compared to traditional two-step activation  
250 methods (Menéndez et al., 2010). Two-step MW activation processes typically involve  
251 carbonization and subsequent activation of the char, with either activation or carbonization  
252 conducted under MW irradiation. MW heating offers numerous advantages over conventional  
253 heating methods, including uniform and internal heating, rapid and selective heating, ease of  
254 control, straightforward setup, insensitivity to particle size and shape, and reduced pretreatment  
255 requirements for biomass (Ao et al., 2018).

256



257 **2.2. Chemical Modification:** Chemical modification of biomass involves altering its chemical  
258 composition through various chemical treatments commonly employed for surface modification  
259 of agricultural biomass to enhance its properties for various applications.

260 **2.2.1. Acid modification of biomass:** Acid modification represents a typical wet oxidation process  
261 commonly employed for surface alteration. Mineral acids and oxidants such as  $\text{HNO}_3$ ,  $\text{H}_2\text{O}_2$ ,  
262  $\text{HClO}$ ,  $\text{H}_2\text{SO}_4$ ,  $\text{H}_3\text{PO}_4$ , and  $\text{HCl}$  are utilized in acid modification processes. While organic acids  
263 like acetic, carboxylic acid, formic acid, and oxalic are rarely used due to their weaker effect  
264 stemming from their low strength. The acidification of the adsorbent surface enhances its acidic  
265 behavior and hydrophilic nature by reducing mineral content. Adsorbents with an acidic surface  
266 feature oxygen-containing functional groups such as carboxyl, carbonyl, quinone, hydroxyl,  
267 lactone, and carboxylic anhydride (Abegunde et al., 2020). These functional groups are typically  
268 situated on the outer surfaces or edges of the basal plane on activated carbon, significantly  
269 influencing the material's chemical properties (Demiral et al., 2021). Researchers have extensively  
270 explored the utilization of acid-modified adsorbents for water decontamination purposes,  
271 reflecting ongoing efforts in this area.

272 **2.2.2. Alkaline modification of biomass:** Modifying adsorbents with reducing agents can  
273 markedly alter their surface functional groups, leading to significant enhancements in their  
274 adsorption capacities. This process tends to improve the relative abundance of alkali groups and  
275 render the surface more non-polar, thereby improving the adsorption capacity for non-polar  
276 substances. When subjected to alkali treatment, an adsorbent acquires a positive charge on its  
277 surface, which in turn boosts the adsorption of negatively charged species. Surface reduction can  
278 be achieved through treatments involving  $\text{NaOH}$ ,  $\text{KOH}$ ,  $\text{LiOH}$ ,  $\text{Na}_2\text{SiO}_3$ ,  $\text{Na}_2\text{CO}_3$ , and various  
279 oxides (Abegunde et al., 2020).

280 **2.3. Physico-chemical activation of biomass:** Activated carbon finds wide-ranging applications,  
281 including the removal of various contaminants from water and wastewater, as well as its utilization  
282 in capacitors, battery electrodes, catalytic supports, and gas storage materials. These applications  
283 arise from its desirable characteristics, including its large surface area and porosity, along with its  
284 surface chemistry capable of interacting with molecules possessing specific functional groups  
285 (Heidarinejad et al., 2020). Over the past decade, there has been growing recognition of the  
286 potential of biowaste to yield low-cost adsorbents, leading to numerous studies assessing the



287 characteristics and efficacy of activated carbon derived from various biowaste sources for  
288 wastewater pollutant removal (**Table 1**).

289



290 **Table 1.** Synthetic approaches involving surface modification of biomass.

| <b>Biomass</b>    | <b>Process type</b> | <b>Pre-treatment</b>  | <b>Activator</b>                   | <b>Activating condition</b>                   | <b>Ref.</b>                     |
|-------------------|---------------------|---|------------------------------------|---|---------------------------------|
| Barley straw      | Two-step            | Carbonization, N <sub>2</sub> atm.                              | CO <sub>2</sub> and steam          | 800 °C in CO <sub>2</sub> and 700 °C in steam | (Pallarés et al., 2018)         |
| Date seeds        | Single step         | None  | KOH/H <sub>2</sub> SO <sub>4</sub> | 600- 900 °C, N <sub>2</sub> atm.              | (Ogungbenro et al., 2020)       |
| Apple bagasse     | Two-step            | Pyrolysis with CO <sub>2</sub> , 800 °C                         | KOH                                | 800 °C, N <sub>2</sub> atm.                   | (Suárez & Centeno, 2020)        |
| Kenaf             | Single step         | None  | H <sub>3</sub> PO <sub>4</sub>     | 600 °C, N <sub>2</sub> atm.                   | (Baek et al., 2019)             |
| Cashew nut        | Single step         | None  | H <sub>3</sub> PO <sub>4</sub>     | 400–700 °C, N <sub>2</sub> atm.               | (Geczo et al., 2021)            |
| Corn straw        | Single step         | None  | H <sub>3</sub> PO <sub>4</sub>     | 300 °C, N <sub>2</sub> atm.                   | (Q. Yang et al., 2020)          |
| Pine wood sawdust | Single step         | None  | H <sub>3</sub> PO <sub>4</sub>     | 800 °C, N <sub>2</sub> atm.                   | (X. Gao et al., 2018)           |
| Corn cob          | Single step         | None  | H <sub>3</sub> PO <sub>4</sub>     | 450- 850 °C, N <sub>2</sub> atm.              | (Y. Liu et al., 2017)           |
| Jujun Grass       | Two-step            | Hydrothermal carbonization                                      | KOH                                | 900 °C, N <sub>2</sub> atm.                   | (Demir et al., 2017)            |
| Lecithin          | Two-step            | Hydrothermal carbonization                                      | KOH                                | 900 °C, N <sub>2</sub> atm.                   | (Xing et al., 2019)             |
| Wheat straw       | Two-step            | ZnCl <sub>2</sub> catalytic hydrothermal carbonization (200 °C) | H <sub>3</sub> PO <sub>4</sub>     | 500 °C, N <sub>2</sub> atm.                   | (Dey & Ahmaruzzaman, 2023)      |
| Cotton shell      | Single step         | None  | KOH                                | 600 °C, N <sub>2</sub> atm.                   | (Kaur et al., 2024a)            |
| Coconut shell     | Single step         | None  | ZnCl <sub>2</sub>                  | 500 °C, N <sub>2</sub> atm.                   | (Sangeetha Piriya et al., 2021) |
| Tobacco stalks    | two-step            | carbonized at 700 °C  | None                               | 1000 °C, 5 h                                  | (Ju et al., 2023)               |
| Shiitake mushroom | Single step         | None  | None                               | 300 °C, 500 °C, 700°C                         | (X. Liu et al., 2023)           |

|                           |             |                      |   |   |                                    |
|---------------------------|-------------|----------------------|---|---|------------------------------------|
| Rape straw                | Two-step    | carbonized at 700 °C | KOH   | 750 °C  | (Y. Qin et al., 2022)              |
| Sunflower                 | Two-step    | 650 °C               | Ag/ vitamin C/<br>and H <sub>2</sub> O <sub>2</sub> | None  | (Tomczyk & Szewczuk-Karpisz, 2022) |
| Rice straw                | Two-step    | 700 °C               | Tannic acid   | None  | (J. Chen et al., 2021)             |
| Food and plant waste      | Single step | None                 | None  | 300 °C  | (Hoslett et al., 2021)             |
| Cow manure                | Single step | None                 | None  | Carbonized at 300 °C,<br>500 °C, 700°C, N <sub>2</sub> atm. | (P. Zhang et al., 2019)            |
| Pomelo peels              | Two-step    | Carbonized at 400 °C | KOH   | 600, 700, 800, 900 °C,<br>N <sub>2</sub> atm.               | (D. Chen et al., 2017)             |
| Wheat Straw               | Single step | None                 | None  | 600 °C, N <sub>2</sub> atm.                                 | (Cao et al., 2019)                 |
| Rice husk                 | Single step | None                 | NaOH  | None  | (Kaur, Kalpana, et al., 2023)      |
| Seaweed                   | Two-step    | 500 °C               | NaOH  | 800 °C, N <sub>2</sub> atm.                                 | (D. Jiang et al., 2023)            |
| Rice Husk                 | Single step | None                 | NaOH  | None  | (Ye et al., 2010)                  |
| Hazelnut Shell            | Two-step    | None                 | KOH   | 950 °C  | (Yurtay & Kılıç, 2023)             |
| Rice husk                 | Two-step    | None                 | KOH   | 950 °C  |                                    |
| Corn Stalks               | Two-step    | None                 | KOH   | 950 °C  |                                    |
| <i>Erythrina speciosa</i> | Single-step | None                 | ZnCl <sub>2</sub>                                   | None  | (Bouzidi et al., 2023)             |
| Animal dung               | Two-step    | None                 | KOH and   | Hydrothermal activation                                     | (Kandasamy et al., 2023)           |





|                                  |             |                             |  |                               |                            |
|----------------------------------|-------------|-----------------------------|--|-------------------------------|----------------------------|
|                                  |             |                             | ZnCl <sub>2</sub>  |                               |                            |
| Bamboo                           | Two-step    | None                        | KOH  | 700 °C                        | (Cui et al., 2022)         |
| Sesame straw                     | Two-step    | None                        | KOH, Ca(OH) <sub>2</sub>   | Calcination                   | (Y. Zhang et al., 2022)    |
| <i>Thevetia nerifolia</i>        | Two-step    | None                        | H <sub>3</sub> PO <sub>4</sub> , 400 °C                          | 800 °C N <sub>2</sub> atm.    | (Srinivasan et al., 2021)  |
| Acacia wood                      | Two-step    | 500 °C, N <sub>2</sub> atm. | KOH  | 110 °C, Microwave oven        | (Yusop et al., 2021)       |
| <i>Haematoxylum campechianum</i> | Two-step    | None                        | H <sub>3</sub> PO <sub>4</sub>                                   | 500 °C                        | (Abatal et al., 2020)      |
| Sugar cane bagasse               | Two-step    | None                        | ZnCl <sub>2</sub>  | 500 °C N <sub>2</sub> atm.    | (Abo El Naga et al., 2019) |
| Rice husk                        | Two-step    | None                        | NaOH/<br>CH <sub>3</sub> COOH/<br>H <sub>3</sub> PO <sub>4</sub> | 700 °C                        | (K. Huang et al., 2023)    |
| Kesambi wood                     | Two-step    | 400 °C                      | H <sub>2</sub> SO <sub>4</sub>                                   | 110 °C, oven                  | (Neolaka et al., 2021)     |
| Sawdust                          | Two-step    | None                        | KOH  | 800 °C N <sub>2</sub> atm.    | (Kharrazi et al., 2021)    |
| Biomass Peels                    | Two-step    | None                        | H <sub>3</sub> PO <sub>4</sub>                                   | 600 °C                        | (Thompson et al., 2020)    |
| Pistachio wood                   | Single step | None                        | NH <sub>4</sub> NO <sub>3</sub>                                  | 800 °C N <sub>2</sub> atm.    | (Sajjadi et al., 2018)     |
| Date Press Cake                  | Two-step    | 500 °C                      | NaOH   | 750 °C N <sub>2</sub> atm     | (Norouzi et al., 2018)     |
| Rice Husk                        | Single step | None                        | NaOH   | None                          | (Gebrewold et al., 2019)   |
| Corn Cob                         | Single step | None                        | HCl  | None                          | (Gebrewold et al., 2019)   |
| Baobab fruit shells              | Single step | None                        | H <sub>3</sub> PO <sub>4</sub>                                   | 200-900 °C N <sub>2</sub> atm | (Vunain et al., 2017)      |

|                               |             |      |      |         |                     |
|-------------------------------|-------------|------|------|---------|---------------------|
| Poplar flour and walnut shell | Single step | None | None | 1000 °C | (Xu et al., 2023)   |
| Soybean biomass               | Single step | None | None | 900 °C  | (Dong et al., 2023) |

---

291

292



293 Activated carbon is conventionally produced through two primary activation methods: a)  
294 physical activation; and b) chemical activation. The physical activation involves two distinct  
295 thermal stages. Initially, the carbonaceous precursor undergoes pyrolysis or carbonization at high  
296 temperatures, typically between 700–900 °C, in an inert atmosphere to prevent combustion. This  
297 step eliminates heteroatoms and releases volatiles, resulting in chars with high carbon content  
298 (where increased carbonization temperature enhances carbon content), but limited porosity  
299 development. The subsequent stage of physical activation is gasification, entailing the selective  
300 removal of the most reactive carbon atoms through controlled gasification reactions to induce the  
301 characteristic porosity of activated carbons (Kumar Mishra et al., 2024). The gasification  
302 temperature varies depending on the gasification agent utilized, typically water vapor, CO<sub>2</sub>, or  
303 O<sub>2</sub>/air. Water vapor or CO<sub>2</sub> gasification commonly occurs at temperatures ranging around 700–  
304 900 °C, whereas gasification using pure O<sub>2</sub> or air requires much lower temperatures (around 300–  
305 450 °C) due to the higher reactivity of O<sub>2</sub> compared to CO<sub>2</sub> and water vapor. The use of O<sub>2</sub>  
306 complicates gasification control and porosity development due to its high reactivity and  
307 exothermic nature (S. Mishra & Upadhyay, 2021). Generally, CO<sub>2</sub> serves as the preferred  
308 activation gas due to its cleanliness, ease of handling, and facilitation of activation process control  
309 owing to its slow reaction rate at elevated temperatures. Jiang et al. used pyrolysis in the presence  
310 of CO<sub>2</sub> and N<sub>2</sub> as a physical activator to obtain activated hybrid willow biomass (C. Jiang et al.,  
311 2020). Pallares et al. activated barley straw biomass by regulating the gas flow rate of compressed  
312 gas cylinders containing N<sub>2</sub> and CO<sub>2</sub>, along with steam produced using a steam generator at 150  
313 °C (Pallarés et al., 2018).

314 On the other hand, the process of chemical activation involves impregnating a biomass  
315 material with a chemical reagent and then activating it, whether the material is raw or carbonized.  
316 The activation can be achieved in one-step or two-steps. In the one-step process, the raw precursor  
317 is mixed with the activating agent, and then is subjected to carbonization. In the two-step process,  
318 the pre-carbonized biomass is treated with the activating agent, and then it is again subjected to  
319 carbonization. A strong base (NaOH, KOH), acid (H<sub>2</sub>SO<sub>4</sub>, H<sub>3</sub>PO<sub>4</sub>, HCl, HF, etc.), or salt (ZnCl<sub>2</sub>,  
320 CaCl<sub>2</sub>) are employed as an activating agent. In single-step activation, a strong base such as KOH  
321 is typically used (Heidarinejad et al., 2020). After activation, the last step involves the washing to  
322 remove the remaining activating agents or reaction byproducts that occlude the newly formed  
323 porosity and drying. Ogungbenro et al. synthesized activated carbon from date seed biomass using



324 a two-step activation process involving pyrolysis of biomass under CO<sub>2</sub> atmosphere followed by  
325 treatment with chemical activators such as KOH and H<sub>2</sub>SO<sub>4</sub> (Ogungbenro et al., 2020). Suarez and  
326 Centeno, obtained activated carbon from apple bagasse using pyrolysis under CO<sub>2</sub> and then  
327 activation with KOH under N<sub>2</sub> atmosphere (Suárez & Centeno, 2020). A mesoporous activated  
328 carbon from Kenaf (Baek et al., 2019), cashew (Geczo et al., 2021), corn straw (Q. Yang et al.,  
329 2020), sawdust biomass (X. Gao et al., 2018), and Corncob (Y. Liu et al., 2017) was obtained  
330 using a single step pyrolysis under the N<sub>2</sub> atmosphere in the presence of H<sub>3</sub>PO<sub>4</sub> as a chemical  
331 activator. The activated carbon from Jujun grass (Demir et al., 2017), Lecithin (Xing et al., 2019),  
332 and Wheat straw (Dey & Ahmaruzzaman, 2023) biomass was obtained by two-step hydrothermal  
333 carbonization with KOH and H<sub>3</sub>PO<sub>4</sub> as a chemical activator. Sangeetha et al. synthesized activation  
334 carbon in the presence of ZnCl<sub>2</sub> from coconut shell (Sangeetha Piriya et al., 2021).

335  
336 **2.4. Nanostructuring of biomass and its derivatives:** The fabrication of these biomaterials with  
337 inorganic nanoparticles such as metal/metal oxides will not only increase their surface area of  
338 contaminant absorption, but also make them an efficient catalyst for studying various organic  
339 contaminant degradation processes (Zhong et al., 2023). The adsorption tendencies of biomass  
340 materials complemented with the catalytic efficiencies of inorganic nanoparticles and generate a  
341 synergistic effect, which is effective in the removal of various contaminants from their aqueous  
342 solution (Mazarji et al., 2023). The Fe is a pure metal and magnetic in nature; thus, a magnetic  
343 biochar can be obtained when Fe is immobilized on biochar. Nano-sized Fe, also known as  
344 nanoscale zero-valent iron (nZVI), is highly unstable in the environment, however, many studies  
345 have confirmed that by coating nZVI on biochar could be an efficient approach to getting a stable  
346 nZVI@biochar composite with simultaneous high reactivity due to dispersive nZVI on biochar  
347 (Singh, 2023). The removal mechanisms of nZVI@biochar include reduction, surface  
348 complexation, and coprecipitation. The magnetic biochar can also be prepared by pre-treatment  
349 and post-treatment of biomass. In the pre-treatment process, pyrolysis of biomass in the presence  
350 of FeCl<sub>3</sub> or FeCl<sub>2</sub> is performed. However, in the post-treatment precipitation of biochar with FeSO<sub>4</sub>  
351 and FeCl<sub>3</sub> under basic conditions results in immobilization of the iron hydroxides (Fe(OH)<sub>3</sub>) on  
352 biochar (Lu et al., 2020). In literature, the magnetic biochar have been synthesized using different  
353 kinds of methods with various biomass and magnetic mediums. The popular methods including  
354 co-precipitation, thermal decomposition, and/or reduction, and hydrothermal synthesis techniques,



355 can all be directed to the synthesis of high-quality magnetic biochar. The iron oxides such as  $\text{Fe}_3\text{O}_4$   
356 and  $\gamma\text{-Fe}_2\text{O}_3$ , have been studied largely due to their low cost of raw materials and ease of synthesis  
357 (Chavali & Nikolova, 2019). Other than  $\text{Fe}_3\text{O}_4$ , other metal oxides such as  $\text{CuO}$ ,  $\text{TiO}_2$ ,  $\text{ZnO}$ ,  $\text{MnO}_2$ ,  
358  $\text{Co}_3\text{O}_4$ , etc., have also been immobilized on biomass and its derivative surfaces and have been  
359 extensively explored for their environmental remediation applications (Isikgor & Becer, 2015).

360

## 361 **2.5 Comparative analysis of surface modification techniques**

362 While a wide range of surface modification strategies have been developed for biomass, their  
363 effectiveness, scalability, and environmental impact vary significantly. *Chemical modifications*  
364 (e.g., acid/alkali activation, oxidative treatments) are highly effective in introducing functional  
365 groups and creating well-developed porosity, which enhances adsorption and catalytic  
366 performance. However, these approaches often require strong reagents ( $\text{H}_2\text{SO}_4$ ,  $\text{HNO}_3$ ,  $\text{KOH}$ , etc.),  
367 generate secondary effluents, and may raise concerns regarding environmental safety and process  
368 sustainability.

369 In contrast, *physical methods* such as pyrolysis, hydrothermal carbonization, and microwave  
370 heating offer greener and more scalable routes, especially at pilot or industrial levels. These  
371 methods minimize the use of hazardous chemicals and often produce by-products like bio-oil and  
372 syngas that can be valorized. However, their effectiveness in producing high surface areas and  
373 tailored functionalities is sometimes limited compared to chemical treatments, often necessitating  
374 post-treatment or hybrid approaches.

375 *Biological modifications*, employing microbial or enzymatic pretreatments, represent the most  
376 eco-friendly strategies, with minimal chemical waste and reduced energy requirements. They can  
377 selectively alter lignin, cellulose, or hemicellulose fractions to improve accessibility of active sites.  
378 Yet, their relatively slow kinetics, sensitivity to environmental conditions, and difficulties in  
379 scaling beyond laboratory studies restrict their current industrial applicability.

380 From a sustainability standpoint, the integration of *physico-chemical* or *bio-assisted hybrid*  
381 *approaches* may offer the best compromise—combining the efficiency of chemical treatments  
382 with the environmental friendliness of biological methods and the scalability of physical routes.  
383 Future research should therefore focus on techno-economic analyses and life-cycle assessments  
384 (LCA) to evaluate not only the technical performance but also the overall environmental footprint  
385 of each modification pathway.



### 386 3. Structure of biomass adsorbents

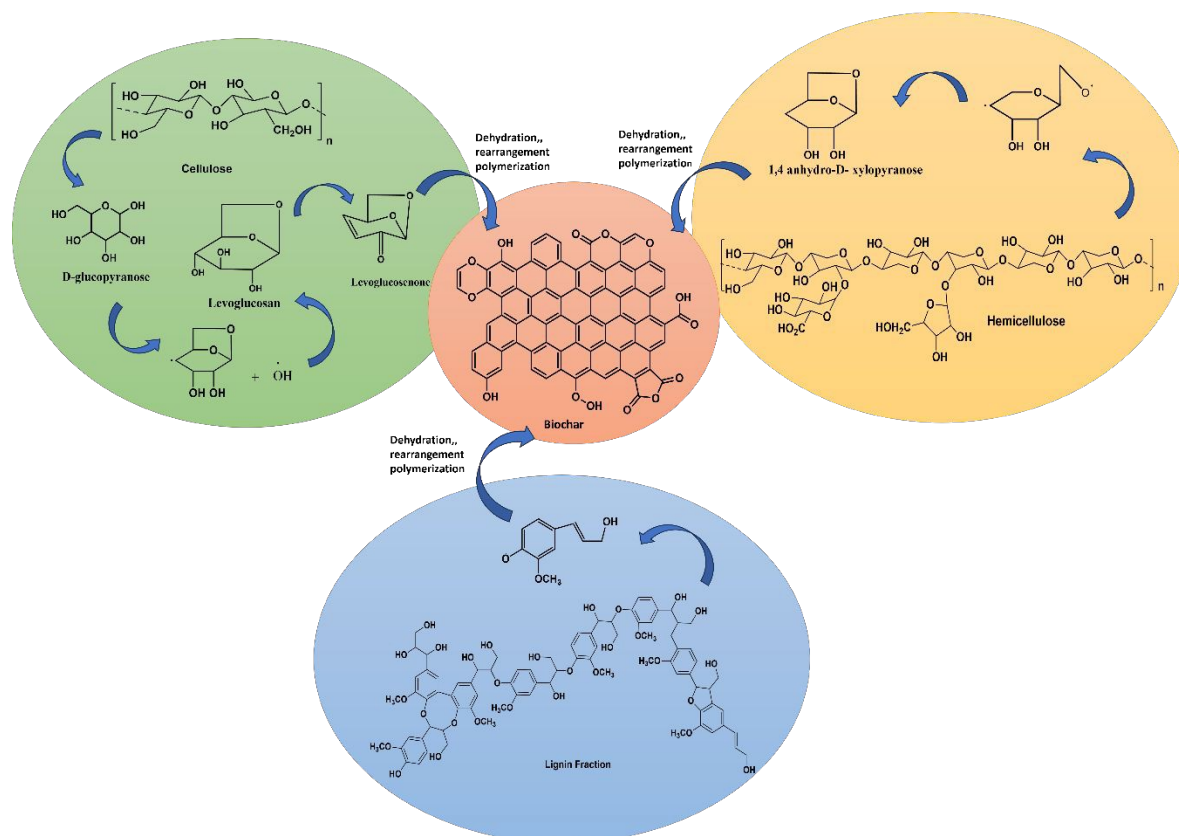
387 The biomass is mainly categorized into two: lignocellulosic and non-lignocellulosic  
388 biomass, having chemical compositions different altogether, with the former being extensively  
389 used for its environmental remediation applications. The lignocellulosic biomass mainly consists  
390 of cellulose, hemicellulose, silica, and lignin. The complex nature of the lignocellulosic biomass  
391 not only provides the structural integrity to the plants, but also contributes to the rigidity and  
392 strength to the overall structure. The sources of lignocellulose biomass include wood, agricultural  
393 residues, and dedicated energy crops (S. Wu et al., 2022). On the other hand, the non-  
394 lignocellulosic biomass includes materials like algae, aquatic plants, animal dung, sewage sludge,  
395 and organic waste streams, etc., which contains a diverse array of organic compounds. The  
396 composition of non-lignocellulosic biomass is mainly proteins, lipids, and carbohydrates (Joseph,  
397 2023). The lignocellulosic biomass has a porous structure, and high surface area, making it useful  
398 in the adsorption processes for the removal of recalcitrant pollutants such as heavy metals, dyes,  
399 and organic compounds from water. The abundant hydroxyl and carboxyl groups present in the  
400 lignocellulosic biomass facilitates the binding of contaminants through physical as well as  
401 chemical interactions (Y. Zhou et al., 2015). The algal biomass exhibits a high affinity for  
402 nutrients, such as nitrogen and phosphorus, thus making it suitable for wastewater treatment  
403 applications through processes like nutrient uptake and biofiltration (Joseph, 2023).

404 The chemical and physical modifications can be applied to the surface of biomass in order  
405 to enhance its properties, and potential applications. The physical modifications affect the surface  
406 morphology and topography of biomass, resulting in change in the surface area, porosity, and  
407 accessibility of active sites (Eldhose et al., 2023). The chemical modification results in change of  
408 composition, and the functional groups on the surface of biomass (Yaashikaa et al., 2020). These  
409 modifications can improve certain properties such as hydrophobicity, thermal stability, and  
410 compatibility with other materials, thus expanding the range of applications in biocomposites,  
411 adsorption, and catalysis.

412 *Biochar*, a stable carbon-rich solid product, is obtained through biomass pyrolysis in an  
413 environment with limited oxygen. During this process, the hydroxyl, carboxyl, and carbonyl  
414 groups present in the biomass are removed, resulting in a modified surface chemistry of biochar  
415 with higher carbon content, and lower concentration of oxygen-containing functional groups  
416 compared to the original biomass (Rane et al., 2018). Within biochars, carbon, oxygen, and



417 hydrogen species comprise both inorganic (like  $\text{HCO}_3^-$ ,  $\text{CO}_3^{2-}$ , metallic oxides, and hydroxides)  
 418 and organic components (such as C–C, C=C, C–H, –C–O–H, C=O, C–O–C, COOH, and –C<sub>6</sub>H<sub>5</sub>).  
 419 The organic component, resembling a skeleton in biochar, originates from cellulose,  
 420 hemicellulose, and lignin in the biomass, transforming into aliphatic carbon at lower and  
 421 intermediate pyrolysis temperatures, and transitioning to aromatic carbon at higher temperatures  
 422 (P. Zhang et al., 2022) (**Figure 4**).



423

424 **Figure 4.** Scheme for biochar synthesis from lignocellulosic biomass.

425

426 The surface chemistry of biochar, encompassing surface functional groups, surface charge,  
 427 and free radicals, play a crucial role in its interaction with organic and inorganic contaminants.  
 428 These factors provide significant sites for adsorption and catalytic degradation of pollutants.  
 429 Different sorption mechanisms, such as partitioning, hydrogen bonding,  $\pi$ – $\pi$  bonding, electrostatic  
 430 interaction, and pore-filling, rely on the properties of both biochar and pollutants. The surface  
 431 negative charge across the natural pH range of 4–12 in biochars originates from the breakdown of



432 functional groups (such as carboxyl moieties) and their aliphatic/aromatic surface (Gale et al.,  
433 2021). Typically, the biochar surfaces become more negatively charged as the pH of the solution  
434 rises above 4. The electrostatic interactions, regulated by the solution, influence the transport of  
435 biochar particles and ions. Additionally, biochar displays redox activity due to the presence of  
436 electroactive moieties like quinones, phenolic functional groups, polycondensed aromatic sheets,  
437 and redox-active metals, capable of accepting/donating or conducting electrons (Chavali &  
438 Nikolova, 2019). The electrochemical analyses of the biochar indicate that the redox-active  
439 moieties and their electron transfer capacities vary with pyrolysis temperatures, suggesting a  
440 correlation between redox properties and biochar structure. In a biochar-mediated p-nitrophenol  
441 (PNP) decomposition, approximately 20% of PNP degradation occurs via  $\cdot\text{OH}$  radicals produced  
442 from the activation of  $\text{H}_2\text{O}_2$  by redox-active sites in biochar, while around 80% of PNP degradation  
443 involves direct interaction with reactive sites, likely hydroquinones in biochar, through two one-  
444 electron transfers, leading to the production of reduced PNP (P. Zhang et al., 2023, p.).

445 *Hydrochar*, a carbon-rich material produced through hydrothermal carbonization of  
446 biomass, which involves heating biomass in water at high pressure and temperature. Its structure  
447 typically consists of a network of condensed carbon rings, resulting in a material with high carbon  
448 content and significant porosity. The composition of hydrochar includes a mix of carbon,  
449 hydrogen, and oxygen, with some residual inorganic minerals depending on the feedstock used.  
450 Its properties are characterized by increased stability and reduced volatility compared to the  
451 original biomass, making it suitable for applications like water treatment, and energy storage. The  
452 hydrochar obtained from the physical activation process has poor porosity and surface area  
453 compared to one produced from chemical activation procedure. The porous structure of hydrochar  
454 enhances its surface area, contributing to its effectiveness in adsorbing contaminants and  
455 improving its performance in various environmental and industrial applications (Kambo & Dutta,  
456 2015; Masoumi et al., 2021).

457 *Activated Carbon*, a carbon material derived from organic materials such as agricultural  
458 residues, wood, or other plant-based sources through a process of carbonization followed by  
459 activation or *vice-versa*. Its structure features a network of highly porous carbon, including a range  
460 of pore sizes from macropores to micropores, which creates an extensive surface area for  
461 adsorption (Kaur et al., 2024b). The composition predominantly consists of carbon, with varying



462 amounts of residual ash, minerals, and potentially some remaining organic matter, depending on  
463 the original biomass and the activation method used. This porous structure enhances the material's  
464 ability to adsorb contaminants from gasses and liquids, making biomass activated carbon a  
465 valuable resource for environmental remediation, water treatment, and other applications requiring  
466 efficient adsorption (Heidarinejad et al., 2020).

467 *Nanostructured biomass*, the immobilization of metal/metal oxide nanoparticles on the  
468 surface of biomass and its derived materials give metal nanocomposites. There are various  
469 methods for nanocomposite synthesis, such as impregnation, precipitation, in-situ reduction, and  
470 carbothermal reduction (Sargazi et al., 2019). The metal nanoparticles interact with the functional  
471 groups on the biomass surface through various mechanisms, including chemical bonding,  
472 electrostatic forces, and van der Waals interactions. The functional groups like hydroxyl, carboxyl,  
473 and amino groups on the biomass can form bonds with the nanoparticles or attract them due to  
474 their charges. These interactions help integrate the nanoparticles into the biomass, influencing how  
475 well they are dispersed and attached. Modification of the surface of either the biomass or the  
476 nanoparticles can enhance these interactions, ultimately affecting the composite's properties such  
477 as strength and reactivity. The unique properties of biomass, such as its porous structure, high  
478 surface area, and functional groups stabilizes the metal nanoparticles. In addition, the synergistic  
479 interactions between the metal nanoparticles and the biomass renders the biomass-based metal  
480 nanocomposites with enhanced adsorption and catalytic properties (Kumar et al., 2023).

481

#### 482 **4. Characterization techniques for biomass and its derived materials:**

483 Various characterization techniques or methods are utilized to assess biomass or its  
484 nanocomposite materials, including biochar, hydrochars, or activated carbons, tailored to their  
485 distinctive chemical, physical, and structural properties.

486 **4.1. Characterization techniques for physical/morphological properties:** Biomass and its  
487 derived materials have different physical properties such a surface area, pore volume, and pore  
488 size distribution. The characterization techniques such as microscopy, Brunauer-Emmett-Teller  
489 (BET), transmission electron microscopy (TEM), scanning electron microscopy (SEM), X-ray  
490 diffraction (XRD), thermogravimetric analysis (TGA) and differential thermal analysis (DTA) etc.

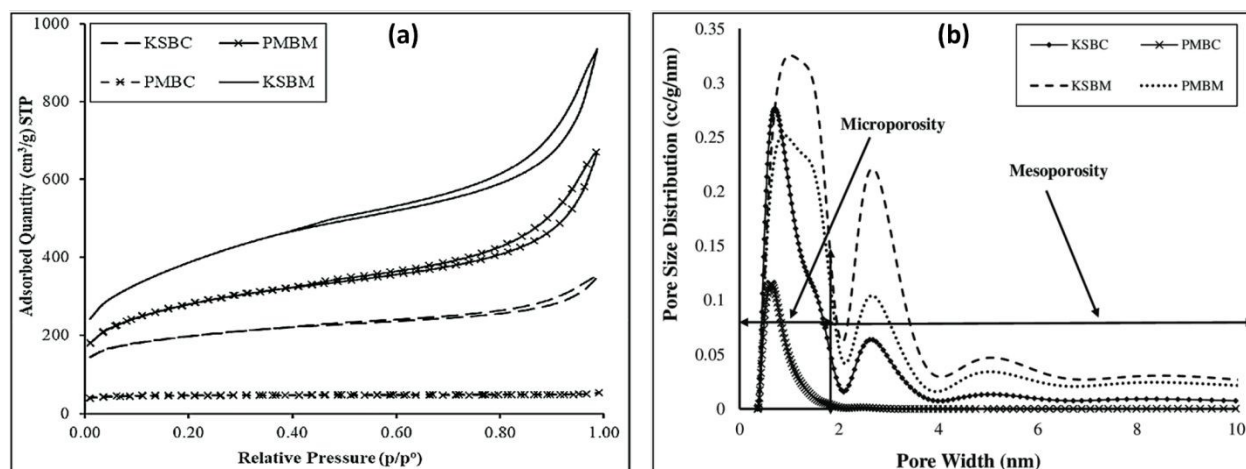


491 are used to analyze the physical and structural properties of biomass, biochar, activated carbon and  
492 metal immobilized nanocomposites.

493 *4.1.1. Brunauer-Emmett-Teller analysis:* Depending on the activation method employed (physical  
494 or chemical) the BET surface area of biomass undergoes significant changes upon activation. The  
495 surface area of untreated biomass is comparatively higher than the thermal activated material. As  
496 the thermal activation typically leads to a decrease in surface area due to the removal of volatile  
497 matter at higher temperature. On the other hand, the chemical activation tends to increase the BET  
498 surface area by introducing additional pores, and creating a more porous structure. Different types  
499 of BET (Brunauer-Emmett-Teller) isotherms Type I, II, III, or IV are shown by biomass materials  
500 reflecting their diverse structural characteristics and porosities (Sing, 1995). Type I isotherms are  
501 typically observed for the materials with well-defined micropores exhibiting a sharp increase in  
502 adsorption at relatively low pressures followed by a plateau, indicating the presence of a monolayer  
503 adsorption (Bedia et al., 2018). Type II isotherms are characteristic of materials with non-porous  
504 or macroporous structure, and display a gradual increase in adsorption with increasing the relative  
505 pressure. The biomass-derived materials with less defined porosity or larger pore sizes may exhibit  
506 Type II isotherms (Schlumberger & Thommes, 2021). Type III isotherms are commonly associated  
507 with materials having mesoporous structure and exhibit an inflection point in the adsorption curve,  
508 indicating the formation of multilayer adsorption on the mesoporous surfaces. This is often  
509 observed in activated carbons derived from biomass with a significant mesopore volume. The Type  
510 IV isotherm indicates hierarchical porosity, displaying both micropores and mesopores. Oginni, et  
511 al. investigate that the activated carbon obtained from Public Miscanthus (PMBC) and Kanlow  
512 Switchgrass (KSBC) biochar showed type I and type IV isotherms, respectively (Oginni et al.,  
513 2019) (**Figure 5**). The activated carbons had pore diameters ranging from 2.01 to 4.15 nm. The  
514 activated carbon derived from biomass had larger average pore sizes due to the ordered porous  
515 structure of the biochar precursors. This minimized the impact of the activating agent on enhancing  
516 the porous structure of the final biochar-derived activated carbons (Oginni et al., 2019).

517



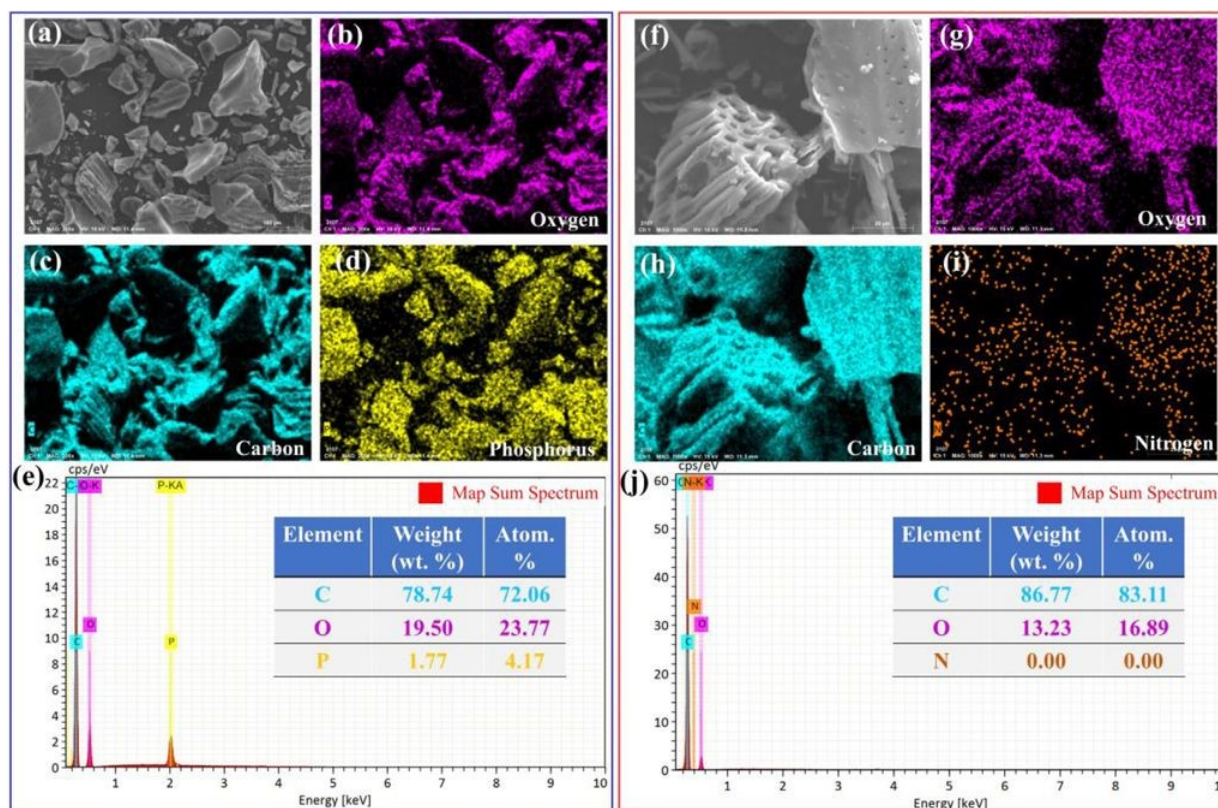


518  
519 **Figure 5.** (a) N<sub>2</sub> adsorption/desorption isotherms; and (b) pore size distribution for biochar-derived  
520 and biomass-derived activated carbons (Oginni et al., 2019) (Reproduced with permission,  
521 Elsevier, 2019).

522  
523 *4.1.2. Scanning electron microscopy (SEM) and energy dispersive X-ray spectroscopy (EDS):*  
524 SEM-EDS is an outstanding technique that provides both qualitative morphological and elemental  
525 information. The SEM image of biochar and activated carbon exhibits irregular structures with  
526 high heterogeneous surface properties and irregular dense pores. These surface irregularities play  
527 an important role in the contaminant removal. The activation processes induced structural changes  
528 within the carbon framework, causing it to collapse under high temperatures. The alkali treatment  
529 serves as a pore-forming agent, initiating the generation of active vapor or CO/CO<sub>2</sub>, which  
530 promotes the formation of pores. These pores not only increase the surface area but also provide  
531 an abundance of defective sites, facilitating enhanced adsorption and catalytic activities (Girão et  
532 al., 2017). Shao et al. investigated the morphological structure of bamboo and pigeon pea stalks  
533 that have a gentle surface with no pores. The biochar prepared at 400 °C and 500 °C from bamboo  
534 and pigeon pea stalks had honeycomb-like porous structures. The increase in the pyrolysis  
535 temperature to 600 °C causes the pores to crumble and form a channel-like structure (Shao et al.,  
536 2022). From SEM analysis of eucalyptus biochar (EC) and eucalyptus derived activated carbon  
537 (AC) it was confirmed that the former has small irregular shaped particles, whereas uniform sized  
538 particles were observed for the later. The element composition analysis of activated carbon and  
539 biochar displayed carbon as the dominant component (72-83%), and oxygen in smaller amounts



540 (4-23%), along with other trace elements such as P and N in the sample (Maia et al., 2021) (Figure  
541 6).  
542



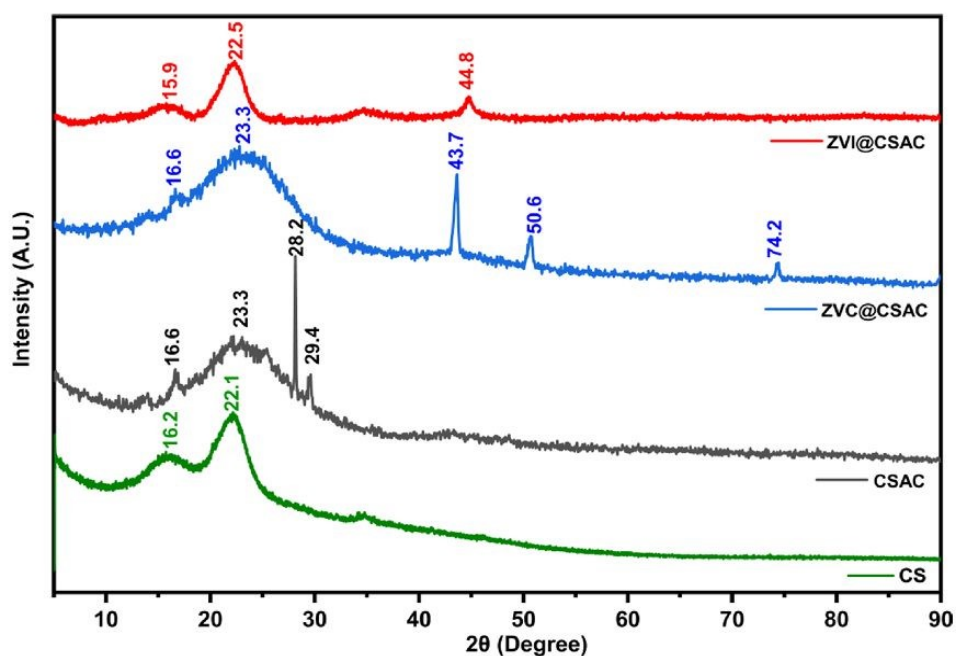
543  
544 **Figure 6.** The elemental mapping and EDS mass spectrum of (a-e) Eucalyptus activated carbon  
545 (AC), and (f-j) Eucalyptus biochar (EC) (Maia et al., 2021) (Reproduced with permission, Elsevier,  
546 2021).

547  
548 *4.1.3. X-ray diffraction analysis:* X-ray diffraction (XRD) analysis offers invaluable insights into  
549 the structural properties of biomass, and its derived materials. The XRD analysis investigates the  
550 crystalline structure of biomass constituents such as cellulose, hemicellulose, and lignin. After  
551 pyrolysis, XRD analysis gives information of the structural properties as the conversion of organic  
552 materials into a carbon-rich, porous matrix upon activation of biomass. Gale et al. explored the  
553 effect of the activation on the structural properties of biomass. The activation of biomass decreases  
554 the intensity of cellulosic peaks and the crystallite size. The temperature increase during the  
555 activation breaks down the lignocellulosic biomass and generates the turbostratic carbon (t-carbon)  
556 with a peak at  $26^\circ$  ( $2\theta$ ), indicating the potential growth of graphene layers (Gale et al., 2021). Kaur



557 et al. also investigated the effect of XRD analysis of biomass before and after activation, and they  
 558 found that significant changes in the phase composition and crystallinity were observed. The  
 559 untreated biomass showed broad diffraction peaks at  $16.2^\circ$  and  $22.1^\circ$ , indicating the amorphous  
 560 nature of carbon-containing biomass, attributed to the typical reflection plane (002). However, the  
 561 XRD patterns after chemical activation of lignocellulosic biomass showed shifted peaks at  $16.6^\circ$   
 562 and  $23.3^\circ$ , indicating the presence of crystalline structured graphitic carbons with intense graphitic  
 563 peak at  $2\theta$  values of  $28.2^\circ$  and  $29.4^\circ$  was observed in the XRD pattern of activated biomass,  
 564 indicating a high degree of crystallinity achieved after the activation process. The XRD analysis  
 565 of these structural changes provides valuable insights into the transformation of biomass during  
 566 activation (Kaur et al., 2024a) (**Figure 7**).

567



568

569 **Figure 7.** XRD pattern of biomass (CS), activated carbon (CSAC), and its metal-immobilized  
 570 nanocomposites (Kaur et al., 2024a) (Reproduced with permission, Elsevier, 2024).

571

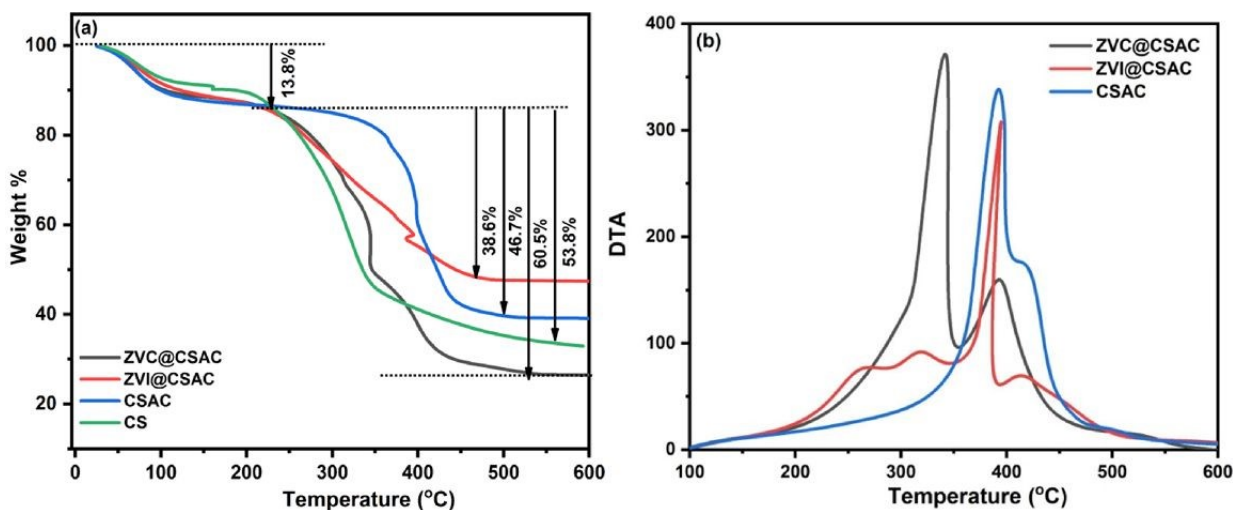
572 *4.1.4. Thermogravimetric analysis (TGA) and differential thermal analysis (DTA):* The TGA/DTA  
 573 analysis explains thermal behaviour of biomass and its derived materials. In the TGA analysis, the  
 574 weight percentage change is monitored as a function of temperature or time under controlled  
 575 pressure (Y. Chen et al., 2023). The TGA analysis depicts its thermal stability, pore structure, and  
 576 surface functional groups. With the help of the degradation stages, the TGA elucidates the key



577 thermal events like dehydration, breakdown of cellulose and lignin and char formation. Further,  
578 the DTA analysis provides information regarding endothermic and exothermic reactions, phase  
579 transitions and chemical reactions within the materials (Nair et al., 2022). The activation of  
580 biomass, with pyrolysis or chemical treatment, leads to a notable increase in its thermal stability.  
581 The changes on the surface of biomass act as thermal stabilizers and inhibit thermal breakdown  
582 reactions and enhance thermal stability. This enhancement may arise from several factors such as  
583 the removal of volatile organic compounds and moisture from the surface of biomass, structural  
584 rearrangement with formation of new chemical bonds, creation of a porous structure, generation  
585 of new functional groups on the surface of biomass during the activation step, and reduction in its  
586 propensity for combustion or decomposition at lower temperature (Demiral et al., 2021). Further,  
587 the immobilization of inorganic materials such as metal/metal oxide nanoparticles on the surface  
588 of biomass and its derived materials also enhance the thermal stability of nanocomposites (Akhtar  
589 et al., 2020). Maia et al. used physico-chemical activation via KOH treatment followed by  
590 pyrolysis to prepare palm fibre biomass derived activated carbon, and used it for the adsorptive  
591 removal of methylene blue dye. In the TGA analysis, it was observed that the thermal stability of  
592 palm fibre biomass derived activated carbon was significantly increased (Maia et al., 2021). Kaur  
593 et al. investigated the higher thermal stability of the cotton shell activated carbon (CSAC) and its  
594 metal nanocomposites compared to the raw CS biomass. The increment in thermal stability is  
595 attributed to the formation of different surface groups at specific sites through the interaction of  
596 oxygen and oxidized gasses, as well as the immobilization of inorganic material on its surface  
597 (Kaur et al., 2024a) (**Figure 8**).

598





599  
600 **Figure 8.** (a) TGA graph for CS, CSAC, ZVC@CSAC, and ZVI@CSAC; (b) DTA curves for CSAC,  
601 ZVC@CSAC, and ZVI@CSAC (Kaur et al., 2024a).

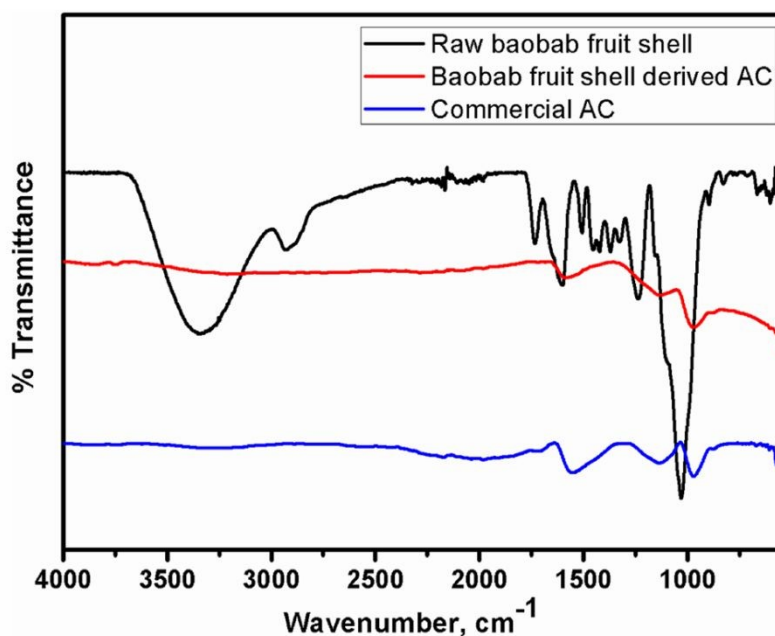
602  
603 **4.2. Characterization techniques for chemical properties:** The chemical compositions of  
604 cellulose, hemicellulose, and lignin, decides the chemical properties of biomass materials, which  
605 further depends on the source material and processing methods to obtain the biomass. When the  
606 biomass undergoes activation to produce activated carbon, its chemical properties undergo  
607 significant change. The activated carbon obtained via chemical treatment possesses a highly  
608 porous structure, which increases its surface area and alters its chemical reactivity. This material  
609 typically exhibits a high carbon content and a reduced amount of impurities like moisture and  
610 volatile organic compounds (Demiral et al., 2021). The functional groups present in the precursor  
611 biomass also have significant impact on the surface chemistry of activated carbon, deciding its  
612 adsorption capabilities and reactivity towards different molecules. These properties render  
613 activated carbon a versatile material widely used in various applications, such as water  
614 purification, air filtration, and adsorptive removal of contaminants from industrial processes  
615 (Joseph, 2023). The characterization techniques used for the evaluation of chemical properties of  
616 biomass and its derived materials is discussed below:

617 *4.2.1. Fourier-transform infrared spectroscopic analysis:* The Fourier-transform infrared (FTIR)  
618 spectroscopic analysis of biomass can provide important information about the changes in the  
619 surface functional groups, before and after the activation process. The untreated biomass usually  
620 exhibits specific absorption bands that correspond to functional groups such as hydroxyl (-OH),



621 carbonyl (C=O), carboxyl (COOH), and aromatic C=C, which are characteristic of cellulose,  
622 hemicellulose, and lignin constituents (Q. Tang et al., 2023). The activation can modify these  
623 absorption bands, indicating structural transformations. It was observed that thermal activation  
624 may leads to dehydration, and thus a decrease in the intensity of the hydroxyl (-OH) peak was  
625 common in the FTIR spectrum, while the formation of new oxygen-containing functional groups  
626 on the activated surface can produce new bands or shift in existing bands. The chemical activation  
627 introduces functional groups from activating agents such as KOH or H<sub>3</sub>PO<sub>4</sub>, leading to additional  
628 peaks or changes in the peak intensities in the FTIR spectra. The disappearance or reduction of  
629 specific peaks associated with the organic functional groups suggested the removal of volatile  
630 matter or the breakdown of organic compounds during activation. Vunain et al. prepared activated  
631 carbon from raw baobab fruit shell biomass using H<sub>3</sub>PO<sub>4</sub> chemical activation process. The FTIR  
632 spectrum of raw baobab fruit shell exhibits strong peaks associated with hydroxyl (-OH) and  
633 carbonyl (C=O) groups of lignocellulose framework. After chemical activation with H<sub>3</sub>PO<sub>4</sub>  
634 followed by carbonization, these peaks either disappeared or shifted, with the appearance of peaks  
635 associated with the activated carbon (Vunain et al., 2017) (**Figure 9**).

636



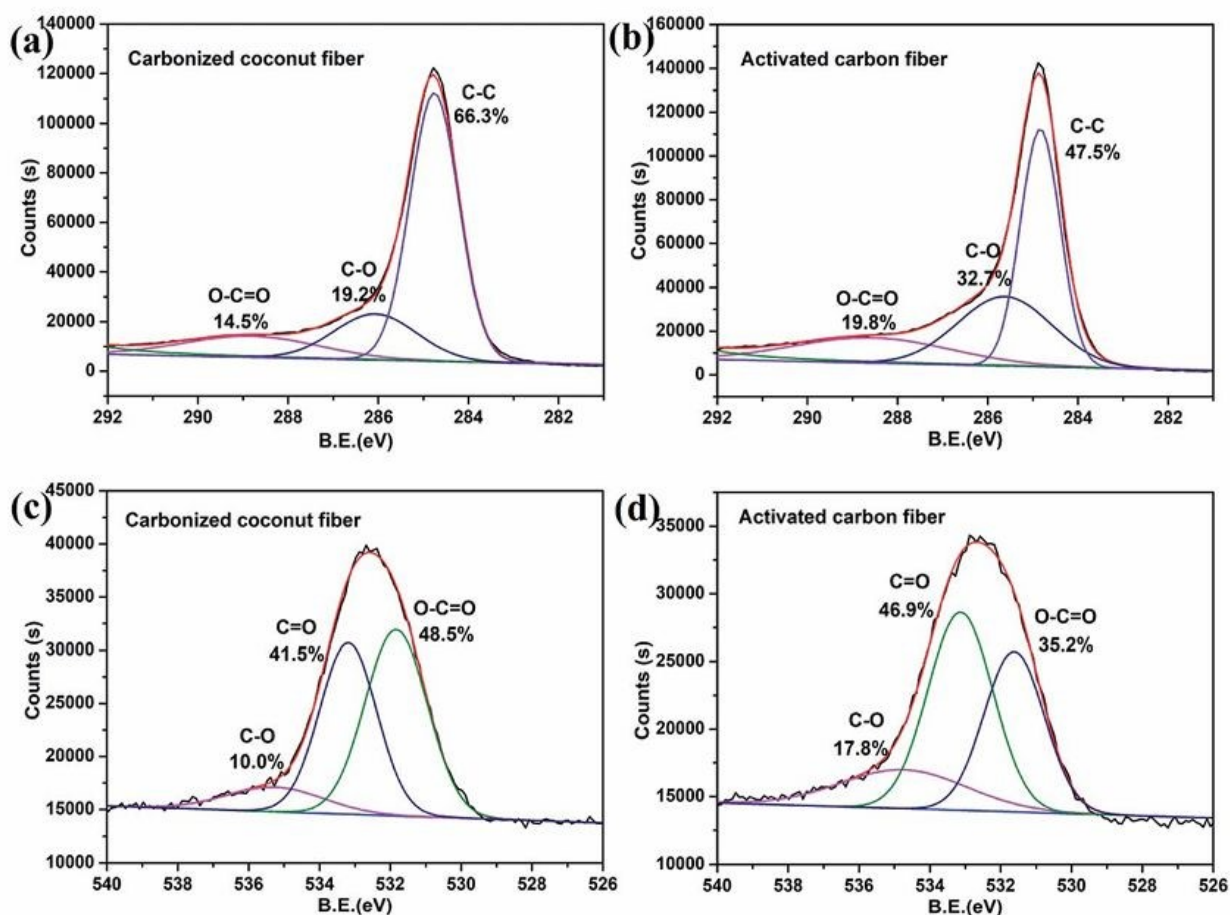
637

638 **Figure 9.** The FTIR spectra of raw baobab fruit shell biomass and its activated carbon in  
639 comparison with commercial activated carbon (Vunain et al., 2017) (Reproduced under Creative  
640 Commons Attribution (CC BY) license <http://creativecommons.org/licenses/by/4.0/>).



641  
642 *4.2.2. X-ray Photoelectron Spectroscopy analysis:* The X-ray Photoelectron Spectroscopy (XPS)  
643 is a powerful analytical technique used to provide valuable insights into the chemical composition  
644 and surface functionalities of biomass and its activated carbon by measuring the binding energies  
645 of electrons emitted from the sample on exposure to X-rays (Gale et al., 2021). The surface  
646 elemental composition of biomass including carbon, oxygen, nitrogen, and other trace elements,  
647 if present, can be evaluated using XPS analysis. It also provides information about the functional  
648 groups such as hydroxyl (-OH), carbonyl (C=O), and carboxyl (-COOH) groups, which are  
649 important for defining its reactivity and potential applications. On the other hand, XPS analysis of  
650 activated carbon describes the changes in the surface chemistry with the activation process. When  
651 compared to the biomass precursor, the activated carbon displayed a higher carbon content with  
652 reduced oxygen functionalities during activation. The XPS can determine the changes in the  
653 elemental composition and functional groups, thus providing significant information about the  
654 structure-property relationships of derived activated carbon and its suitability for applications such  
655 as adsorption or catalysis (Kaur et al., 2024a). Gale et al. explored the elemental analysis and effect  
656 of pyrolysis temperature on the oxygen-containing functional groups of biochar materials, prior to  
657 and after activation with KOH. The XPS analysis revealed that the activation process results in  
658 decreased C-O content of the biochars and activated carbons (Gale et al., 2021). Zhang et al.  
659 compared the elemental composition of carbonized coconut fibres, and the activated carbon  
660 prepared after its KOH treatments. The KOH activation of coconut fibre results in an increase in  
661 oxygen-containing functionalities (L. Zhang et al., 2018) (**Figure 10**).





662

663 **Figure 10.** XPS diagram about C1s and O1s of carbonized coconut fibres and activated carbon  
 664 fibres. (a) and (b) are the C1s XPS spectra and (c) and (d) are the O1s XPS spectra of the two  
 665 samples (L. Zhang et al., 2018) (Reproduced under Creative Commons Attribution-  
 666 NonCommercial 3.0 Unported Licence).

667

### 668 5. Mechanism involved in contaminant removal

669 The mechanism of contaminant removal in biomass and its derived materials mainly  
 670 involves the adsorption process, wherein the contaminants are physically or chemically bound to  
 671 the surface of the biomass adsorbents. In biomass, the porous structure and surface functional  
 672 groups facilitate the adsorption of contaminants from water or air to the surface through  
 673 electrostatic forces, van der Waals interactions, or chemical bonding, thus effectively removing  
 674 them from the surrounding medium (X. Liu et al., 2024). The activated carbons, derived from  
 675 carbonaceous biomass possess an extensive surface area and a high degree of microporosity, which

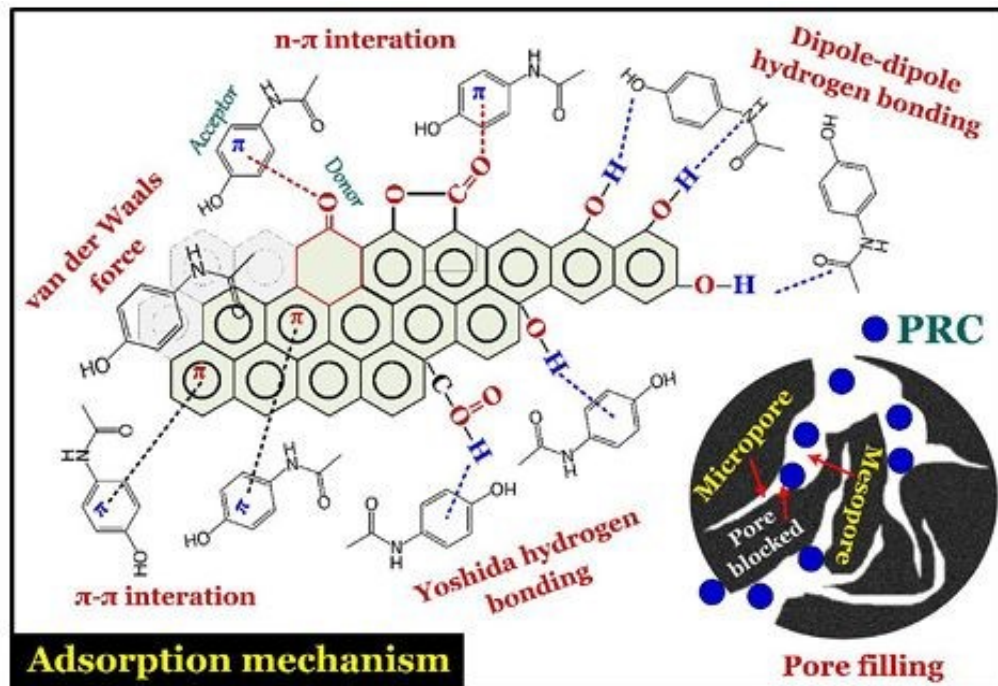


676 enhances their adsorption capacities (Rane et al., 2018). Further, the functionalities present on the  
677 surface of biomass and its activated carbons may undergo chemical reactions with certain  
678 contaminants, or help in the activation of certain oxidizing agents for further aiding in their  
679 removal (Tran et al., 2020). In this section, a general discussion on the various mechanisms  
680 involved in the contaminant removal process by biomass and derived materials has been  
681 performed.

682 **5.1. Adsorptive removal:** The adsorption mechanism with biomass involves the adherence of  
683 contaminant molecules or ions from aqueous solution onto the surface of a solid substrate. When  
684 biomass is used as the substrate, its porous structure provides ample surface area for the adsorption  
685 to occur (Nayak et al., 2024). Biomass can be modified to enhance its adsorption properties by  
686 treating it with acids or bases, which can alter its surface chemistry and increase its affinity for  
687 specific pollutants or molecules. The acid-modified biomass tends to increase the number of  
688 surface acidic functional groups, while base-modified biomass increases basic functional groups,  
689 thereby enhancing adsorption capabilities. Materials derived from biomass, such as biochar and  
690 activated carbon, exhibit excellent adsorption potential due to their high surface area and porous  
691 structure (Heidarinejad et al., 2020). Biochar, a carbon-rich material obtained from the pyrolysis  
692 of biomass, possesses a stable structure and a high surface area and porosity derived from  
693 pyrolysis, enhances absorption through  $\pi$ - $\pi$  interactions and hydrogen bonding, particularly  
694 effective for organic pollutants. Activated carbon, produced by the activation of carbonaceous  
695 materials, undergoes additional processing to create a highly porous structure with active  
696 functional groups which enhance adsorption properties. Activated carbon, with its extensive  
697 microporous and mesoporous structure, facilitates multilayer adsorption through van der Waals  
698 forces,  $\pi$ - $\pi$  interactions, and electrostatic attractions (X. Liu et al., 2024). Understanding these  
699 surface mechanisms is crucial for optimizing the design of adsorbents and advancing wastewater  
700 treatment technologies for effective contaminant removal. Tran et al. suggested the adsorptive  
701 removal of paracetamol (PRC), pharmaceutical contaminant, on the surface of biochar with  
702 included pore-filling, Yoshida hydrogen bonding, dipole-dipole interactions, van der Waals forces,  
703 and  $\pi$ - $\pi$  interactions (Tran et al., 2020) (**Figure 11**).

704





705

706

707 **Figure 11.** The schematic of the mechanism of adsorptive removal of paracetamol onto biochar  
 708 (Tran et al., 2020) (Reproduced with permission, Elsevier, 2020).

709

710 Vo et al. investigated the removal mechanism of Cr(VI) onto biochar and activated carbon.

711 The Cr(VI) removal predominantly relies on the adsorption-coupled reduction, whereby the Cr(VI)

712 ions are partially reduced to Cr(III) ions during the adsorption process. The process of chromium

713 adsorption on biochar and activated carbon is multifaceted, driven primarily by electrostatic forces

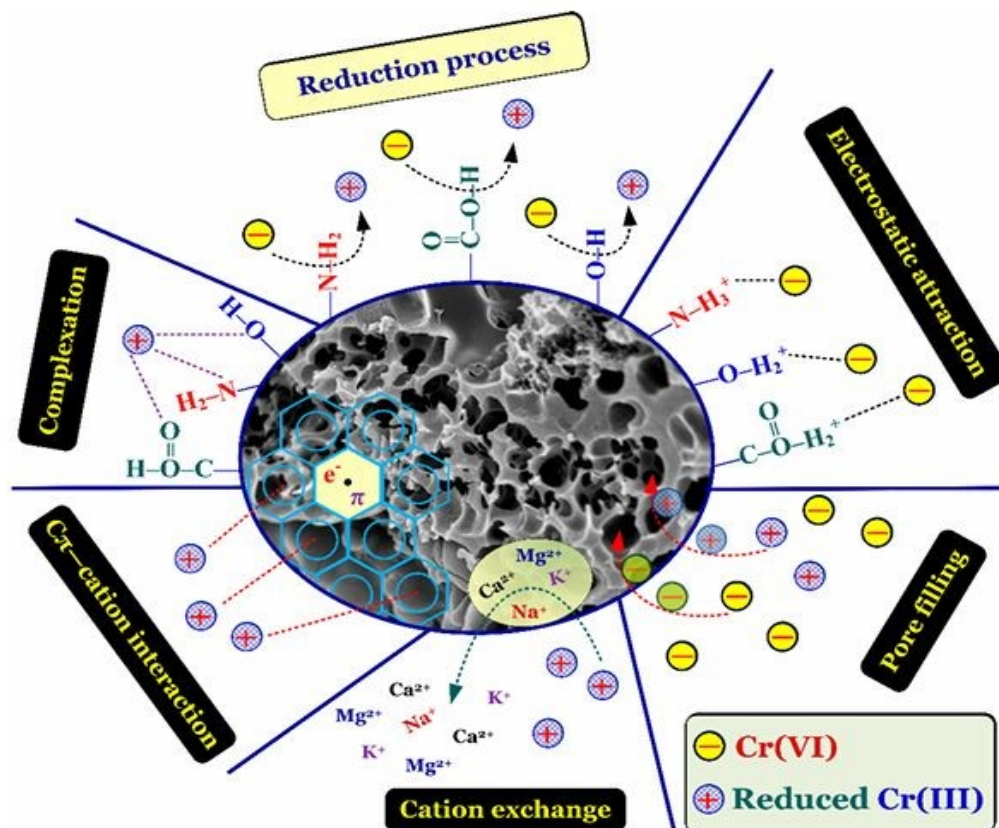
714 that attract Cr(III) ions to the surface. This attraction encompasses several mechanisms, including

715 complexation,  $C\pi$ -cation interaction, cation exchange, and pore filling (Vo et al., 2019) (**Figure**

716 **12).**

717





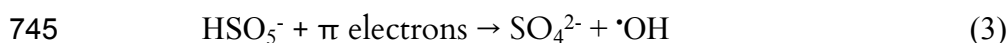
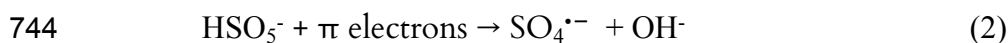
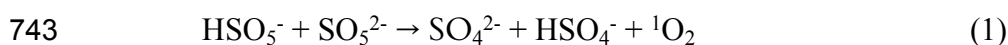
718  
719 **Figure 12.** The schematic of reductive adsorption of Cr(VI) onto biochar and activated carbon (Vo  
720 et al., 2019) (Reproduced under Creative Commons Attribution (CC BY) license  
721 <http://creativecommons.org/licenses/by/4.0/>).

722  
723 **5.2. Degradative removal:** Biomass-derived materials and nanocomposites offer another  
724 promising feature as catalysts in the advanced oxidation processes (AOPs). These materials  
725 efficiently generate a spectrum of reactive oxygen species (ROS), including sulfate radical ( $\text{SO}_4^{\cdot-}$ )  
726 ), hydroxyl radical ( $\cdot\text{OH}$ ), superoxide radicals ( $\text{O}_2^{\cdot-}$ ), and singlet oxygen ( $^1\text{O}_2$ ), through mechanisms  
727 such as Fenton-like reactions or single electron transfer processes (Rani et al., 2025b). These  
728 highly reactive oxygen species play a primary role in the oxidative degradation of diverse  
729 recalcitrant contaminants (Kaur et al., 2024a). Further, the surface functional groups present in the  
730 biomass-derived materials, such as biochar and activated carbons or immobilized metals, serve as  
731 activators for various oxidizing agents like persulfate (PS), peroxymonosulfate (PMS), and  
732 hydrogen peroxide ( $\text{H}_2\text{O}_2$ ), promoting the generation of radical species and thereby enhancing the  
733 oxidative degradation process (Mazarji et al., 2023)

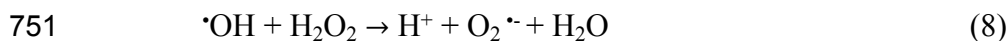
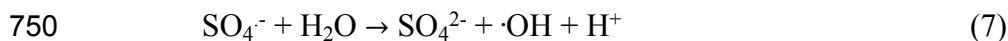
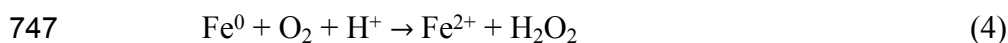


734 Tang et al. investigated two possible pathways involving radical and non-radical processes  
 735 for the degradation of tetracycline (TC) in the FeO<sub>x</sub>@N-BC/PMS system (**Figure 13**). The N-  
 736 biochar contains surface graphite N and pyridine N, which increases the electron density and hence  
 737 facilitates the PMS decomposition by the generation of <sup>1</sup>O<sub>2</sub> (Eq. 1). Further, the electron pair of  
 738 pyridine N transfers π-electrons to PMS to generate SO<sub>4</sub><sup>•-</sup> and <sup>•</sup>OH (Eq. 2-3). The FeO<sub>x</sub>  
 739 nanoparticle on the surface of the biochar also activates PMS to generate various reactive species  
 740 (Eq. 4-8). These reactive oxygen species collectively contribute to the degradation of TC in the  
 741 FeO<sub>x</sub>@N-BC/PMS system (Q. Tang et al., 2023).

742 *Generation of non-radical oxygen species*



746 *Generation of radical oxygen species:*



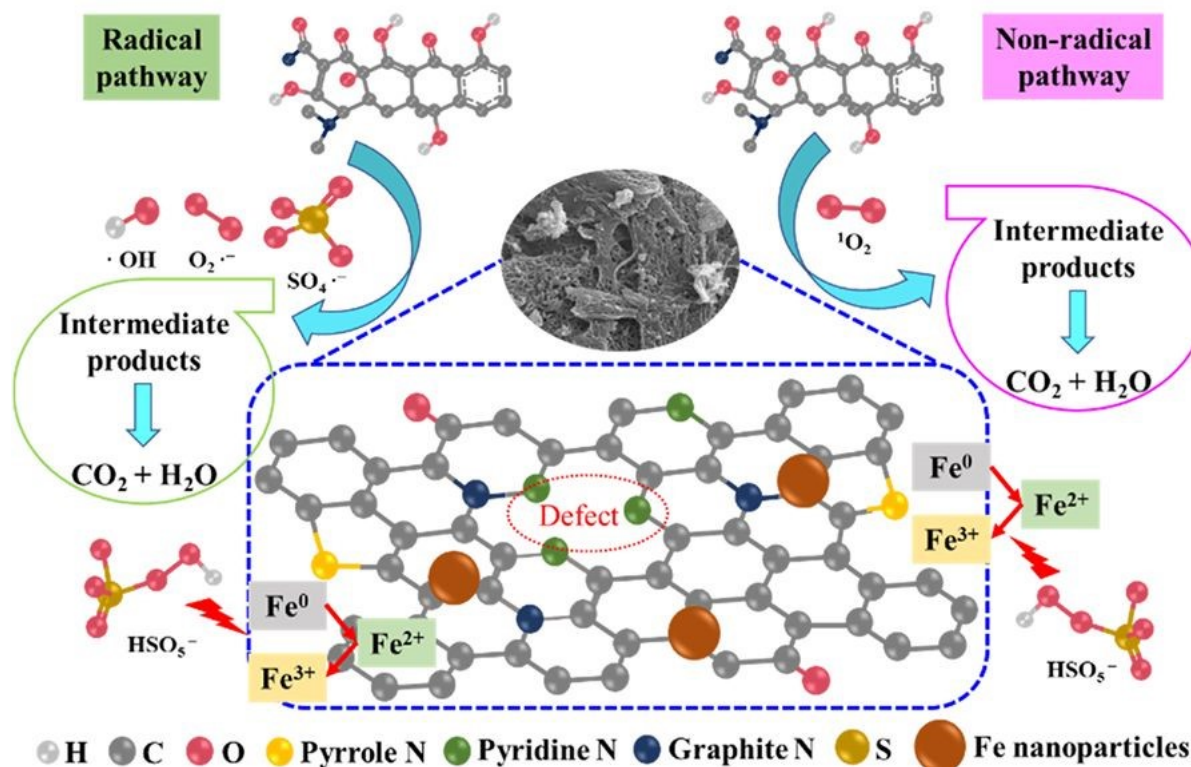
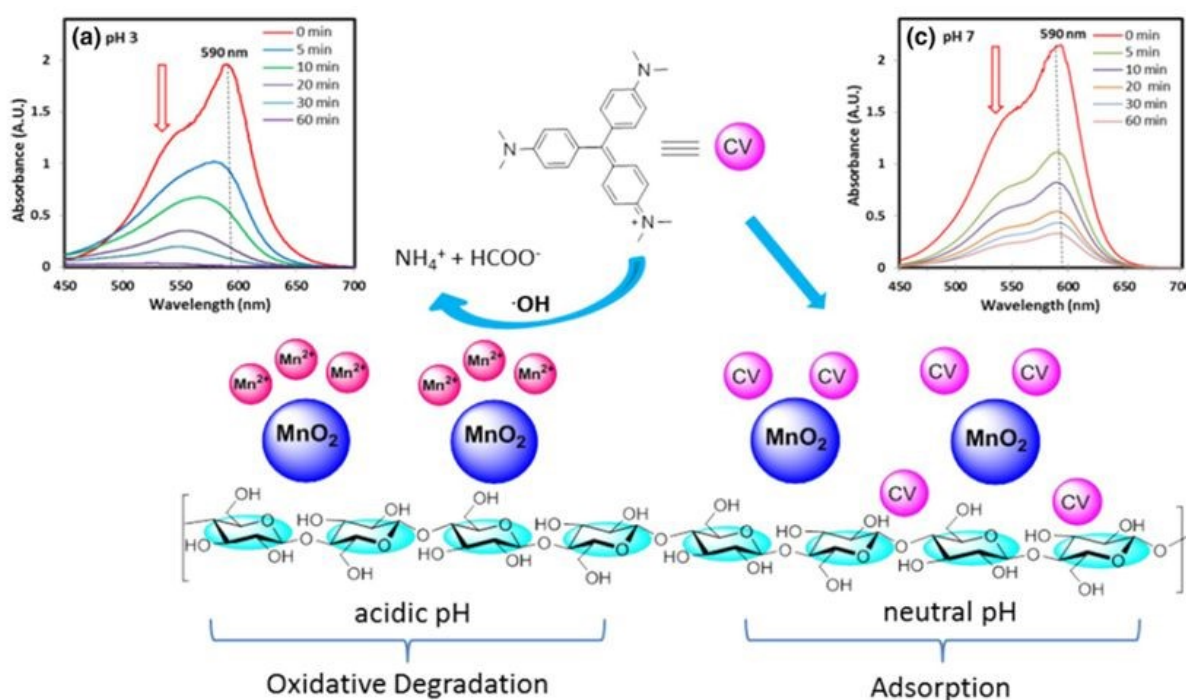


**Figure 13.** The mechanism for tetracycline (TC) degradation via radical and non-radical pathways in the  $\text{FeO}_x\text{@N-BC/PMS}$  system (Q. Tang et al., 2023) (Reproduced with permission, Elsevier, 2023).

Despite these advances, the catalytic degradation field remains underdeveloped in several aspects. Most current studies emphasize radical-mediated degradation ( $\cdot\text{OH}$  and  $\text{SO}_4\cdot^-$ ), while non-radical pathways such as  $^1\text{O}_2$  generation, surface-bound electron transfer, and direct oxidation are relatively less explored, despite their potential for greater selectivity and stability under real environmental conditions. In addition, the contribution of redox-active moieties (e.g., quinones, phenolic groups, graphitic N sites) to catalytic performance remains poorly defined, and requires more systematic investigation using advanced in situ spectroscopic and electrochemical techniques. Furthermore, much of the existing research is conducted in simplified laboratory settings, with limited evaluation of catalyst regeneration, long-term stability, or performance in complex wastewater matrices. Addressing these knowledge gaps will be essential for translating biomass-derived catalysts into practical, scalable, and sustainable degradation technologies.



768 **5.3. Synergy between adsorption and degradation mechanism:** In biomass derived  
 769 nanocomposite materials, the synergy between adsorption efficiencies of biomass derivatives and  
 770 catalytic efficiencies of metal nanoparticles maximizes the contaminant removal efficiencies. The  
 771 porous nature of biomass, biochar, and activated carbon in nanocomposites amplifies the surface  
 772 area, ensuring extensive contact between contaminants and the active sites, where the metal  
 773 nanoparticle mediated chemical reactions break them down. The synergistic interaction enhances  
 774 the overall performance of the composite material, leading to improved removal efficiency and  
 775 degradation rates compared to individual components. Kumar et al. investigated the synergistic  
 776 effect in lignocellulosic biomass and manganese oxide ( $\text{MnO}_2$ ) nanoparticles for the removal of  
 777 crystal violet under a range of pH (Kumar et al., 2023) (**Figure 14**).



779  
 780 **Figure 14.** Synergistic effect originating from the surface adsorptive removal with pistachio  
 781 biomass (PS), and oxidative degradation with  $\text{MnO}_2$  nanoparticles in the  $\text{MnO}_2$ @PS  
 782 nanocomposite (Kumar et al., 2023) (Reproduced with permission, Springer Nature, 2023).

## 784 6. Environmental remediation application of biomass and its surface modified derivative

785 Biomass and its surface-modified derivatives find extensive application in environmental  
 786 remediation processes, serving as versatile and sustainable tools for addressing pollution



787 challenges. Their porous structure, abundant surface functional groups, and diverse chemical  
788 compositions make them effective adsorbents for a wide range of contaminants in soil, water, and  
789 air. The surface modification techniques, such as chemical activation or carbonization,  
790 impregnation with metal nanoparticles, further enhance their adsorption capacity, selectivity, and  
791 reusability. These modified biomass materials exhibit improved performance in removing heavy  
792 metals, organic pollutants, and even emerging contaminants like pharmaceuticals and personal  
793 care products (PPCP's). Further, the biomass-based materials can be utilized in the catalytic  
794 degradation of pollutants through advanced oxidation processes, via exploiting their catalytic  
795 activity and reactive surface sites. In this review section, we will explore the environmental  
796 remediation applications, beginning with raw biomass and advancing to surface-modified biomass  
797 derivatives and metal-immobilized nanocomposites. Throughout this discussion, we will examine  
798 the diverse mechanisms employed for the removal of various organic/inorganic contaminants.

## 799 **6.1 Raw biomass as environmental remediation agent**

800 Raw biomass holds immense potential as an environmental remediation agent due to its  
801 ease of availability and eco-friendly nature (**Table SI 1**). Its properties, including high surface area  
802 and diverse surface functionalities, enables effective adsorption of contaminants from various  
803 environmental sources. Further, the biodegradable nature of these raw biomasses ensures a  
804 minimal environmental impact (Kainth et al., 2024).

805 **6.1.1. Organic contaminant removal:** The removal of organic pollutants, including  
806 pharmaceutical drugs and dyes, is a critical challenge due to their widespread presence and the  
807 detrimental effects on the ecosystems as well as human health. The dyes and the pharmaceutical  
808 drugs are often introduced into water bodies through wastewater discharge or improper disposal,  
809 which can lead to antibiotic resistance, disrupt endocrine systems, and cause adverse health effects  
810 in aquatic organisms and humans. Biomass-based remediation approaches emerge as promising  
811 strategies in addressing these issues.

812 Perez-Millan et al. studied the removal of reactive blue 19 (RB19) and basic blue 3 (BB3)  
813 dyes from water using coconut endocarp (CE) and sugarcane bagasse (SB). The DFT modelling  
814 and characterization reveal that the sulfonate group of these dye molecules and the nitrogen present  
815 in the phenoxazine were found to be the highly reactive areas to interact with the hydroxyl and



816 carboxyl groups of the biomass surface (Pérez-Millán et al., 2023). Kaur et al. performed a study  
817 on the adsorption of methylene blue dye onto rice husk biomass. The Redlich-Peterson isotherm  
818 provides the best fit of adsorption equilibrium data, indicating a multilayer adsorption with a non-  
819 uniform distribution of adsorption heat and affinities over a heterogeneous surface (Kaur, Kalpana,  
820 et al., 2023). The maximum monolayer adsorption capacity was found to be 71.28 mg/g. The best  
821 correlation of kinetics results with pseudo-second-order kinetic models suggesting a chemical  
822 adsorption process. Kaur et al. further explored the utilization of cotton shell (CS) biomass for the  
823 adsorption of terbinafine hydrochloride (TBH). The adsorption efficiency of cotton shell biomass  
824 for TBH was 47.2 mg/g under optimal experimental conditions (Kaur, Hussain, et al., 2023).  
825 Yardimici et al. investigated the adsorption of methylene blue using cinnamon bark biomass (CB).  
826 The best fitting of adsorption data using Langmuir isotherm exhibits the monolayer maximum  
827 adsorption capacity of 123.25 mg/g. The experiment results also suggested the adsorption process  
828 to be of physical nature (Yardımcı & Kanmaz, 2023). Al-Mokhalelati et al. evaluated the  
829 adsorption efficiency of sugarcane bagasse for the removal of methylene blue (MB) dye. The best  
830 correlation of Langmuir isotherm and Halsey adsorption isotherms with equilibrium data indicates  
831 the favourability of multilayer sorption. The thermodynamics study reveals that the adsorption  
832 process is spontaneous and endothermic in nature (Al-Mokhalelati et al., 2021). Tang et al.  
833 investigated the removal efficiency of methylene blue (MB) with walnut -shell biomass. The  
834 adsorption of MB onto walnut shell biomass was chemical in nature, as described using the  
835 Dubinin-Radushkevich isotherm model and pseudo-second-order kinetic model. The  
836 thermodynamic data indicated that the adsorption was favourable, spontaneous, and exothermic in  
837 nature (R. Tang et al., 2017). Uddin et al. used mango leaf biomass for the adsorption of MB dye.  
838 The Langmuir isotherm describes the best fitting for the experimental equilibrium data with  
839 maximum monolayer adsorption capacity of 156 mg/g. Further, the removal of MB with mango  
840 leaf biomass follows a pseudo second order kinetics (Uddin et al., 2021). Deng et al determined  
841 the effect of cotton stalk biomass (CS) for the removal of methylene blue dye (MB). The  
842 equilibrium adsorption efficiency of Methylene Blue (MB) onto the cotton shell reached 147.06  
843 mg/g under optimal experimental conditions. The equilibrium adsorption and kinetics data were  
844 best fitted with Langmuir and pseudo-second order models, respectively (H. Deng et al., 2011).  
845 Ertas et al. studied methylene blue (MB) adsorption using cotton waste (CW), cotton stalk (CS),  
846 and cotton dust (CD). The cotton dust was the most effective in MB removal. The CS adsorption



847 data fit both Freundlich ( $R^2 = 0.967$ ) and Langmuir ( $R^2 = 0.997$ ) isotherms, while CW and CD fit  
848 Freundlich. The thermodynamic parameters showed positive  $\Delta G^\circ$  for CS and negative for CW and  
849 CD, with positive  $\Delta H^\circ$  and  $\Delta S^\circ$  for all sorbents (Ertaş et al., 2010).

850  
851 **6.2.2. Inorganic contaminant removal:** Inorganic contamination, particularly heavy metals, poses  
852 a significant threat to environmental and human health due to their persistence and toxicity. The  
853 biomass can effectively remove heavy metals from aqueous solutions due to its metal-binding  
854 capabilities through processes such as adsorption, precipitation, or ion exchange. These eco-  
855 friendly approaches not only mitigates pollution, but also offers a sustainable means of metal  
856 recovery and recycling, contributing to both environmental remediation and resource conservation  
857 efforts (Ali Redha, 2020).

858         Kebir et al. studied chromate adsorption onto red peanut skin (RPS) in a fixed-bed column.  
859 The optimal conditions were 100 mg/L Cr(VI) concentration and a 10 cm bed height, with high  
860 column adsorption capacity. The Bohart-Adams model ( $R^2 > 0.98$ ) indicated surface diffusion as  
861 the rate-limiting step. The RPS demonstrated a Cr(VI) removal capacity of 26.23 mg/g at pH 5.35,  
862 with electrostatic interactions being crucial in the adsorption process (Kebir et al., 2023).  
863 Mahmood-ul-Hassan et al. studied heavy metal adsorption (Cd, Cr, Pb) using banana stalks, corn  
864 cob, and sunflower achene. The Langmuir model showed banana stalks had the highest Pb  
865 adsorption (21-60 mg/g), with the order of sorption capacities being  $Pb > Cr > Cd$  (Mahmood-ul-  
866 Hassan et al., 2015). Akram et al. used cotton shell biomass for lead (Pb) removal from wastewater,  
867 achieving up to 90% efficiency in 90 min with a 1000 mg/L dose and 1 mg/L Pb concentration.  
868 The Freundlich isotherm model best describes Pb sorption. The SEM analysis revealed a  
869 microporous structure with a 45 m<sup>2</sup>/g BET surface area and 2.3 mm pore size, involving  
870 complexation and ion exchange mechanisms (Akram et al., 2019). Ye et al. studied the adsorptive  
871 removal of cadmium (Cd) with rice husk biomass. The equilibrium adsorption data was best fit  
872 with Langmuir isotherm with Cd(II) adsorption capacity of 73.96 mg/g at pH 6.5 (Ye et al., 2010).  
873 Cao et al. used wheat straw biomass for the adsorptive removal of lead from wastewater. The  
874 results indicate that the Pb(II) adsorption capacities at an adsorbent dosage of 0.2 g/L onto wheat  
875 straw biomass was 46.33 mg/g. The adsorption mechanism involves processes such as ion  
876 exchange and precipitation (Cao et al., 2019). Banerjee and coworkers investigated the adsorption  
877 of Cr(VI) onto a pistachio shell with a fixed bed column. The experimental results indicate that



878 adsorption capacity increases with increase in column bed depth (Banerjee et al., 2018).  
879 Ezeonuegbu et al. studied sugarcane bagasse for Pb(II) and Ni(II) removal from untreated  
880 wastewater. The Freundlich and pseudo-second order models best describe the adsorption  
881 isotherms and kinetics for Pb(II) and Ni(II), with capacities of 1.61 mg/g and 123.46 mg/g,  
882 respectively (Ezeonuegbu et al., 2021). Varsihini et al. investigated cerium(III) biosorption using  
883 prawn carapace (PC) and corn style (CS). The maximum adsorption capacities were 218.3 mg/g  
884 for PC and 180.2 mg/g for CS. The Freundlich and Langmuir models best fit PC and CS data,  
885 respectively, with physisorption indicated and the process found to be endothermic and  
886 spontaneous (Varsihini C et al., 2014).

## 887 **6.2 Surface modified biomass as environmental remediation agent.**

888 Surface modification of raw biomass via physical, chemical or physicochemical activation  
889 processes results in increased removal efficiencies of the biomass. This section of the review will  
890 discuss the environmental remediation applications of surface modified biomass with special  
891 emphasis on the mechanistic aspects and methodologies used for evaluating the enhanced surface  
892 efficacies (**Table SI 2**).

893 **6.2.1. Physical modified biomass:** Physical modification of biomass includes its conversion to  
894 biochar or hydrochar. This conversion process involves various physical modifications such as  
895 pyrolysis, size reduction, hydrothermal treatment, etc., intended to improve the quality of the  
896 resulting biochar or hydrochar such as surface area, density, stability and purity, and thus to  
897 enhance the efficiency of the contaminant removal process (Masoumi et al., 2021). This part of  
898 review discusses various literature reports on the use of physically modified biomass for  
899 environmental contaminant removal.

900 Ju et al. explored the use of biochar derived from tobacco stalks for removing  
901 sulfamethazine (SMT) through a dual approach of adsorption and degradation. The  
902 characterization revealed that this biochar had a porous structure with a high specific surface area  
903 of 905.6 m<sup>2</sup>/g and active functional groups on its surface. These features significantly enhanced  
904 SMT removal, facilitated by the generation of hydroxyl radicals (-OH) observed in the EPR  
905 spectrum, which played a crucial role in the degradation of SMT (Ju et al., 2023). Dias et al.  
906 examined biochars made from pine nut shells for adsorbing Methylene blue (MB) dye. They found  
907 that pyrolysis temperature influenced the thermal stability and weight loss of the biochar, with



908 remaining mass percentages of 78%, 45%, 41%, 36%, and 32% at temperatures of 221 °C, 309 °C,  
909 350 °C, 420 °C, and 488 °C, respectively. Adsorption experiments showed that biochar produced  
910 at lower pyrolysis temperatures had higher removal efficiency, achieving up to 53.9 mg/g (Dias et  
911 al., 2024). Liu et al. studied shiitake mushroom bran biochar prepared at various pyrolysis  
912 temperatures (300 °C, 500 °C, 700 °C) for tetracycline removal. The research revealed that the  
913 surface chemistry of the biochar varied with temperature. The adsorption data for BC300 and  
914 BC500 fit the Langmuir isotherm, indicating monolayer adsorption, while BC700 fit the  
915 Freundlich isotherm, suggesting heterogeneous adsorption. The kinetic studies indicated that the  
916 pseudo second-order model best described the adsorption, signifying chemisorption across all  
917 biochar (X. Liu et al., 2023). Qin et al. assessed biochar from rape straw, activated with KOH, for  
918 tetracycline (TC) removal. This biochar had a specific surface area of 1531 m<sup>2</sup>/g, abundant oxygen-  
919 containing functional groups, and a graphite-like structure. The adsorption data matched both  
920 pseudo second-order kinetics and the Freundlich isotherm, indicating a chemisorption process and  
921 heterogeneous adsorption. The thermodynamic analysis showed that TC adsorption was  
922 spontaneous and endothermic, with hydrogen bonding, electrostatic interactions, and pi-pi  
923 interactions contributing to the adsorption mechanism (Y. Qin et al., 2022). Tomczyk et al.  
924 investigated tetracycline removal using sunflower biomass-derived biochar, modified with vitamin  
925 C, hydrogen peroxide, and silver nanoparticles. Although modifications decreased the biochar's  
926 surface area and pore volume, they increased the presence of acidic and basic functional groups,  
927 enhancing electrostatic interactions with tetracycline. The vitamin C-modified biochar  
928 demonstrated superior adsorption efficiency compared to other modifications (Tomczyk &  
929 Szewczuk-Karpisz, 2022). Chen et al. studied tannic acid-modified rice straw biochar for  
930 tetracycline removal. The modification increased oxygen-containing functions on the biochar  
931 surface, improving adsorption capacity. Adsorption followed the Freundlich and Elovich models,  
932 suggesting physisorption through electrostatic interactions, pi-pi interactions, and hydrogen  
933 bonding (J. Chen et al., 2021). Hoslet et al. analysed biochar from food and plant waste for  
934 tetracycline removal. Produced via pyrolysis at 300 °C, the biochar achieved an adsorption  
935 capacity of 9.45 mg/g for tetracycline. The kinetic and isotherm models indicated an Elovich  
936 kinetics and Freundlich isotherm, reflecting a combination of chemisorption and heterogeneous  
937 adsorption (Hoslett et al., 2021). Zhang et al. investigated cow manure biochar for tetracycline  
938 removal. Biochar produced at 300 °C, 500 °C, and 700 °C showed differences in surface area,



939 charge, and pore volume. The adsorption mechanism involved electrostatic interactions, hydrogen  
940 bonding, pore filling, and pi-pi interactions. Freundlich and pseudo-second-order kinetics models  
941 best described the adsorption, suggesting heterogeneous surface properties and chemical  
942 adsorption (P. Zhang et al., 2019). Chen et al. evaluated the biochar from pomelo peels, activated  
943 with KOH, for carbamazepine removal. Characterizations indicated that activation temperature  
944 affected biochar morphology. Adsorption data fit the pseudo-second-order kinetics and Langmuir  
945 isotherm models, suggesting physisorption through intra-particle diffusion. Thermodynamic  
946 analysis showed the adsorption process was spontaneous and exothermic (D. Chen et al., 2017).

947 Cao and colleagues studied the adsorption of Pb(II) using different wheat straw-based  
948 materials: acid-modified wheat straw (WS), wheat straw biochar (WS-BC), and ball-milled wheat  
949 straw biochar (WS-BC+BM). They found that pyrolysis and ball milling significantly enhanced  
950 Pb(II) removal, with capacities of 46.33 mg/L for WS, 119.55 mg/L for WS-BC, and 134.68 mg/L  
951 for WS-BC+BM. Pb(II) removal was primarily driven by ion exchange, precipitation, and  
952 complexation with acid functional groups (AFGs). The carbonization and ball milling improved  
953 ion exchange and precipitation, but high adsorbent concentrations led to competition between these  
954 mechanisms. Further, the acid modification increased Pb(II) complexation, as indicated by FTIR  
955 peak shifts showing changes in AFG bond energies (Cao et al., 2019).

### 956 **6.2.2. Chemical modified biomass:**

957 Chemical modification of biomass involves changing its chemical composition through  
958 various chemical treatments to improve its properties, typically focusing on increasing surface area  
959 or porosity. Chemical activation of biomass can involve agents such as mineral acids and oxidants,  
960 including HNO<sub>3</sub>, H<sub>2</sub>O<sub>2</sub>, HClO, H<sub>2</sub>SO<sub>4</sub>, H<sub>3</sub>PO<sub>4</sub>, and HCl, as well as alkalis like NaOH, KOH, LiOH,  
961 Na<sub>2</sub>SiO<sub>3</sub>, Na<sub>2</sub>CO<sub>3</sub>, and various oxides. Depending on the type of reagent used, the surface of the  
962 biomass may develop either positive or negative charges and thus can be used for the remediation  
963 of target contaminants. This section of the review provides a summary of the literature on  
964 chemically activated biomass and its applications in environmental remediation.

965 Kaur et al. studied how varying sodium hydroxide (NaOH) treatment parameters affect the  
966 efficiency of rice husk in adsorbing methylene blue (MB) from water. NaOH-treated rice husks  
967 were prepared by adjusting NaOH concentration, treatment time, and temperature. The results



968 showed that the higher NaOH concentration, longer treatment duration, and increased temperature  
969 improved the adsorption process. The maximum monolayer adsorption capacity for NaOH-treated  
970 rice husk was 123.39 mg/g, compared to 71.28 mg/g for untreated husk (Kaur, Kalpana, et al.,  
971 2023). Yang et al. developed porous biosorbents from hickory wood using a one-step ball milling  
972 process with acidic or alkaline treatments. These modifications enhanced the biomass's oxygen-  
973 containing functional groups, porous structure, and capacity to remove crystal violet (CV, 476.4  
974 mg/g) and Congo red (CR, 221.8 mg/g) dyes from water at neutral pH. The adsorption followed  
975 Freundlich isotherm and pseudo second-order kinetic models, indicating surface complexation (X.  
976 Yang et al., 2022). Jiang et al. created activated carbon from seaweed biomass (SWAC) via NaOH  
977 activation for methylene blue removal, achieving a high specific surface area of 1238.491 mg/g  
978 and a 98.56% MB removal efficiency at 30 °C and pH 5. The high adsorption capacity is linked to  
979 graphitic N sites and interactions such as  $\pi$ - $\pi$  stacking and electrostatic forces (D. Jiang et al.,  
980 2023). Homagai et al. evaluated chemically modified rice husks for crystal violet removal, finding  
981 adsorption capacities of 62.85 mg/g for charred rice husk, and 90.02 mg/g for xanthate rice husk  
982 at pH 10 (Homagai et al., 2022). Al-Mokhalelati et al. examined the sugarcane bagasse (SB) before  
983 and after alkaline treatment, and observed temperature-dependent MB adsorption increase  
984 (Al-Mokhalelati et al., 2021). Deng et al. examined cotton stalk (CS), cotton stalk treated with  
985 sulphuric acid (SCS), and cotton stalk treated with phosphoric acid (PCS) for their effectiveness  
986 in removing methylene blue (MB) from aqueous solutions. The study revealed that the porosity of  
987 activated materials can be easily regulated by employing different activation agents. The initial pH  
988 of the aqueous solution minimally influenced the adsorption capacity of both SCS and PCS,  
989 whereas it significantly affected the removal efficiency of CS. The MB adsorption capacity  
990 followed the order of SCS > PCS > CS (H. Deng et al., 2011).

991 Mahmood et al. evaluated the adsorption effectiveness of unmodified and chemically  
992 modified banana stalks, corn cobs, and sunflower achenes for cadmium (Cd), chromium (Cr), and  
993 lead (Pb) in wastewater. The modifications involved treating the agricultural wastes with sodium  
994 hydroxide (NaOH) combined with nitric acid (HNO<sub>3</sub>) and sulfuric acid (H<sub>2</sub>SO<sub>4</sub>) to boost their  
995 adsorption capabilities. The results showed that NaOH-modified materials had better adsorption  
996 capacity than those modified with acids. The highest adsorption capacities were observed in the  
997 order of Pb > Cr > Cd. The enhancement in Pb adsorption capacity was most significant in banana  
998 stalks (117%) and corn cobs (62%), while sunflower achenes showed only a 34% increase,



999 possibly due to their higher lignin content. This suggests that chemical modification improved  
1000 adsorption through increased active binding sites and new functional groups (Mahmood-ul-Hassan  
1001 et al., 2015). Ye et al. tested natural and alkali-modified rice husks for Cd(II) removal. The  
1002 modified rice husks showed enhanced Cd(II) adsorption (125.94 mg/g) compared to natural rice  
1003 husks (73.96 mg/g) due to structural changes from alkali treatment (Ye et al., 2010). Yardımcı and  
1004 Kanmaz studied the use of waste cinnamon bark biomass (CB) and manganese dioxide-  
1005 immobilized CB ( $\text{MnO}_2@CB$ ) for methylene blue (MB) dye removal. The  $\text{MnO}_2@CB$  with a  
1006 higher surface area (145.2  $\text{m}^2/\text{g}$ ) compared to CB (45.59  $\text{m}^2/\text{g}$ ), demonstrated better adsorption  
1007 capacity. The Langmuir isotherm best fitted CB data, while  $\text{MnO}_2@CB$  followed the Freundlich  
1008 isotherm, with both adsorbents showing kinetics best described by the pseudo-second-order model  
1009 (Yardımcı & Kanmaz, 2023).

1010 **6.2.3. Physico-chemical modified biomass:** Physico-chemical modification of biomass involves  
1011 a combination of physical and chemical treatment processes. The modification led to changes in  
1012 biomass properties such as increased surface area, enhanced reactivity, improved stability, or  
1013 altered chemical composition (Gale et al., 2021). This section of the review discusses literature on  
1014 physico-chemically modified biomass and its applications in various environmental remediation  
1015 efforts.

#### 1016 **6.2.3.1. Organic contaminant removal**

1017 Yurtay and Kılıç investigated the production of activated carbon (AC) from agricultural  
1018 residues such as hazelnut shells (HS), rice husks (RH), and corn stalks (CS) using chemical  
1019 activation with potassium hydroxide (KOH) and carbonization at 950 °C. This study aimed to  
1020 explore the effectiveness of these ACs in removing metronidazole from aqueous solutions. The  
1021 BET analysis revealed significant improvements in surface area of hazelnut shell AC (1650  $\text{m}^2/\text{g}$ ),  
1022 rice husk AC (2573  $\text{m}^2/\text{g}$ ), and corn stalk AC (2304  $\text{m}^2/\text{g}$ ) due to chemical activation. The  
1023 adsorption isotherms showed that both HS-AC and RH-AC best fit the Langmuir model, while  
1024 CS-AC was best described by the Freundlich model. The kinetic studies indicated that the pseudo-  
1025 second-order model was the most accurate for metronidazole adsorption. Thermodynamic analysis  
1026 confirmed that the adsorption process was exothermic and spontaneous (Yurtay & Kılıç, 2023).  
1027 Bouzidi et al. examined the adsorption of ibuprofen (IBP) and paracetamol (PCM) using activated  
1028 carbon derived from *Erythrina speciosa* tree pods activated with zinc chloride ( $\text{ZnCl}_2$ ). The AC



1029 displayed a high BET surface area of 795.1 m<sup>2</sup>/g. The double-layer model (DLM) suggested multi-  
1030 molecular adsorption for both IBP and PCM, indicating the simultaneous accommodation of each  
1031 functional group on the adsorbent's surface. The energy evaluations indicated that the adsorption  
1032 was predominantly physical (Bouzidi et al., 2023). Astuti et al. developed activated carbon from  
1033 pineapple leaves, cocoa shells, and coconut shells using microwave heating and ZnCl<sub>2</sub> activation.  
1034 This method created a template effect that resulted in uniformly distributed pores. The specific  
1035 surface area and porosity were enhanced, with the average pore sizes being 2.41 nm for coconut  
1036 shell AC, 1.75 nm for cocoa shell AC, and 1.79 nm for pineapple crown leaf AC. All four activated  
1037 carbons showed the best fit with the Langmuir isotherm for methyl violet adsorption (Astuti et al.,  
1038 2023). Kandasamy and colleagues evaluated the effectiveness of carbons derived from goat and  
1039 sheep dung, activated with KOH and ZnCl<sub>2</sub> using a hydrothermal method, for methylene blue dye  
1040 removal. The KOH-activated carbon from goat dung achieved a 99.6% removal rate with a  
1041 maximum adsorption capacity of 24.81 mg/g. Adsorption equilibrium data best fit the Freundlich  
1042 model for ZnCl<sub>2</sub>-activated carbon, the Langmuir model for KOH-activated carbon, and the  
1043 Dubinin-Radushkevich model for hydrothermally carbonized carbon. The pseudo-second-order  
1044 model described the kinetic data well, indicating a chemisorption process (Kandasamy et al.,  
1045 2023). Cui et al. employed bamboo-derived activated carbon aerogel (BACA) for tetracycline  
1046 hydrochloride (TCH) removal. Synthesized through KOH activation of bamboo cellulose aerogel,  
1047 BACA demonstrated a strong fit with the Langmuir isotherm and pseudo-second-order kinetics,  
1048 indicating monolayer adsorption and chemisorption. Thermodynamic analysis suggested that the  
1049 adsorption process was spontaneous and endothermic (Cui et al., 2022).

1050 Al Sarjidi et al. explored the removal of various emerging pollutants such as diclofenac,  
1051 amoxicillin, carbamazepine, and ciprofloxacin using activated carbon derived from pomegranate  
1052 peels, with laccase immobilization (LMPP). When compared to unloaded pomegranate peel-  
1053 derived AC (MPP), LMPP demonstrated superior pollutant removal efficiency. The adsorption  
1054 process followed the Langmuir isotherm and first-order kinetics, also characterized as spontaneous  
1055 and endothermic (Al-sareji et al., 2023). Zhang et al. synthesized amorphous activated carbon from  
1056 sesame straw using KOH and Ca(OH)<sub>2</sub> co-activation. The activated carbon exhibited a surface  
1057 area of 935 m<sup>2</sup>/g and high adsorption capacities for ofloxacin, ciprofloxacin, and enrofloxacin. The  
1058 kinetic and adsorption data indicated heterogeneous and multilayer adsorption, with the pseudo-  
1059 second-order and Sips models providing the best fits. The DFT calculations revealed hydrogen



1060 bonding, electrostatic interactions, and  $\pi$ - $\pi$  interactions as key mechanisms in drug removal (Y.  
1061 Zhang et al., 2022). Srinivasan et al. evaluated activated carbon from *Thevetia neriifolia* Juss wood  
1062 for adsorbing direct orange 102 dye (DO102). The adsorption capacity increased with temperature,  
1063 suggesting an endothermic process. The pseudo-second-order model provided a more accurate fit  
1064 compared to the pseudo-first-order model, and the Langmuir model best described the adsorption  
1065 with capacities ranging from 9.44 mg/g to 33 mg/g (Yusop et al., 2021). Yusop et al. studied the  
1066 adsorptive removal of methylene blue using activated carbon derived from Acacia wood (AWAC).  
1067 The AWAC exhibited a BET surface area of 1045.56 m<sup>2</sup>/g and a mesopore surface area of 689.77  
1068 m<sup>2</sup>/g. The adsorption followed the Langmuir isotherm and pseudo-second-order kinetics, with film  
1069 diffusion being the main process. The Langmuir monolayer capacity was 338.29 mg/g, and the  
1070 process was exothermic (Yusop et al., 2021). Piriya and colleagues investigated malachite green  
1071 adsorption on zinc chloride-activated carbon from coconut. The activation process increased  
1072 surface area to 544.66 m<sup>2</sup>/g and adsorption capacity to 39.683 mg/g. The Freundlich isotherm and  
1073 intraparticle diffusion model best described the data. The coconut shell AC showed effective dye  
1074 removal from industrial effluents, suggesting it as a viable alternative to commercial activated  
1075 carbon (Sangeetha Piriya et al., 2021).

1076 Baloo et al. compared activated carbons from empty fruit bunches (EFB) and mesocarp  
1077 fibers (MF) of oil palm for removing methylene blue (MB) and Acid Orange 10 (AO10). The MF  
1078 AC had a higher BET surface area (552.7222 m<sup>2</sup>/g) compared to EFB (35.6328 m<sup>2</sup>/g). The  
1079 adsorption of dyes followed the pseudo-second-order kinetic model, with the Langmuir model  
1080 better representing MB adsorption for MF (Baloo et al., 2021). Abatal et al. created a carbonaceous  
1081 material from *Haematoxylum campechianum* bark using phosphoric acid activation and thermal  
1082 treatment at 500 °C. This material, with a mixed graphitized/amorphous phase, showed high  
1083 adsorption capacities for phenol, 4-chlorophenol, and 4-nitrophenol. The Langmuir model  
1084 provided the best fit, with a maximum phenol adsorption capacity of 94.09 mg/g (Abatal et al.,  
1085 2020). Geczo et al. derived activated carbon from cashew nut shells using H<sub>3</sub>PO<sub>4</sub> activation. The  
1086 study highlighted the importance of acidic groups in acetaminophen removal, showing that highly  
1087 acidic groups facilitated hydrolysis while lower concentrations led to physisorption (Geczo et al.,  
1088 2021). Yang et al. utilized one-step H<sub>3</sub>PO<sub>4</sub> activation to produce porous carbon from corn straw  
1089 for tetracycline removal. The AC showed a high surface area of 463.89 m<sup>2</sup>/g and demonstrated  
1090 excellent adsorption performance. Both pseudo-second-order and Langmuir models fit the data



1091 well, with the process being endothermic and spontaneous (Q. Yang et al., 2020). Abo El Naga et  
1092 al. examined sugar cane bagasse-derived activated carbon (SCG-AC) for diclofenac sodium  
1093 removal. The SCG-AC, produced via  $\text{ZnCl}_2$  activation, showed good fits with the Langmuir and  
1094 pseudo-second-order models. The pH influenced the adsorption mechanism, with hydrophobic  
1095 interactions dominating at low pH and electrostatic/hydrogen bonding at moderate pH (Abo El  
1096 Naga et al., 2019).

1097 El Mouchtari et al. developed a bio-composite material for removing pharmaceuticals from  
1098 water. This composite, combining activated carbon from *Argania Spinosa* nutshells and  
1099 commercial  $\text{TiO}_2$ , demonstrated high efficacy for diclofenac, carbamazepine, and  
1100 sulfamethoxazole removal through adsorption and photodegradation (El Mouchtari et al., 2020).  
1101 Darweesh and Ahmed synthesized granular activated carbon from *Phoenix dactylifera* L. stones  
1102 using microwave-assisted KOH activation. This material exhibited a high levofloxacin adsorption  
1103 capacity of 100.38 mg/g. The adsorption process was influenced by initial levofloxacin  
1104 concentration and flow rate, with the Thomas and Yoon-Nelson models providing better fits than  
1105 Adams-Bohart (Darweesh & Ahmed, 2017). Jung et al. produced granular activated carbon from  
1106 spent coffee grounds using calcium-alginate beads. This material effectively removed Acid Orange  
1107 7 (AO7) and methylene blue (MB) from water, with adsorption controlled by pore diffusion. The  
1108 carbon showed high capacity and was effective in both environmental and economic terms (Jung  
1109 et al., 2016).

1110

#### 1111 6.2.3.2. Inorganic contaminant removal

1112 Elewa and colleagues studied activated carbons (AC) from rice husk for removing Fe(III)  
1113 and Mn(II) from aqueous solutions. The AC was produced at 700 °C in an electric furnace with  
1114 activation with NaOH (AC-1), acetic acid (AC-2), phosphoric acid (AC-3), and without chemical  
1115 activation (AC-4). The AC-4 showed superior efficiency compared to the other. The adsorption  
1116 followed pseudo-second-order kinetics and Langmuir isotherm, with an endothermic process  
1117 (Elewa et al., 2023). Huang et al. prepared N, P co-doped activated carbon from cabbage waste  
1118 using  $\text{H}_3\text{PO}_4$  activation via hydrothermal method. The carbon, with a high BET surface area (1400  
1119  $\text{m}^2/\text{g}$ ), showed over 97.5% efficiency in adsorbing antibiotics within 10 min, with adsorption being  
1120 a chemical process (K. Huang et al., 2023). Neolaka and colleagues synthesized activated Carbon  
1121 Mesopore Adsorbent (ACMA) from Kesambi wood for Pb(II) removal. The characterization



1122 analysis confirmed the presence of oxygenated functional groups with carbon and oxygen as  
1123 predominant elements, a rough surface with amorphous structure, low crystallinity, and  
1124 mesoporous size. The adsorption followed the pseudo second-order model and Langmuir isotherm  
1125 signifying a homogeneously energetic adsorbent surface. Thermodynamic studies suggest  
1126 processes being exothermic and spontaneous (Neolaka et al., 2021). Kharrazi and colleagues  
1127 studied adsorbent carbons from Elm tree sawdust treated with various chemicals to remove Pb(II)  
1128 and Cr(VI) from water. Acid treatment enhanced Cr(VI) absorption, while alkali treatment  
1129 improved Pb(II) adsorption, with a pseudo-second-order model best describing the process.  
1130 Treatment with  $MgCl_2$  resulted in a mesoporous AC capable of absorbing Pb(II) up to 1430 mg/g  
1131 (Kharrazi et al., 2021). Thompson et al. found  $H_3PO_4$ -activated biomass (groundnut shell, yam  
1132 peels, cassava peels) as a cost-effective alternative for  $Pb^{2+}$  removal from wastewater. The process  
1133 was endothermic, rapid, and best fit the pseudo second-order model. The optimal temperature for  
1134 ion removal from yam peels and groundnut shells was identified as 60 °C, while temperature  
1135 exerted no discernible effect on the adsorption process of cassava peels (Thompson et al., 2020).  
1136 Wang et al. studied Cr(VI) adsorption on coconut shell-derived Granular Activated Carbon (GAC),  
1137 finding a redox reaction that forms a  $Cr_2O_3$  layer on GAC, limiting Cr(VI) uptake. It was suggested  
1138 that nanoscale AC or porous nanoscale AC pellets could offer promising solutions for effective  
1139 Cr(VI) water treatment applications (Y. Wang et al., 2020). Salomón-Negrete and colleagues  
1140 developed avocado-based adsorbents for fluoride removal through pyrolysis, finding that  
1141 pyrolyzed adsorbents outperformed  $CO_2$ -activated ones. Fluoride adsorption was influenced by  
1142 carbonization temperature and involved silicon-based ligand exchange and electrostatic  
1143 interactions (Salomón-Negrete et al., 2018). Sajjad et al. synthesized activated carbon from  
1144 pistachio wood waste using  $NH_4NO_3$  activation, showing it has a higher surface area with well-  
1145 developed pores for better  $Hg^{2+}$  adsorption than commercial carbon, making it a cost-effective,  
1146 efficient adsorbent for hazardous metals (Sajjadi et al., 2018). Norouzi et al. converted Date Press  
1147 Cake into activated carbon using NaOH, achieving a high surface area (2025.9  $m^2/g$ ) and Cr(VI)  
1148 adsorption capacity (282.8 mg/g), best described by Elovich and Redlich-Peterson models  
1149 (Norouzi et al., 2018). Gebrewold and colleagues evaluated chemically modified rice husk and  
1150 corn cob activated carbon for fluoride adsorption. They found Langmuir and pseudo-second-order  
1151 models best fit the data, with adsorption influenced by intraparticle and surface diffusion  
1152 (Gebrewold et al., 2019). Vunain et al. found that activated carbon from baobab fruit shells,



1153 chemically activated with phosphoric acid was more economical compared to commercially  
1154 available activated carbon, and efficiently removes  $\text{Cu}^{2+}$  ions from aqueous solution (Vunain et al.,  
1155 2017). Thamarai et al. investigates Pb(II) removal using Physically Modified (PMSB) and  
1156 Chemically Modified Seaweed Biosorbents (CMSB). Optimal conditions were 303 K, pH 5.0, and  
1157 dosages of 2.5 g/L (PMSB) and 1 g/L (CMSB), with contact times of 80 and 40 min. Maximum  
1158 adsorption capacities were 149.8 mg/g (PMSB) and 175.5 mg/g (CMSB) (Thamarai et al., 2024a).  
1159 Further, the Cd(II) removal was also compared using CMSB and PMSB. The CMSB (19.682  $\text{m}^2/\text{g}$ )  
1160 and PMSB (14.803  $\text{m}^2/\text{g}$ ) showed optimal adsorption at 303 K, pH 6.0, with dosages of 1 g/L and  
1161 2.5 g/L. The maximum capacities reached 181.6 mg/g (PMSB) and 151.2 mg/g (CMSB), following  
1162 Langmuir isotherm and pseudo-second-order kinetics (Thamarai et al., 2024c).

1163 The free radicals, generated during the charring process, also play a crucial role in biochar's  
1164 surface chemistry. The surface free radicals can react with certain chemical substances, like  
1165 hydrogen peroxide and persulfate, thereby facilitating the degradation of organic contaminants  
1166 (Xing et al., 2019). This mechanism, primarily driven by electrochemical analysis, indicates that  
1167 high-temperature-pyrolysis-derived biochar possess electron-accepting capabilities mediated by  
1168 free radicals. The biochar not only facilitates the degradation or transformation of pollutants by  
1169 serving as a catalyst for electron transfer, but can also directly react with pollutants, significantly  
1170 impacting their environmental fate. Although a limited relevant literature is available, surface  
1171 redox-active moieties predominantly contribute to biochar's redox activity. These moieties activate  
1172 certain oxidants to produce reactive radicals like  $\cdot\text{OH}$  and  $\text{SO}_4^{\cdot-}$  and can also directly engage with  
1173 pollutants through non-radical pathways (Q. Tang et al., 2023).

1174 Zhou et al. created biochar from  $\alpha$ -cellulose and sodium lignosulfonate via microwave  
1175 pyrolysis, achieving 99.9% oxytetracycline degradation in 15 min. The removal pathway was  
1176 based on a non-free radical pathway involving  $^1\text{O}_2$  as the main active species responsible for OTC  
1177 removal, that was promoted by enriched thiophene S and C = O groups. The enrichment of carbon  
1178 vacancies further improved the removal of pollutant through direct electron transfer that  
1179 accelerated the PMS activation (Q. Zhou et al., 2024). Xu et al. studied poplar flour (PF) and  
1180 walnut shell flour (WSF) biochar, finding that higher pyrolysis temperatures improved their  
1181 performance in activating peroxymonosulfate (PMS) for diclofenac (DCF) removal. Poplar  
1182 biochar (PB) outperformed walnut shell biochar (WSB) due to better porosity, functional groups,  
1183 and conductivity. The non-radical mechanism, including singlet oxygen ( $^1\text{O}_2$ ) and electron



1184 transfer, was key to DCF degradation (Xu et al., 2023). Dong et al. investigated N-doped biochar  
1185 (N-biochar) from soybean biomass for atrazine removal via enhanced catalytic ozonation. The key  
1186 factors included delocalized  $\pi$ -electrons and functional groups that generated reactive oxygen  
1187 species (ROS) like hydroxyl radicals ( $\cdot\text{OH}$ ) and singlet oxygen ( $^1\text{O}_2$ ) (Dong et al., 2023). Zeng et  
1188 al. studied plant-based biochar (PBC) for tetracycline (TC) degradation via peroxydisulfate  
1189 (PMS) activation, noting a large surface area ( $725\text{ m}^2/\text{g}$ ) and effective pyrrolic-N in enhancing  
1190 PMS activation and degrading TC in a non-radical reaction pathway (Zeng et al., 2023). Hou et al.  
1191 synthesized graphene/biochar composites for persulfate (PS) activation and phenol degradation,  
1192 with non-radical pathways and  $\pi$ - $\pi^*$  EDA interactions playing crucial roles (Hou et al., 2023). Dai  
1193 et al. studied periodate-based advanced oxidation for BPA degradation using wheat straw-derived  
1194 biochar. A metastable C-PI\* intermediate was identified as the primary oxidant, with BPA  
1195 donating electrons. The DFT calculations confirmed strong van der Waals interactions between PI  
1196 and biochar with an observed synergistic effect, whereby an adsorption takes place on the biochar  
1197 surface, while the PI facilitates the degradation of BPA (Dai et al., 2023). Wang and Chen  
1198 synthesized a nitrogen-doped biochar from pomelo peel, achieving 95% sulfamethoxazole  
1199 removal in 30 min via PMS activation, with high activity due to graphitic and pyrrolic N, carbonyl  
1200 groups, and a large surface area ( $738\text{ m}^2/\text{g}$ ) (W. Wang & Chen, 2022). Gao et al. investigated BPA  
1201 degradation using ferric chloride-modified rice husk biochar activated by PMS. With 1.0 g/L  
1202 catalyst and 1.6 g/L PMS, over 97% of 20 mg/L BPA was removed in 150 min, involving  $\text{SO}_4^{\cdot-}$ ,  
1203  $\cdot\text{OH}$ ,  $\text{O}_2^{\cdot-}$ , and  $^1\text{O}_2$  (Y. Gao et al., 2022). Hu et al. studied tetracycline hydrochloride (TCH)  
1204 degradation using biochar from passion fruit shells pyrolyzed at  $900\text{ }^\circ\text{C}$  under  $\text{N}_2$ . The metal-free  
1205 biochar activated PMS, achieving 90.9% TCH removal via singlet oxygen-mediated oxidation and  
1206 non-radical pathways, including direct electron transfer and  $\text{O}_2^{\cdot-}/^1\text{O}_2$  generation (Hu et al., 2021).  
1207 Cai et al. studied pyrrolic N-rich biochar from waste bean dregs for BPA removal, finding that N-  
1208 Biochar/PDS was most effective under neutral and acidic conditions. The ESR and quenching tests  
1209 showed  $\text{SO}_4^{\cdot-}$ ,  $\cdot\text{OH}$ , and  $^1\text{O}_2$  had minimal impact. The DFT results revealed enhanced electron  
1210 donation and charge density in N-Biochar, improving PDS activation and ROS formation (Cai et  
1211 al., 2021). Xu et al. developed a cost-effective N-doped biochar from sawdust via single-step  
1212 calcination. The biochar, with high graphitic and pyridinic nitrogen, activates PMS for degrading  
1213 BPA, phenol, acetaminophen, and sulfamethoxazole. The EPR and quenching tests identified  
1214 ROS, especially singlet oxygen, as key in degradation (Xu et al., 2020). Ding et al. studied nitrogen



1215 and sulphur-doped rice straw biochar for metolachlor degradation using PMS. N-doping improved  
1216 PMS interaction, while S-doping disrupted charge balance. The DFT showed hydroxyl radicals  
1217 and singlet oxygen were crucial, with HPLC-TOF-MS revealing the degradation pathways through  
1218 hydroxylation, hydrolytic dechlorination, N-dealkylation, dehydroxylation, demethylation, and  
1219 amide bond cleavage mechanism (Ding et al., 2020). Li et al. used biomass-derived activated  
1220 carbon (BAC) for sulfamethoxazole removal with PDS. The BAC-PDS complex facilitated  
1221 electron transfer, with EPR detecting ROS like  $\cdot\text{OH}$ ,  $\text{SO}_4^{\cdot-}$ , and  $^1\text{O}_2$ . In real water, common anions  
1222 had minimal impact on SMX degradation, providing insights into ROS generation (Y. Li et al.,  
1223 2023).

1224

#### 1225 **6.2.4. Nanostructured biomass**

1226 The immobilization of metal or metal oxide nanoparticles on the surface of the biomass  
1227 and its derived materials such as biochar, hydrochar and activated carbon, holds significant  
1228 importance for various applications, particularly in the fields of environmental remediation, and  
1229 catalysis. This process involves the deposition of nanoparticles onto the surface of these  
1230 carbonaceous materials through various methods such as carbothermal reduction, hydrothermal  
1231 method, etc. (Singh, 2023). The biomass derived materials have ample surface area and functional  
1232 groups for the immobilization of nanoparticles, facilitating strong interactions and stability. The  
1233 metal or metal oxide nanoparticles, such as iron, copper, silver, titanium dioxide, manganese oxide,  
1234 etc. can be selectively deposited onto the surface of biomass derived materials to impart specific  
1235 properties or functionalities (Kaur et al., 2024a). For instance, metal nanoparticles immobilized on  
1236 activated carbon can serve as highly efficient catalysts for organic transformations, while metal  
1237 oxide nanoparticles supported on biochar can act as effective adsorbents for pollutant removal in  
1238 water treatment applications. The immobilization of nanoparticles on the carbonaceous materials  
1239 not only enhances their stability and reusability but also expands their range of applications,  
1240 contributing to the development of sustainable and efficient technologies for various  
1241 environmental and industrial challenges (**Table SI 3**) (Kumar et al., 2023). The incorporation of  
1242 nanoparticles onto biomass or its carbon-rich derivatives significantly alters their physicochemical  
1243 properties, thereby enhancing their remediation performance. Nanostructuring contributes to: (a)  
1244 increased surface area and hierarchical porosity provide abundant active sites for pollutant binding,



1245 while functional groups on nanoparticles (e.g.,  $-\text{OH}$ ,  $-\text{O}-$ , metal oxides) strengthen interactions  
1246 through hydrogen bonding, electrostatic attraction, or  $\pi-\pi$  stacking; (b) metal and metal oxide  
1247 nanoparticles act as catalytic centers, activating oxidants such as  $\text{H}_2\text{O}_2$ , persulfate, or PMS, and  
1248 generating reactive oxygen species (ROS) such as  $\cdot\text{OH}$ ,  $\text{SO}_4^{\cdot-}$ ,  $\text{O}_2^{\cdot-}$ ,  $^1\text{O}_2$ . The porous biomass matrix  
1249 supports nanoparticle dispersion and prevents agglomeration, ensuring sustained catalytic activity;  
1250 (c) biomass facilitates pre-concentration of pollutants onto its surface, while immobilized  
1251 nanoparticles drive catalytic degradation, leading to faster and more complete removal compared  
1252 to either mechanism alone; (d) carbonized biomass with graphitic domains can act as an electron  
1253 shuttle, accelerating redox reactions at nanoparticle sites and enhancing pollutant breakdown.

#### 1254 6.2.4.1. Raw biomass immobilized with metal/metal oxide nanoparticles

1255 Kaur et al. studied the adsorption of terbinafine hydrochloride (TBH) using cotton shell  
1256 powder (CS), nano zerovalent copper (nZVC), and zerovalent copper on CS (ZVC@CS).  
1257 ZVC@CS effectively concentrated or removed TBH under acidic conditions ( $\text{pH} < 5$ ) through  
1258 hydrophobic and electrostatic interactions. Analysis revealed external mass transport as the  
1259 limiting step for TBH adsorption, with ZVC@CS achieving a  $q_{\text{max}}$  of 285.3 mg/g, better than other  
1260 adsorbents (Kaur, Hussain, et al., 2023). Kumar et al. also studied how pistachio shell biomass  
1261 combined with nano- $\text{MnO}_2$  (nMPP) affects crystal violet (CV) removal. The adsorption capacity  
1262 of pistachio shell works synergistically with oxidative degradation efficacy of  $\text{MnO}_2$  to enhance  
1263 CV removal. Under acidic conditions, oxidative CV degradation occurs via  $\cdot\text{OH}$  radicals from  
1264 nMPP, while neutral pH conditions show CV adsorption. This combination shows promise for  
1265 organic contaminant remediation in water (Kumar et al., 2023). Kumar et al. evaluated the  
1266 nanocomposite of pistachio shell powder combined with nano-zerovalent copper for the chromium  
1267 remediation. The immobilized nano-copper (ZVC@PS) showed superior Cr(VI) adsorption (110.9  
1268 mg/g) compared to pistachio shell powder alone (27.95 mg/g). The XPS and spectroscopy  
1269 confirmed the presence of synergistic effect from Cr(VI) adsorption and reduction to Cr(III),  
1270 enhancing remediation efficiency (Kumar et al., 2021). Kaur et al. explored a synergistic approach  
1271 combining pistachio shell powder adsorption with ZVI or ZVC in Fenton-like and PMS activation  
1272 processes to enhance tetracycline (TCH) degradation. ZVI@PS-PMS showed superior  
1273 performance with high contaminant removal, faster degradation ( $0.34 \text{ min}^{-1}$ ), and 86% COD  
1274 removal, due to effective adsorption, catalysis, and PMS activation for advanced oxidation (Kaur,  
1275 Kumar, et al., 2023) (Table SI 4).



1276

#### 1277 **6.2.4.2 Surface modified biomass immobilized with metal/metal oxide nanoparticles**

1278 Surface-modified biomass immobilized with metal/metal oxide nanoparticles offers a promising  
1279 approach for environmental remediation, combining the high surface area and reactivity of  
1280 nanoparticles with the renewable, sustainable properties of biomass to enhance pollutant removal  
1281 and treatment efficiency (**Table 2**). Further, the catalytic efficiencies of these metal/metal oxide  
1282 nanoparticles in advanced oxidation processes significantly enhance the overall pollutant removal  
1283 processes (**Table 3**).

##### 1284 **6.2.4.2.1. Adsorptive removal**

1285 Sutradhar et al. synthesized biochar from pre-roasted sunflower seed shells (SFS) and  
1286 peanut shells (PNS) using direct pyrolysis and assessed their effectiveness for textile dye removal  
1287 from wastewater. The FTIR and XRD analysis showed degradation of cellulosic and lignin  
1288 components, and XPS indicated a 13.8% increase in C-C/C=C in SFS and 22.6% in PNS biochar,  
1289 reflecting polyaromatic structure condensation. The PNS biochar demonstrated superior dye  
1290 removal efficiency, enhanced by pyridinic-N, graphitic-N, hydrogen bonding, and electrostatic  
1291 interactions (Sutradhar et al., 2024). Qu et al. evaluated the rice straw-derived biochar (BC) for  
1292 ciprofloxacin (CIP) removal from water, finding a maximum Langmuir adsorption capacity of  
1293 747.64 mg/g at pH 5. The adsorption involved C=O groups facilitating electrostatic,  $\pi$ - $\pi$ , and  
1294 hydrogen bond interactions. Incorporating TiO<sub>2</sub> to create Ti-RSB composite with enhanced  
1295 photocatalytic performance, and CIP removal efficiency across pH 5-9, owing to improved biochar  
1296 surface functionality (K. Qu et al., 2023). Sen synthesized a magnetic bamboo charcoal iron oxide  
1297 nanocomposite for removing the cationic methylene blue (MB) dye from synthetic wastewater.  
1298 The pseudo-second-order model described batch adsorption kinetics well. Both Freundlich and  
1299 Langmuir isotherms fit the equilibrium data, with a maximum capacity of 111.11 mg/g. The  
1300 composite's 80.25% desorption efficiency suggests its potential for treating industrial dye effluents  
1301 (Sen, 2023). Nascimento et al. assessed magnetic nanohybrids of sugar cane straw biochar and  
1302 Fe<sub>3</sub>O<sub>4</sub> (Fe<sub>3</sub>O<sub>4</sub>@BC) for removing congo red (CR) and indigo carmine (IC) dyes. Adsorption  
1303 process following pseudo-second-order and Elovich models, involved chemisorption and was best  
1304 described by the Sips model, with endothermic and favourable thermodynamics (Do Nascimento  
1305 et al., 2023).



1306 Dai et al. studied the impact of modification and magnetization on rice straw-derived  
1307 biochar for tetracycline (TC) removal. Enhanced surface area and pore volume improved hydrogen  
1308 bonding and pore-filling effects, achieving an adsorption capacity of 98.33 mg/g (Dai et al., 2020).  
1309 Hao et al. investigated hazelnut shell biomass-derived biochar with zerovalent iron (ZVI@HS) for  
1310 removing oxytetracycline, chlortetracycline, and tetracycline. The adsorption process followed  
1311 Langmuir isotherm and pseudo-second-order kinetics, with up to 95% removal efficiency,  
1312 indicating spontaneous and endothermic processes (Hao et al., 2021). Nyirenda et al. used  
1313 sulphuric acid to create activated carbon from maize cobs, then deposited silver on silica  
1314 nanoparticles to form the Ag-SiO<sub>2</sub>@AC nanocomposite. This composite efficiently removed Pb<sup>2+</sup>,  
1315 Cd<sup>2+</sup>, Cu<sup>2+</sup>, and Zn<sup>2+</sup> from solutions, with maximum adsorption capacities of 81.30, 87.72, 84.75,  
1316 and 81.97 mg/g, respectively. The adsorption process was spontaneous, endothermic, and physical  
1317 in nature (Nyirenda et al., 2022). Masoudian and colleagues efficiently removed Congo Red and  
1318 Phenol Red dyes from water using TiO<sub>2</sub> nanoparticles on activated carbon from watermelon rind.  
1319 The dye removal followed the Langmuir equation and second-order kinetics (Masoudian et al.,  
1320 2019). Altıntig et al. created magnetic activated carbon (Fe@AC) from ZnCl<sub>2</sub>-activated corn shell,  
1321 showing high Methylene Blue adsorption (357.1 mg/g) with fast uptake, endothermic process, and  
1322 good reusability up to four cycles (Altıntig et al., 2017). Saini et al. prepared zinc oxide-loaded  
1323 activated carbon (ZnO@AC) via hydrothermal synthesis to remove Orange G (OG) and  
1324 Rhodamine B (Rh-B) dyes. The Langmuir model best fit the adsorption isotherms, with capacities  
1325 of 153.8 mg/g for OG and 128.2 mg/g for Rh-B. The adsorption followed the pseudo-second-order  
1326 model, and thermodynamic studies indicated spontaneous, and endothermic removal of dyes (Saini  
1327 et al., 2017).

1328 Liu et al. evaluated magnetic zerovalent iron-supported biochar from peanut hull for  
1329 chromium (VI) and trichloroethane (TCE) removal. The mechanisms included pore-filling,  
1330 hydrophobic partitioning, and reductive degradation. The XPS showed Cr(VI) reduction to Cr(III)  
1331 and a redox reaction with a decrease in Fe<sup>0</sup> peak, suggesting effective, cost-efficient water  
1332 treatment (Y. Liu et al., 2019). Qian et al. conducted an investigation into the reduction and  
1333 adsorption of hexavalent chromium using a combination of palladium (Pd) and silicon-rich biochar  
1334 derived from rape straw, supported by nanoscale zerovalent iron (nZVI). The presence of silicon  
1335 and Pd facilitated the reduction of Cr(VI), attributed to the Fe<sup>0</sup> crystallinity within the structures  
1336 of nZVI (Qian et al., 2019). Zhang et al. investigated the adsorption and reduction of uranium



1337 using biochar-supported zerovalent iron (ZVI@BC) prepared through an environmentally friendly  
1338 carbothermal reduction process. The maximum adsorption capacity reached 55.58 mg/g, with the  
1339 Langmuir isotherm providing the best fit. Moreover, X-ray photoelectron spectroscopy (XPS)  
1340 spectra obtained after adsorption revealed simultaneous occurrences of adsorption and reduction,  
1341 as both U(IV) and U(VI) were detected in the spectra (H. Zhang et al., 2019).



1342 **Table 2.** Surface modified biomass nanocomposite as environmental remediating agents

| Nanocomposite                      | Contaminant            | Optimized condition |            |             |            | % Removal | Ref.                         |
|------------------------------------|------------------------|---------------------|------------|-------------|------------|-----------|------------------------------|
|                                    |                        | pH                  | Dose (g/L) | Conc. (g/L) | Time (min) |           |                              |
| Fe@BC                              | Methylene blue         | 10                  | 0.4        | 0.02        | 120        | 80.25     | (Sen, 2023)                  |
| Fe <sub>3</sub> O <sub>4</sub> @BC | Congo red              | 7                   | 0.2        | 0.01        | 1440       | 72        | (Do Nascimento et al., 2023) |
| Fe <sub>3</sub> O <sub>4</sub> @BC | Indigo carmine         | 10                  | 0.2        | 0.01        | 1440       | 27        |                              |
| Fe-BC                              | Tetracycline           | 3-10                | 1.2        | 0.05        | 60         | 98.3      | (Dai et al., 2020)           |
| ZVI@HS                             | Oxytetracycline        | 6.5                 | 4          | 0.4         | 60         | 96.7      | (Hao et al., 2021)           |
| ZVI@HS                             | Chlortetracycline      | 6.5                 | 4          | 0.4         | 60         | 95.5      |                              |
| ZVI@HS                             | Tetracycline           | 6.5                 | 4          | 0.4         | 60         | 95        |                              |
| Fe/Pd@RS                           | 1,2,4-Trichlorobenzene | 5.58                | 0.16       | 0.01        | 2880       | 98.8      | (Shang et al., 2020)         |
| ZVI@PH                             | Chromium,              | 4.4                 | 1          | 0.3         | 6000       | 100       | (Y. Liu et al., 2019)        |
| ZVI@PH                             | Trichloroethene        | 4.4                 | 1          | 0.3         | 6000       | 100       |                              |
| Pd/Fe@CS                           | Trichlorobenzene       | 3.7-10.3            | 0.1        | 0.1         | 1440       | 93        | (L. Han et al., 2019)        |
| Co/Fe@MB                           | Cefotaxime             | 6                   | 0.5        | 0.02        | 380        | 99.46     | (H. Wu et al., 2018)         |
| Fe@PSd                             | Sulfamethoxazole       | 4.5                 | 0.004      | 0.02        | 1440       | 55.6      | (Reguyal & Sarmah, 2018)     |
| Ag/Fe@MB                           | Cefotaxime             | 6.1                 | 1          | 0.04        | 90         | 91.3      | (H. Wu et al., 2017)         |
| Ni/Fe@WS                           | 1,1,1-Trichloroethane  | 6                   | 1          | 0.2         | 180        | 99.3      | (H. Li et al., 2017)         |





|                         |                    |     |        |       |      |       |                            |
|-------------------------|--------------------|-----|--------|-------|------|-------|----------------------------|
| ZVI@RS                  | 2,4-Dinitrotoluene | 7.4 | 4      | 0.04  | 1440 | 40-50 | (Oh et al., 2017)          |
| ZVI@RS                  | 4-Chlorophenol     | 7.4 | 4      | 0.052 | 1440 | 40-50 |                            |
| Ni/Fe@SB                | Decabromodiphenyl  | 6   | 2      | 0.002 | 10   | 91.2  | (Yi et al., 2017)          |
| nZVI/Pd@Si-RS           | Chromium           | 4   | 0.01   | 0.05  | 480  | 95.9  | (Qian et al., 2019)        |
| nZVI@BC                 | Uranium            | 6   | 2      | 0.02  | 120  | 99.9% | (H. Zhang et al., 2019)    |
| Fe-Mn-Zn-Cu@BC          | Thiamethoxam       | 3   | 0.4    | 0.05  | 20   | 100   | (Chai et al., 2023)        |
| ZVI@BC                  | Cadmium            | 6   | 2      | 0.1   | 480  | 96.2  | (Tian, Peng, et al., 2023) |
| ZVI@BC                  | Oxytetracycline    | 4   | 1.5    | 0.1   | 480  | 98.8  |                            |
| Ag-SiO <sub>2</sub> @AC | Copper             | 5.5 | 1      | 0.01  | 200  | 97    | (Nyirenda et al., 2022)    |
| Ag-SiO <sub>2</sub> @AC | Cadmium            | 5.5 | 1      | 0.01  | 200  | 100   |                            |
| Ag-SiO <sub>2</sub> @AC | Lead               | 5.5 | 1      | 0.01  | 200  | 95    |                            |
| Ag-SiO <sub>2</sub> @AC | Zinc               | 5.5 | 1      | 0.01  | 200  | 99    |                            |
| ZVI@CS                  | Methyl orange      | 7   | 0.0005 | 0.2   | 60   | 97.9  | (B. Zhang & Wang, 2019)    |
| TiO <sub>2</sub> @AC    | Phenol red         | 4.3 | 0.04   | 0.046 | 8.2  | 100   | (Masoudian et al., 2019)   |
| TiO <sub>2</sub> @AC    | Congo red          | 4.3 | 0.04   | 0.015 | 8.2  | 100   |                            |
| Fe@AC                   | Methylene blue     | 4   | 0.4    | 0.1   | 30   | 100   | (Altıntug et al., 2017)    |
| ZVI@AC                  | Arsenic            | 7   | 2      | 0.1   | 90   | 99    | (X. Li et al., 2023)       |
| ZnO@AC                  | Orange G           | 7   | 0.4    | 0.05  | 30   | 92    | (Saini et al., 2017)       |
| ZnO@AC                  | Rhodamine B        | 7   | 0.4    | 0.05  | 30   | 99    |                            |

1344

1345 **6.2.4.2.2. Catalytic removal**

1346 Shang et al. tested biochar-supported nanoscale zero-valent iron (nZVI) and palladium (Pd)  
1347 composites for removing 1,2,4-trichlorobenzene (1,2,4-TCB). The modified biochar achieved up  
1348 to 98.8% removal, primarily through Fe/Pd nanoparticle reduction and biochar adsorption (Shang  
1349 et al., 2020). Han et al. elucidate the impact of Pd/Fe supported by biochar on the elimination of  
1350 1,2,4-trichlorobenzene (1,2,4-TCB). A method involving both Pd/Fe electrochemical  
1351 dechlorination and biochar adsorption is employed to eradicate trichlorobenzene (L. Han et al.,  
1352 2019). Wu et al. studied cefotaxime degradation using Co/Fe bimetallic nanoparticles supported  
1353 on modified biochar. The composite efficiently removed cefotaxime (CFX) through adsorption  
1354 and degradation, with Co/Fe nanoparticles breaking down adsorbed CFX. The  $\beta$ -lactam ring  
1355 instability of CFX under strong reducing agents was analysed via HPLC-ESI-MS (H. Wu et al.,  
1356 2018). Reguyal and Sarmah assessed the magnetic biochar (Fe@PSd) from pine sawdust (PSd) for  
1357 sulfamethoxazole (SMX) removal. The SMX sorption was pH-dependent, with hydrophobic and  
1358  $\pi$ - $\pi$  electron interactions significantly influencing the process due to SMX's aromatic and  
1359 heterocyclic structures (Reguyal & Sarmah, 2018). Wu et al. investigated the degradation and  
1360 adsorption of Cephalexin (CLX) using Ag/Fe bimetallic nanoparticles supported on modified  
1361 biochar. Ag/Fe@MB effectively removed CLX through reduction and adsorption, with  
1362 degradation products analysed by LC-MS (H. Wu et al., 2017).

1363 Li et al. evaluated the reductive degradation of 1,1,1-trichloroethane (1,1,1-TCA) using  
1364 biochar-supported Ni/Fe bimetallic nanoparticles. Nickel assisted zero-valent iron (ZVI) corrosion  
1365 and thus generated atomic hydrogen that forms hydride-like species, enhancing 1,1,1-TCA  
1366 reduction. Inorganic ions had minimal effects, but  $\text{NO}_3^-$  and humic acid significantly inhibited  
1367 degradation (H. Li et al., 2017). Oh et al. used rice straw biochar-supported zerovalent iron for  
1368 removing nitro explosives and halogenated phenols from contaminated water. The XPS showed  
1369 no change in  $\text{Fe}^0$  redox properties after co-pyrolysis. The biochar facilitated contaminant reduction  
1370 through  $\text{Fe}^0$  was proved more efficient than direct  $\text{Fe}^0$  reduction due to enhanced electron transfer  
1371 mediated by biochar's surface functional groups (Oh et al., 2017). Yi et al. examined  
1372 decabromodiphenyl ether degradation using biochar-supported Ni/Fe (BC@Ni/Fe) nanoparticles.  
1373 The BC@Ni/Fe showed higher removal efficiency than Ni/Fe alone, with stepwise debromination



1374 as the primary mechanism, complemented by the adsorption process (Yi et al., 2017). Li et al. used  
1375 biochar-supported Fe@BC to activate persulfate (PDS) for degrading Acid Orange 7. The  
1376 maximum removal (98%) occurred in 20 min under optimal conditions (50 mg/L AO7, 1 g/L  
1377 catalyst, 20 mM PMS, and pH 6). The process involves electron transfer and a non-radical  
1378 pathway, primarily generating singlet oxygen ( $^1\text{O}_2$ ) for degradation (Z. Li et al., 2024). Qu et al.  
1379 assessed the efficiency of CuO-supported biochar (CuO@BC) for activating persulfate (PS) to  
1380 degrade bisphenol A (BPA). The free radical and ESR analyses showed involvement of  $\cdot\text{OH}$ ,  $\text{SO}_4^{\cdot-}$   
1381,  $\text{O}_2^{\cdot-}$ , and  $^1\text{O}_2$  in the degradation process. The CuO@BC-PS system reduced BPA toxicity to a  
1382 significant extent, with no toxicity observed for CuO@BC composite (H. Qu et al., 2023).

1383         Chai et al. used a multi-metal loaded heterogeneous Fenton catalyst (M@BC) for  
1384 thiamethoxam (THX) removal, synthesized by pyrolyzing rice straw biomass rich in Fe, Cu, Mn,  
1385 and Zn. This mesoporous biochar effectively generated hydroxyl radicals ( $\cdot\text{OH}$ ) for complete THX  
1386 degradation (100%). DFT studies helped in identifying the regions with high Fukui index for  $\text{O}_2^{\cdot-}$   
1387 and  $\cdot\text{OH}$  attack (Chai et al., 2023). Seo et al. investigated seaweed biomass-derived biochar's  
1388 catalytic properties for Sulfadiazine (SDZ) removal. The adsorption process involves both physical  
1389 and chemical mechanisms. Pyrolysis enriched the biochar with N, P, and Fe, enhancing SDZ  
1390 degradation through peroxydisulfate (PDS) activation. The electron spin resonance (ESR)  
1391 confirmed reactive oxygen species (ROS) generation, including radicals ( $\text{O}_2^{\cdot-}$ ,  $\text{SO}_4^{\cdot-}$ ,  $\cdot\text{OH}$ ) and non-  
1392 radicals ( $^1\text{O}_2$ ), with non-radical mechanisms dominating, highlighting electron transfer pathways  
1393 (Seo et al., 2023). Yang et al. evaluated a modified red mud biochar catalyst (MRBC, Fe@BC) for  
1394 levofloxacin (LFX) degradation in water. MRBC synthesized via acid pretreatment and pyrolysis  
1395 at 700 °C, effectively activated peroxydisulfate (PDS), achieving 88.59% LFX removal in 30 min  
1396 with minimal Fe leaching (0.049 mg/L). The high performance of the catalyst was due to the  
1397 synergy of red mud and biomass, generating reactive oxygen species (ROS) through Fe(II) and  
1398 PDS activation. The quenching experiments and DMPOX presence in EPR confirmed that  $\text{SO}_4^{\cdot-}$   
1399 and  $\cdot\text{OH}$  were key to LFX degradation (Z. Yang et al., 2023). Tian et al. used Fe-N biochar from  
1400 waste chestnut shells, doped with iron and nitrogen (Fe-N-BC), to activate persulfate (PS) for 98%  
1401 oxytetracycline (OTC) degradation in 20 min. The process, dominated by direct electron transfer  
1402 and  $^1\text{O}_2$  generation, benefited from Fe-N structure altering electron distribution, enhancing the  
1403 efficiency and preventing iron ion leaching (Tian, Cui, et al., 2023). Oxytetracycline removal study  
1404 was also evaluated using rice husk-derived biochar (BC), hydrochar (HC), and raw husk (RH) as



1405 supports for zerovalent iron nanocomposites in PMS-activated AOPs. ZVI@BC achieved 98.3%  
1406 removal due to enhanced surface defects and ROS generation. Mechanisms were validated via  
1407 scavenger tests, DFT analysis, and HRMS intermediates identification (Kumar et al., 2025)

1408 Tian et al. studied biochar-supported zerovalent iron (ZVI@BC) for adsorbing Cd(II) and  
1409 degrading oxytetracycline (OTC). The immobilization of zerovalent iron on the biochar in  
1410 ZVI@BC improved electron transfer and its oxidation efficiency. The Cd(II) adsorption was  
1411 monolayer chemisorption, involving electrostatic interactions, ion exchange, and complex  
1412 formation, while OTC adsorption was multilayer. The ESR identified hydroxyl radicals ( $\cdot\text{OH}$ ) as  
1413 key in OTC degradation, with LC-MS revealing dealkylation, deamination, and dehydroxylation  
1414 as main degradation steps (Tian, Peng, et al., 2023). Tang et al. synthesized nitrogen-doped corn  
1415 cob biochar and immobilized it with mixed valence iron ( $\text{FeO}_x\text{@N-BC}$ ) for tetracycline  
1416 degradation via PMS activation. Nitrogen doping prevents  $\text{Fe}^0$  nanoparticle agglomeration,  
1417 enhancing electron transfer and PMS activation. The ESR analysis showed reactive oxygen  
1418 species, with singlet oxygen ( $^1\text{O}_2$ ) as dominant in tetracycline removal (Q. Tang et al., 2023). Shi  
1419 et al. studied N-doped biochar composite catalysts for Bisphenol A (BPA) degradation using  
1420 peroxymonosulfate (PMS) activation.  $\text{Fe}_3\text{C}$ /biochar, synthesized by pyrolyzing wood powder with  
1421 ferric ferrocyanide, effectively degraded 0.05 mM BPA in 30 min with 0.5 g/L catalyst. The system  
1422 generated radicals, high-valent iron-oxo, and non-radical species using both  $\text{Fe}_3\text{C}$  and N-doped  
1423 biochar. The  $\text{Fe}_3\text{C}$  activates PMS efficiently and thus minimizes Fe ion leaching and sludge  
1424 formation (Shi et al., 2023). Leichtweis et al. used  $\text{ZnFe}_2\text{O}_4$ -supported biochar from coffee grounds  
1425 for methylene blue dye degradation using  $\text{H}_2\text{O}_2$  activation. The composite achieved 100% dye  
1426 removal compared to pure  $\text{ZnFe}_2\text{O}_4$  (~37%). The high efficiency was attributed to biochar's  
1427 phenolic, hydroxyl, and carboxylic groups. The radical tests identified  $\text{h}^+$ ,  $\text{O}_2\cdot^-$ , and  $\cdot\text{OH}$  as the  
1428 reactive species involved in dye degradation (Leichtweis et al., 2023).

1429 Li et al. developed copper oxide-modified rice straw biochar ( $\text{CuO@BC}$ ) for phenacetin  
1430 (PNT) degradation using peroxydisulfate (PDS).  $\text{CuO@BC}$  showed effective PNT decomposition,  
1431 with EPR analysis identifying reactive oxygen species ( $\text{SO}_4\cdot^-$ ,  $\cdot\text{OH}$ ,  $\text{O}_2\cdot^-$ , and  $^1\text{O}_2$ ) as key in the  
1432 process. Scavenger experiments revealed  $^1\text{O}_2$  and  $\text{O}_2\cdot^-$  played a key role in PNT removal (W. Li et  
1433 al., 2020). Yang et al. synthesized zerovalent iron-supported biochar ( $\text{nZVI@BC}$ ) at 1000 °C, used  
1434 for peroxydisulfate (PDS) activation to degrade oxytetracycline (OTC). TOC results showed



1435 effective CO<sub>2</sub> conversion, while ESR and quenching identified SO<sub>4</sub><sup>-</sup>, ·OH, and <sup>1</sup>O<sub>2</sub> as key reactive  
1436 species in OTC degradation (Y. Yang et al., 2023). Yang et al. used FeS-modified rape straw (RS-  
1437 FeS) and its biochar (RSBC-FeS) for oxytetracycline (OTC) removal via H<sub>2</sub>O<sub>2</sub> activation. The  
1438 maximum removal capacities were 635.66 mg/g (RS-FeS) and 827.80 mg/g (RSBC-FeS), with  
1439 degradation rates of 70.14% and 79.35%, respectively. The process involved both radical (SO<sub>4</sub><sup>-</sup>,  
1440 ·OH, O<sub>2</sub><sup>-</sup>) and non-radical (<sup>1</sup>O<sub>2</sub>) pathways, including hydroxylation, dehydration, quinonization,  
1441 demethylation, decarbonylation, alcohol oxidation, and ring cleavage (Y. Yang et al., 2022). Jiang  
1442 et al. studied Co<sub>3</sub>O<sub>4</sub>-MnO<sub>2</sub> nanoparticles on rice straw biochar (BC) for peroxymonosulfate (PMS)  
1443 activation to remove sulfadiazine (SDZ). Nearly 100% SDZ degradation was achieved in 10 min,  
1444 primarily via singlet oxygen (<sup>1</sup>O<sub>2</sub>) and sulfate radicals (SO<sub>4</sub><sup>-</sup>) (Z.-R. Jiang et al., 2022). Sang et al.  
1445 developed a catalyst from natural pyrite (FeS<sub>2</sub>) and rice straw biochar (BC) for ciprofloxacin (CIP)  
1446 degradation, using a grinding and calcination method. The FeS<sub>2</sub>@BC system achieved 96.8% CIP  
1447 degradation in 20 min. The catalyst efficacy originates from both free radicals and adsorption  
1448 processes. The ESR and quenching experiments identified hydroxyl (·OH), superoxide (O<sub>2</sub><sup>-</sup>), and  
1449 sulfate (SO<sub>4</sub><sup>-</sup>) radicals, with ·OH being the most effective. The HCO<sub>3</sub><sup>-</sup> significantly impacted CIP  
1450 degradation, while Cl<sup>-</sup>, NO<sub>3</sub><sup>-</sup>, and SO<sub>4</sub><sup>2-</sup> had no effect. (Sang et al., 2022). Yao et al. studied the  
1451 effectiveness of bimetallic Fe and Mo immobilized on nitrogen-doped biochar (Fe-Mo@N-BC)  
1452 for degrading Orange II. They found that N-doping enhanced metal stability and dispersion. In the  
1453 PMS activation process, Fe-Mo nanoparticles transfer electrons to PMS, generating significant  
1454 ROS. The Fe/Mo bimetallic system facilitates Fe<sup>3+</sup>/Fe<sup>2+</sup> and Mo<sup>6+</sup>/Mo<sup>4+</sup> redox cycles, accelerating  
1455 PMS activation and organic degradation. The EPR and radical quenching experiments identified  
1456 SO<sub>4</sub><sup>-</sup>, ·OH, and <sup>1</sup>O<sub>2</sub> as key ROS in the process (Yao et al., 2022). Xiong et al. synthesized Co<sub>3</sub>O<sub>4</sub>  
1457 composites on biochar from rape straw for tetracycline hydrochloride (TCH) degradation via  
1458 peroxymonosulfate (PMS) activation. The Co<sub>3</sub>O<sub>4</sub>@BC catalyst achieved 90% TCH removal in 20  
1459 min, utilizing both radical (SO<sub>4</sub><sup>-</sup>, ·OH, O<sub>2</sub><sup>-</sup>) and non-radical pathways. The DFT calculations  
1460 showed an electric field at the Co<sub>3</sub>O<sub>4</sub>-BC interface, enhancing electron transfer and the Co<sup>2+</sup>/Co<sup>3+</sup>  
1461 redox cycle, improving degradation efficiency (Xiong et al., 2022). Xiao et al. developed  
1462 bimetallic iron and cerium embedded in nitrogen-enriched porous biochar (Fe-Ce@N-BC) for  
1463 metronidazole (MNZ) removal via PMS activation. MNZ degradation reached 97.5% in 60 min.  
1464 The nitrogen-enriched biochar increased surface area and porosity, enhancing PMS activation. Fe-



1465 Ce oxide nanocrystals acted as activation centres, facilitating both radical and non-radical  
1466 degradation pathways (Xiao et al., 2022).

1467 Liu et al. studied  $\text{Fe}_3\text{O}_4@\text{NCNTs-BC}$ , a nitrogen-doped magnetic carbon nanotubes-  
1468 bridged biochar catalyst, which effectively activates persulfate (PS) for sulfamethoxazole (SMX)  
1469 degradation. The quenching and ESR results showed that superoxide radicals ( $\text{O}_2^-$ ) and direct  
1470 electron transfer dominates in the process. The  $\text{Fe}_3\text{O}_4@\text{NCNTs-BC/PMS/SMX}$  system  
1471 decomposes  $\text{HSO}_5^-$  to generate active radicals, while carbon-PDS\* complexes extract electrons  
1472 from SMX (T. Liu et al., 2022). Liu et al. explained the excellent PMS activation with cobalt  
1473 nanoparticles supported biochar ( $\text{Co@BC}$ ) catalyst for levofloxacin (LVF) degradation. The  
1474  $\text{Co@BC-PMS}$  activation process showed that superoxide  $^1\text{O}_2$  non-radical, and the electron transfer  
1475 mechanisms played the dominant role in LVF degradation, as evidenced by quenching  
1476 experiments, electron paramagnetic resonance (EPR) and density functional theory (DFT)  
1477 calculations (J. Liu et al., 2022). Chen et al. investigated printing and dyeing sludge (PADS)  
1478 biochar as a peroxymonosulfate (PMS) activator for bisphenol A (BPA) removal. Prepared by  
1479 pyrolysis at 800 °C for 1.5 h, the biochar achieved 99% BPA removal in 20 min. The radical  
1480 trapping experiments indicated that the non-radical pathway, dominated by singlet oxygen ( $^1\text{O}_2$ ),  
1481 was crucial for degradation, with CO, graphite nitrogen, and pyridine nitrogen identified as active  
1482 sites for PMS activation (J. Chen et al., 2022). Fu et al. used iron-doped sludge biochar to activate  
1483 peroxymonosulfate (PMS) for degrading perfluorooctanoic acid (PFA). In the  $\text{Fe-BC/PMS}$  system,  
1484 singlet oxygen ( $^1\text{O}_2$ ) was generated, facilitated by quinone and pyridinic-N groups. The DFT  
1485 calculations indicated that PFA degradation followed a non-radical pathway with  $^1\text{O}_2$  as the main  
1486 reactive species (S. Fu et al., 2022).

1487 Huang et al. investigated the persulfate activation (PS) with magnetic rape straw biochar  
1488 catalyst for the degradation of tetracycline hydrochloride (TCH) from water. The magnetic biochar  
1489 mediated PS activation generates reactive oxygen species such as  $\text{SO}_4^-$ ,  $\cdot\text{OH}$ , and  $\text{O}_2^-$  as confirmed  
1490 with ESR analysis. The sulfate radical ( $\text{SO}_4^-$ ), and superoxide radical ( $\text{O}_2^-$ ) were observed as the  
1491 dominant reactive oxygen species for the degradation of TCH (H. Huang et al., 2021). Jiang et al.  
1492 studied a zero-valent iron and biochar composite ( $\text{ZVI@BC}$ ) activated by persulfate (PS) for  
1493 atrazine degradation. The EPR and quenching experiments revealed  $\text{SO}_4^-$  and  $\cdot\text{OH}$  as the primary  
1494 radicals responsible for degradation. The analysis of iron corrosion products and XPS suggested



1495 that ZVI@BC-PS activates PS, generating these radicals and altering iron's valence state, which  
1496 degrades atrazine. The GC-MS and LC-MS identified degradation pathways including alkyl  
1497 oxidation, dealkylation, and dechlorination-hydroxylation, etc. (Z. Jiang et al., 2020). Liu et al.  
1498 studied biochar from wheat straw immobilized with cobalt (Co@BC) for activating PMS to  
1499 degrade atrazine (ATZ). The biochar enhanced Co@BC efficiency by donating electrons to  
1500 generate superoxide radical ( $O_2^{\cdot-}$ ), converting Co(III) to Co(II). The radical scavenging and EPR  
1501 analysis revealed  $SO_4^{\cdot-}$  as the dominant reactive species in ATZ degradation (B. Liu et al., 2020).  
1502 Li et al. developed a biochar-supported copper oxide composite (CuO@BC) to activate  
1503 peroxymonosulfate (PMS) for removing Methylene Blue, Acid Orange 7, Rhodamine B, Atrazine,  
1504 and Ciprofloxacin from saline wastewater. The biochar enhanced CuO stability and catalytic  
1505 activity. The EPR analysis confirmed singlet oxygen ( $^1O_2$ ) as the primary reactive species, with  
1506 sulfate radicals ( $SO_4^{\cdot-}$ ) and hydroxyl radicals ( $\cdot OH$ ) also contribute to degradation of pollutants (Z.  
1507 Li et al., 2020).

1508 Qin et al. studied the impact of bimetallic (Fe-MgO) supported biochar on persulfate (PS)  
1509 activation for sulfamethazine (SMT) degradation. Nearly 99% SMT degradation was achieved  
1510 with Fe-MgO@BC-PS activation. The Fe-MgO@BC composite activated PS by leveraging  $Fe^{2+}$ ,  
1511 and biochar's hydroxyl and carboxyl groups, producing  $SO_4^{\cdot-}$  radicals. The SMT degradation  
1512 mechanism involved dehydrogenation, bond cracking, and unsaturated bond addition (F. Qin et  
1513 al., 2020). Zhang et al. studied ZVI@BC- $H_2O_2$  activation for sulfamethoxazole (SMX)  
1514 degradation. They achieved 99% SMX degradation in 2 h with Fe-impregnated biochar, which  
1515 enhanced  $H_2O_2$  activation. The EPR results showed  $H_2O_2$  generated hydroxyl radicals ( $\cdot OH$ )  
1516 through interactions with C-OH on biochar. Both radical and non-radical processes contributed to  
1517 SMX degradation (X. Zhang et al., 2020). Jiang et al. studied zerovalent iron (ZVI) immobilized  
1518 biochar for persulfate (PMS) activation to degrade bisphenol A (BPA). The complete BPA  
1519 removal was achieved in 5 min. The quenching and EPR experiments revealed that  $SO_4^{\cdot-}$  was the  
1520 primary radical, crucial for BPA degradation. Additionally, carbon-based materials activated  
1521 PMS's O-O bond, enabling both radical-mediated and non-radical degradation mechanisms (S.-F.  
1522 Jiang et al., 2019). Nguyen et al. explored cobalt-impregnated spent coffee ground biochar (Co-  
1523 SCG) for tetracycline (TC) removal. Co-SCG showed high adsorption and catalytic activity, with  
1524  $SO_4^{\cdot-}$  identified as the key radical in TC degradation via EPR analysis (V.-T. Nguyen et al., 2019).  
1525 Nguyen and Oh studied how biochar enhances phenol degradation in  $Fe^0$ -persulfate systems. Their



1526 research shows that  $\text{Fe}^0$  combined with biochar and persulfate significantly boosts oxidation of  
1527 contaminants. The radicals generated by electron transfer from  $\text{Fe}^0$  to persulfate involved  $\text{SO}_4^{\cdot-}$   
1528 and  $\cdot\text{OH}$  radicals to degrade phenol, with hydroxyl radicals being dominant as confirmed by EPR  
1529 and quenching experiments (T. A. Nguyen & Oh, 2019).

1530 Chen et al. developed an in-situ method for tetracycline (TC) removal using biochar (BC)  
1531 adsorption and persulfate (PS) oxidation in the  $\text{Cu}@\text{BC}$ -PS system. The process, driven by  $\text{Cu}^{+1}$ ,  
1532 effectively degrades TC across various pH levels and high COD concentrations. The XPS, EPR,  
1533 and quenching studies show  $\text{Cu}^{+1}$  on biochar activates PS, with  $\text{SO}_4^{\cdot-}$  and  $\cdot\text{OH}$  as key radicals.  $\text{Cu}^{2+}$   
1534 and TC adsorption are rate-limiting steps (J. Chen et al., 2020). Lia et al. developed magnetically  
1535 separable  $\text{MnFe}_2\text{O}_4$  nanoparticles and  $\text{MnFe}_2\text{O}_4$ /biochar composites to activate hydrogen peroxide  
1536 ( $\text{H}_2\text{O}_2$ ) for tetracycline (TC) degradation. The SEM analysis showed spherical  $\text{MnFe}_2\text{O}_4$   
1537 effectively loaded on biochar. The  $\cdot\text{OH}$  radicals confirmed by quenching and ESR experiments  
1538 drive the TC degradation. The XPS revealed Fe and Mn ions in  $\text{H}_2\text{O}_2$  activation, while biochar  
1539 prevents  $\text{MnFe}_2\text{O}_4$  aggregation and scavenges excess hydroxyl radicals (Lai et al., 2019). Mao et  
1540 al. studied biochar-supported nanoscale zero-valent iron ( $\text{nZVI}@\text{BC}$ ) with hydrogen peroxide  
1541 ( $\text{H}_2\text{O}_2$ ) for removing organic contaminants, focusing on ciprofloxacin degradation. Their research  
1542 showed hydroxyl radicals ( $\cdot\text{OH}$ ) were key in oxidation. The theoretical calculations indicated  
1543 hydrogen atom abstraction (HAA) contributed 92.3% to the second-order rate constants (k) for  
1544 ciprofloxacin oxidation (Mao et al., 2019). Fu et al. investigated graphitized hierarchical porous  
1545 biochar from corn parts and synthesized  $\text{MnFe}_2\text{O}_4/\text{BC}$  composites for organic pollutant  
1546 degradation via peroxymonosulfate (PMS) activation. The EPR and quenching studies revealed  
1547 three degradation pathways: radical-induced oxidation by  $\text{SO}_4^{\cdot-}$  and  $\cdot\text{OH}$ , non-radical oxidation by  
1548  $^1\text{O}_2$  from PMS decomposition, and electron transfer from organic compounds to PMS via  
1549 graphitization structures (H. Fu et al., 2019).

1550 Chen et al. studied  $\text{Co}_3\text{O}_4$  rice straw-derived biochar ( $\text{BC}-\text{Co}_3\text{O}_4$ ) for peroxymonosulfate  
1551 (PMS) activation, achieving high efficiency in degrading ofloxacin (OFX). The radical scavenging  
1552 and EPR analysis showed  $\text{SO}_4^{\cdot-}$  and  $\cdot\text{OH}$  radicals were involved, with enhanced degradation under  
1553 neutral to weak basic conditions and reduced effectiveness in extreme pH (L. Chen et al., 2018).  
1554 Deng and colleagues studied biochar-supported nanoscale zero-valent iron ( $\text{nZVI}@\text{BC}$ ) for  
1555 sulfamethazine removal using a  $\text{H}_2\text{O}_2$ -activated Fenton-like reaction. The  $\text{nZVI}$  decomposed  $\text{H}_2\text{O}_2$



1556 into hydroxyl radicals, while biochar adsorbed sulfamethazine, activated H<sub>2</sub>O<sub>2</sub>, and prevented  
1557 nZVI aggregation, thus enhancing sulfamethazine removal efficacy (J. Deng et al., 2018). Ma and  
1558 colleagues developed ZVI@BC via co-pyrolysis of K<sub>2</sub>FeO<sub>4</sub> and bamboo biomass, creating a  
1559 material with a high surface area. The study found that lower pH, higher temperature, and Cl<sup>-</sup> ions  
1560 improved sulfadiazine degradation, while CO<sub>3</sub><sup>2-</sup> and HPO<sub>4</sub><sup>2-</sup> impeded it. The free radicals and non-  
1561 free radicals, particularly <sup>1</sup>O<sub>2</sub>, played significant roles in the degradation process (Ma et al., 2021).

1562 Zhang and Wang synthesized nanoscale zerovalent iron on activated carbon from coconut  
1563 shells (nZVI@AC) using a pulse electrodeposition method, which was simpler and cheaper than  
1564 traditional methods. The nZVI@AC achieved 97.94% removal of methyl orange from water by  
1565 breaking its azo bonds (B. Zhang & Wang, 2019). Kaur and colleagues used *Ficus religiosa* bark  
1566 extract to immobilize zerovalent copper (ZVC@CSAC) and zerovalent iron (ZVI@CSAC) on  
1567 cotton shell activated carbon (CSAC) for activating peroxymonosulfate (PMS) to degrade  
1568 Rhodamine B (Rh B) and Crystal Violet (CV) dyes. ZVI@CSAC proved more effective than  
1569 ZVC@CSAC in dye removal. The DFT optimizations and HRMS analysis outlined the  
1570 degradation pathways. The solution toxicity tests showed intermediates were less toxic than the  
1571 original dyes (Kaur et al., 2024a). Chen et al. investigated MnO<sub>x</sub> loaded on activated carbon  
1572 (MnO<sub>x</sub>/AC) for activating PMS to degrade ciprofloxacin. MnO<sub>x</sub>/AC showed excellent  
1573 performance and reusability, with activated carbon enhancing the effectiveness of MnO<sub>x</sub>. The  
1574 Redox cycles among Mn(II, III, and IV) species produced reactive oxygen species, predominantly  
1575 singlet oxygen (63.75%). The PMS adsorption on MnO<sub>x</sub>/AC was crucial for ciprofloxacin  
1576 degradation under acidic conditions. The LC-MS analysis identified seven intermediates to  
1577 propose the degradation pathway (M. Chen et al., 2024).

1578 Li et al. developed a composite material, BAC/FeO<sub>x</sub>, combining FeO<sub>x</sub> nanoparticles with  
1579 biomass activated carbon for bisphenol A (BPA) remediation via sulfate radical-based advanced  
1580 oxidation processes (AOPs). The BAC/FeO<sub>x</sub> efficiently degrades BPA by activating  
1581 peroxydisulfate (PDS) and the process was influenced by BAC/FeO<sub>x</sub> dosage and PDS  
1582 concentration, showing versatility across pH levels and temperatures. The ESR and quenching  
1583 experiments confirmed the involvement of SO<sub>4</sub><sup>-</sup> and ·OH radicals as key species in degradation  
1584 process (X. Li et al., 2021). Yang et al. synthesized CoFe<sub>2</sub>O<sub>4</sub>@SAC nanocomposites from the  
1585 sludge activated carbon via a simple hydrothermal method. These nanocomposites effectively  
1586 degraded norfloxacin (NOR) by activating peroxymonosulfate (PMS) and showed over 90% NOR



1587 removal after five cycles. The study explored the effects of  $\text{Cl}^-$ ,  $\text{HCO}_3^-$ , and  $\text{NO}_3^-$  on the catalysis,  
1588 and identified  $\text{SO}_4^-$  and  $\cdot\text{OH}$  radicals as key to NOR degradation, with XPS revealing redox  
1589 couples  $\text{Co}^{3+}/\text{Co}^{2+}$  and  $\text{Fe}^{3+}/\text{Fe}^{2+}$  in PMS activation (Z. Yang et al., 2020). Loo et al. synthesized  
1590  $\text{Fe-TiO}_2@\text{AC}$  from oil palm empty fruit bunches via the sol-gel method. The  $\text{Fe-TiO}_2$  particles  
1591 were well-dispersed on the AC support, retaining their anatase phase. The high surface area and  
1592 porous structure of AC's improved the adsorption process, while the enhanced electrostatic  
1593 interactions and reduced recombination rates, combined with Fe doping, boosted the photocatalytic  
1594 activity.  $\text{Fe-TiO}_2@\text{AC}$  achieved 97% dye removal after 45 min of light irradiation (Loo et al.,  
1595 2021).

1596 Zhao and colleagues found that activated carbon-supported iron ( $\text{Fe}@\text{AC}$ ) is a highly  
1597 effective catalyst for amoxicillin (AMO) degradation using Persulfate (PS). The complete AMO  
1598 breakdown occurred within 10 min, with improved efficiency at higher catalyst dosages and PS  
1599 concentrations. The process followed pseudo-first-order kinetics, with an activation energy of  
1600 28.11 kJ/mol. The ESR analysis identified hydroxyl and sulfate radicals, with surface-adsorbed  
1601 hydroxyl radicals crucial for the degradation of AMO. The  $\text{Fe}@\text{AC-PS}$  system also significantly  
1602 reduced the toxicity of degraded AMO, highlighting its practical application potential (Zhao et al.,  
1603 2021). Dangwang Dikdim et al. developed a composite,  $\text{AC/g-C}_3\text{N}_4$ , for photocatalytic atrazine  
1604 degradation under visible light with PMS. Incorporating AC effectively mitigated electron-hole  
1605 recombination and enhanced the photocatalytic activity of graphitic carbon nitride. Reactive  
1606 radical trapping experiments and EPR analysis revealed that sulfate and hydroxyl radicals played  
1607 crucial roles in atrazine degradation during the reaction process (Dangwang Dikdim et al., 2019).

1608 Erdem and Erdem studied ciprofloxacin degradation in water using a persulfate activation  
1609 process with an activated carbon-supported cobalt catalyst ( $\text{Co}@\text{AC}$ ). The synthesized  $\text{Co}@\text{AC}$   
1610 activated persulfate to generate  $\text{SO}_4^-$  and  $\cdot\text{OH}$  radicals, with  $\text{SO}_4^-$  being more effective. The kinetic  
1611 analysis showed pseudo-first-order kinetics with an activation energy of 62.69 kJ/mol (Erdem &  
1612 Erdem, 2023). Nguyen et al. prepared magnetic activated carbon (MAC) using one-pot pyrolysis  
1613 of lotus seedpod waste with  $\text{ZnCl}_2$  and  $\text{FeCl}_3$  coactivation. This MAC, with a high surface area  
1614 ( $S_{\text{BET}} = 1080 \text{ m}^2/\text{g}$ ) and pore volume ( $V_{\text{total}} = 0.51 \text{ cm}^3/\text{g}$ ), effectively activated  $\text{H}_2\text{O}_2$  for removing  
1615 Acid Orange 10, outperformed MAC prepared from single activation using  $\text{FeCl}_3$  only (D. V.  
1616 Nguyen et al., 2023). Li et al. found that nZVI supported on biomass-derived porous carbon  
1617 ( $\text{nZVI}@\text{AC}$ ) removed As(III) from water more effectively and quickly than  $\text{nZVI}@\text{BC}$  and pure



1618 nZVI. The adsorption kinetics followed the pseudo-second-order model, and the Langmuir model  
1619 described isotherms. The removal involved electrostatic interaction, oxidation, and complexation  
1620 processes (X. Li et al., 2023). Wang et al. used an affordable single-atom iron catalyst (Fe@N-C)  
1621 on nitrogen-doped porous carbon to degrade sulfamethoxazole in water. The DFT calculations  
1622 identified nitrogen and oxygen coordination to iron as the active site for PMS activation. The  
1623 quenching experiments and ESR analysis showed Fe@N-C enhanced singlet oxygen ( $^1\text{O}_2$ )  
1624 production, contributing 78.77% to the degradation (C. Wang et al., 2023). Chen et al. synthesized  
1625  $\text{Co}_3\text{O}_4$ @N-doped porous carbon ( $\text{Co}_3\text{O}_4$ @NPC/rGO) using self-assembly and pyrolysis-  
1626 oxidation, with graphene oxide and bimetallic zeolite imidazolate frameworks as precursors. The  
1627 composite efficiently activates peroxymonosulfate across various pH levels, degrading  
1628 sulfamethoxazole in 5 min via both radical and non-radical pathways (Y. Chen et al., 2022).



1629 **Table 3.** Surface modified biomass nanocomposite mediated advanced oxidation processes for environmental contaminant removal

| Nanocomposite          | Oxidizing agent | Contaminant     | Optimized condition |            |             |            | % Removal | Ref.                   |
|------------------------|-----------------|-----------------|---------------------|------------|-------------|------------|-----------|------------------------|
|                        |                 |                 | pH                  | Dose (g/L) | Conc. (g/L) | Time (min) |           |                        |
| ZVC@CSAC               | PMS             | Rhodamine B     | 3                   | 0.05       | 0.01        | 60         | 87.6      | (Kaur et al., 2024a)   |
| ZVC@CSAC               | PMS             | Crystal violet  | 3                   | 0.05       | 0.01        | 10         | 99.8      |                        |
| ZVI@CSAC               | PMS             | Rhodamine B     | 3                   | 0.05       | 0.01        | 60         | 84.1      |                        |
| ZVI@CSAC               | PMS             | Crystal violet  | 3                   | 0.05       | 0.01        | 60         | 98.3      |                        |
| FeO <sub>x</sub> @N-BC | PMS             | Tetracycline    | 6.6                 | 0.2        | 0.1         | 10         | 91.8      | (Q. Tang et al., 2023) |
| Cu@BC                  | PS              | Tetracycline    | 4                   | 0.5        | 0.12        | 270        | 93.6      | (J. Chen et al., 2020) |
| Fe@BC                  | PDS             | Acid orange 7   | 6                   | 1          | 0.05        | 20         | 98        | (Z. Li et al., 2024)   |
| CuO-Biochar            | PS              | Bisphenol       | 3.84                | 0.1        | 0.01        | 40         | 93        | (H. Qu et al., 2023)   |
| Fe-N-P@BC              | PDS             | Sulfadiazine    | 6.1                 | 0.2        | 0.01        | 60         | 97.2      | (Seo et al., 2023)     |
| MRBC, Fe@BC            | PDS             | Levofloxacin    | 7                   | 1.6        | 0.01        | 30         | 88.59     | (Z. Yang et al., 2023) |
| Fe-N-BC                | PS              | Oxytetracycline | 7                   | 0.1        | 0.01        | 20         | 98        | (Tian, Cui, et al.,    |





|  |                               |                            |      |      |       |     |       |                            |
|--|-------------------------------|----------------------------|------|------|-------|-----|-------|----------------------------|
| Fe-BC  | PMS                           | Bisphenol A                | 7.26 | 0.5  | 0.002 | 30  | 100   | (Shi et al., 2023)         |
| ZnFe <sub>2</sub> O <sub>4</sub> @BC                 | H <sub>2</sub> O <sub>2</sub> | Methylene Blue             | 3    | 1    | 0.1   | 60  | 100   | (Leichtweis et al., 2023)  |
| CuO-Biochar  | PDS                           | Phenacetin                 | 4.26 | 0.3  | 0.01  | 30  | 100   | (W. Li et al., 2020)       |
| nZVI@BC  | PDS                           | Oxytetracycline            | 2    | 0.35 | 0.2   | 240 | 90.7  | (Y. Yang et al., 2023)     |
| RSBC-FeS   | H <sub>2</sub> O <sub>2</sub> | Oxytetracycline            | 2    | 0.35 | 0.2   | 240 | 79.35 | (Y. Yang et al., 2022)     |
| Co <sub>3</sub> O <sub>4</sub> -MnO <sub>2</sub> @BC | PMS                           | Sulfadiazine               | 5-9  | 0.1  | 0.025 | 10  | 100   | (Z.-R. Jiang et al., 2022) |
| FeS <sub>2</sub> @BC                                 | H <sub>2</sub> O <sub>2</sub> | Ciprofloxacin              | 3    | 1.5  | 0.03  | 20  | 96.8  | (Sang et al., 2022)        |
| Fe-Mo@N-BC   | PMS                           | Orange II                  | 4.74 | 0.1  | 0.03  | 40  | 100   | (Yao et al., 2022)         |
| Co <sub>3</sub> O <sub>4</sub> @BC                   | PMS                           | Tetracycline hydrochloride | 4.6  | 0.1  | 0.04  | 20  | 90    | (Xiong et al., 2022)       |
| Fe-Ce@N-BC   | PMS                           | Metronidazole              | 5.74 | 0.75 | 0.01  | 60  | 97.5  | (Xiao et al., 2022)        |
| Fe <sub>3</sub> O <sub>4</sub> @NCNTs-BC             | PS                            | Sulfamethoxazole           | 7    | 0.4  | 0.01  | 40  | 100   | (T. Liu et al., 2022)      |



|             |                               |                            |     |       |        |     |       |                            |
|-------------|-------------------------------|----------------------------|-----|-------|--------|-----|-------|----------------------------|
| Co@RBC      | PMS                           | Levofloxacin               | 4.5 | 0.2   | 0.01   | 15  | 100   | (J. Liu et al., 2022)      |
| Fe-BC       | PMS                           | Perfluorooctanoic acid     | 6.4 | 1     | 0.002  | 120 | 99    | (S. Fu et al., 2022)       |
| Magnetic BC | PS                            | Tetracycline hydrochloride | 5.7 | 1     | 0.02   | 120 | 99    | (H. Huang et al., 2021)    |
| ZVI-Biochar | PS                            | Atrazine                   | 4   | 0.175 | 0.025  | 30  | 73.47 | (Z. Jiang et al., 2020)    |
| Co@BC       | PMS                           | Atrazine                   | 5.3 | 0.010 | 0.002  | 10  | 100   | (B. Liu et al., 2020)      |
| CuO-Biochar | PMS                           | Methylene Blue             | 7   | 0.2   | 0.032  | 30  | 99.68 | (Z. Li et al., 2020)       |
| CuO-Biochar | PMS                           | Acid Orange 7              | 7   | 0.2   | 0.035  | 30  | 100   |                            |
| CuO-Biochar | PMS                           | Rhodamine B,               | 7   | 0.2   | 0.048  | 30  | 100   |                            |
| CuO-Biochar | PMS                           | Atrazine                   | 7   | 0.2   | 0.022  | 30  | 100   |                            |
| CuO-Biochar | PMS                           | Ciprofloxacin              | 7   | 0.2   | 0.033  | 30  | 78.27 |                            |
| Fe-Mg@BC    | PS                            | Sulfamethazine             | 3   | 2     | 0.03   | 30  | 99    | (F. Qin et al., 2020)      |
| ZVI@BC      | PMS                           | Bisphenol A                | 8.2 | 0.15  | 0.02   | 5   | 100   | (S.-F. Jiang et al., 2019) |
| ZVI@BC      | H <sub>2</sub> O <sub>2</sub> | Sulfamethoxazole           | 5   | 0.1   | 0.0025 | 120 | 99    | (X. Zhang et al., 2020)    |



|   |                               |                 |     |     |       |     |       |                           |
|---|-------------------------------|-----------------|-----|-----|-------|-----|-------|---------------------------|
| ZVI-biochar                               | PS                            | Phenol          | 7   | 0.3 | 0.094 | 330 | 97    | (T. A. Nguyen & Oh, 2019) |
| MnFe <sub>2</sub> O <sub>4</sub> -biochar | H <sub>2</sub> O <sub>2</sub> | Tetracycline    | 5.5 | 0.5 | 0.04  | 120 | 95    | (Lai et al., 2019)        |
| nZVI-Biochar                              | H <sub>2</sub> O <sub>2</sub> | Ciprofloxacin   | 3   | 0.4 | 0.1   | 60  | 70    | (Mao et al., 2019)        |
| Co <sub>3</sub> O <sub>4</sub> -Biochar   | PMS                           | Ofloxacin       | 7   | 0.2 | 0.019 | 60  | 98.9  | (L. Chen et al., 2018)    |
| nZVI-Biochar                              | H <sub>2</sub> O <sub>2</sub> | Sulfamethazine  | 3   | 1.2 | 0.01  | 720 | 74.04 | (J. Deng et al., 2018)    |
| ZVI-Biochar                               | PS                            | Sulfadiazine    | 3   | 0.2 | 0.02  | 10  | 100   | (Ma et al., 2021)         |
| MnO <sub>x</sub> @AC                      | PMS                           | Ciprofloxacin   | 2.7 | 0.5 | 0.01  | 60  | 95.3  | (M. Chen et al., 2024)    |
| FeO <sub>x</sub> -cherry stones           | PMS                           | Bisphenol A     | 7   | 0.1 | 0.02  | 5   | 100   | (X. Li et al., 2021)      |
| CoFe <sub>2</sub> O <sub>4</sub> @SAC     | PMS                           | Norfloxacin     | 5-9 | 0.1 | 0.01  | 60  | 98    | (Z. Yang et al., 2020)    |
| FeTiO <sub>2</sub> /AC                    | H <sub>2</sub> O <sub>2</sub> | Malachite Green | 4   | 1   | 0.1   | 45  | 97    | (Loo et al., 2021)        |
| ZVI@AC                                    | PS                            | Amoxicillin     | 2-9 | 1   | 0.1   | 10  | 99    | (Zhao et al., 2021)       |

|                                      |                               |                  |     |       |       |     |      |  |
|--------------------------------------|-------------------------------|------------------|-----|-------|-------|-----|------|--|
| AC/g-C <sub>3</sub> N <sub>4</sub>   | PMS                           | Atrazine         | 3   | 1     | 0.005 | 120 | 100  | (Dangwan<br>g Dikdim<br>et al.,<br>2019) |
| CO-AC                                | PS                            | Ciprofloxacin    | 7   | 0.75  | 0.017 | 120 | 100  | (Erdem &<br>Erdem,<br>2023)              |
| MAC                                  | H <sub>2</sub> O <sub>2</sub> | Acid Orange 10   | 3   | 0.2   | 0.1   | 30  | 93.9 | (D. V.<br>Nguyen et<br>al., 2023)        |
| Fe@N-C                               | PMS                           | Sulfamethoxazole | 5.6 | 0.05  | 0.01  | 40  | 95.2 | (C. Wang<br>et al.,<br>2023)             |
| Co <sub>3</sub> O <sub>4</sub> @N-AC | PMS                           | Sulfamethoxazole | 7   | 0.015 | 0.025 | 5   | 100  | (Y. Chen<br>et al.,<br>2022)             |



### 1631 **6.3. Reusability and Stability of Modified Biomass Materials**

1632 In practical environmental remediation, the reusability and stability of biomass-derived materials  
1633 are just as critical as their initial adsorption or catalytic efficiency. Materials that quickly lose  
1634 activity or suffer structural degradation during repeated use have limited applicability in real-world  
1635 scenarios. Thus, systematic evaluation and enhancement of their long-term durability are  
1636 indispensable for advancing their practical deployment.

#### 1638 **6.3.1. Regeneration and cycling performance**

1639 Many modified biomass adsorbents exhibit significant regeneration potential through simple  
1640 desorption techniques such as washing with dilute acids, bases, or organic solvents. For instance,  
1641 alkali-activated rice husk biochar has retained more than 80% of its dye removal efficiency over  
1642 five adsorption–desorption cycles (Kaur et al., 2024b), while iron-immobilized biochars showed  
1643 consistent Cr(VI) removal performance across multiple cycles (Zhou et al., 2023). The  
1644 regeneration capacity largely depends on the stability of functional groups introduced during  
1645 surface modification and the resilience of the porous network to repeated sorption–desorption  
1646 stresses.

#### 1648 **6.3.2. Thermal and structural stability**

1649 The thermal stability of biomass-derived adsorbents is strongly influenced by the activation or  
1650 nanostructuring technique employed. Pyrolysis-derived biochars demonstrate higher carbonization  
1651 and improved resistance to thermal degradation, while hydrothermal carbonization often results in  
1652 hydrochars with moderate stability but abundant oxygenated groups. Further enhancement is  
1653 achieved by immobilization of metal or metal oxide nanoparticles (e.g., Fe<sub>3</sub>O<sub>4</sub>, TiO<sub>2</sub>, ZnO), which  
1654 not only provide catalytic activity but also prevent collapse of pore structures at elevated  
1655 temperatures (Kumar et al., 2022). Thermogravimetric analyses have confirmed that chemically  
1656 activated carbons and nanocomposites display improved decomposition resistance compared to  
1657 raw biomass (Kaur et al., 2024b).

#### 1659 **6.3.3. Chemical stability under operational conditions**

1660 In real wastewater systems, pH fluctuations, high ionic strengths, and competing contaminants  
1661 may compromise material performance. Acid-modified biochars, for example, may leach



1662 functional groups under highly alkaline conditions, whereas nanoparticle-loaded composites risk  
1663 metal leaching into the environment (Kumar et al., 2025). Stabilization strategies such as covalent  
1664 cross-linking, polymer coating, or strong electrostatic immobilization of nanoparticles can  
1665 significantly improve long-term chemical resistance (H. Han et al., 2019). However,  
1666 comprehensive studies under variable real-world conditions remain limited.

#### 1667 **6.3.4. Strategies for enhancing reusability and durability**

1668 Surface functionalization with stable moieties (e.g., amine, sulfonic acid groups), hybridization  
1669 with inorganic supports (clays, silica, zeolites), and carbonization at optimized conditions have  
1670 proven effective in improving reusability (Y. Chen et al., 2022). Additionally, coupling adsorption  
1671 with catalytic degradation (as in biochar–metal oxide nanocomposites) reduces fouling of active  
1672 sites, thereby extending material lifetime. Developing multifunctional composites that combine  
1673 adsorption, photocatalysis, and redox reactivity represents a promising path toward enhanced  
1674 stability (H. Han et al., 2019).

### 1676 **6.4. Economic Viability and Scalability of Biomass Modification Techniques**

1677 Although biomass itself is an abundant and low-cost feedstock, the economic feasibility of its  
1678 modified derivatives depends heavily on the activation and nanostructuring techniques employed.  
1679 While many studies emphasize material performance, fewer critically assess the cost and  
1680 scalability of these treatments, which are crucial for large-scale deployment.

#### 1681 **6.4.1. Cost implications of modification techniques**

1682 Chemical activation methods (e.g., acid/alkali treatments, oxidative agents) can substantially  
1683 improve porosity and functional group density, but they also incur significant costs from reagent  
1684 consumption, high-temperature processing, and post-treatment washing to remove residues.  
1685 Additionally, chemical processes generate secondary waste streams requiring careful disposal,  
1686 which further adds to operational costs (Kumar et al., 2025). In contrast, physical methods such as  
1687 pyrolysis, hydrothermal carbonization, or microwave heating are generally more cost-efficient and  
1688 scalable, though they may yield materials with lower surface functionalization unless combined  
1689 with post-modification steps (Kaur et al., 2024b).

#### 1690 **6.4.2. Scalability considerations**

1691 From a scalability perspective, physical methods hold greater promise for industrial adoption due  
1692 to their simpler setups, compatibility with bulk biomass feedstocks, and potential to integrate with



1693 existing waste-to-energy infrastructure. Hydrothermal carbonization, for instance, eliminates the  
1694 need for biomass drying and operates under moderate conditions, making it suitable for  
1695 continuous-flow systems (Thamarai et al., 2024b). On the other hand, nanostructuring with  
1696 metal/metal oxide nanoparticles, although effective for enhancing catalytic and adsorption  
1697 performance, raises concerns regarding raw material costs, potential leaching, and complex  
1698 synthesis protocols that may hinder scale-up (Kumar et al., 2025).

#### 1699 **6.4.3. Strategies for improving economic feasibility**

1700 Hybrid approaches that combine low-cost physical methods with selective chemical or biological  
1701 modifications may offer a more balanced trade-off between performance and cost. Valorization of  
1702 process by-products (e.g., bio-oil, syngas from pyrolysis) could further offset treatment costs  
1703 ((Amenaghawon et al., 2021). Moreover, implementing circular economy principles such as  
1704 reusing spent adsorbents in energy recovery or soil amendment could enhance the overall  
1705 economic and environmental sustainability.

#### 1707 **6.5. Real-World and Pilot-Scale Applications of Surface-Modified and Nanostructured 1708 Biomass in Environmental Remediation**

1709 While laboratory-scale investigations dominate the literature, several pilot-scale and field  
1710 applications highlight the feasibility of biomass-derived materials in real environmental systems.  
1711 For example, granular walnut shell biochar layered into sand-based constructed wetlands  
1712 effectively neutralized acidity and removed multiple heavy metals from simulated mining-  
1713 impacted water, while enhancing plant growth and regulating microbial communities (Chen et al.,  
1714 2021). In another study, alkali-activated rice husk biochar was tested in a textile wastewater  
1715 treatment plant and demonstrated >80% dye removal efficiency, with stable regeneration  
1716 performance over multiple cycles (Katheresan et al., 2018). Similarly, hydrothermally carbonized  
1717 sewage sludge was applied at field scale to immobilize heavy metals in contaminated soils thus  
1718 reducing metal leaching (Wang et al., 2019). Further, a pilot-scale biochar-amended sand filtration  
1719 system was evaluated for drinking water treatment and showed significant removal of natural and  
1720 heavy metals (Eniola et al., 2023).

1721 These case studies demonstrate that surface-modified biomass can be engineered into scalable  
1722 remediation systems such as packed-bed reactors, constructed wetlands, and filtration units.



1723 Nevertheless, challenges remain in ensuring long-term stability, regeneration, and economic  
1724 viability.

1725

## 1726 **7. Future perspectives:**

1727 In the future, the modified surface of biomass, its carbon-rich derivatives, and metal  
1728 nanocomposites hold significant potential for enhancing environmental remediation applications,  
1729 particularly through persulfate (PMS) activation. Advanced material synthesis techniques will be  
1730 crucial for fine-tuning catalytic efficiency and durability, as well as for deepening mechanistic  
1731 understanding of pollutant degradation pathways. Such mechanistic insights can guide the rational  
1732 development of surface-modified materials tailored for specific environmental challenges. Equally  
1733 important will be the scaling-up of production methods and their integration into practical  
1734 remediation strategies, which requires innovation in reactor design, cost-effectiveness analysis,  
1735 and techno-economic feasibility studies. The exploration of multifunctional materials and  
1736 prioritization of sustainability in both synthesis and application will further improve adaptability  
1737 and long-term effectiveness across diverse environmental matrices.

1738 Looking forward, artificial intelligence (AI) and machine learning (ML) are expected to play  
1739 transformative roles in accelerating material design and process optimization. AI-guided  
1740 computational approaches can predict pollutant–surface interactions, identify optimal  
1741 modification strategies, and reduce reliance on trial-and-error experimentation. Similarly, ML-  
1742 driven process control can optimize operating conditions in pilot and full-scale systems, enabling  
1743 real-time adjustments that enhance efficiency and lower costs.

1744 Another emerging direction is the integration of biomass valorization into circular economy  
1745 frameworks. Agricultural residues, forestry by-products, and municipal wastes can be transformed  
1746 into functional remediation materials, turning waste streams into value-added resources. Closed-  
1747 loop strategies, where spent adsorbents are regenerated, reused, or repurposed into new products,  
1748 will be critical for sustainable deployment. Combining advanced characterization techniques with  
1749 AI/ML will also enable deeper insights into adsorption and catalytic mechanisms, thereby guiding  
1750 the rational design of next-generation nanostructured biomass composites. Collectively, these  
1751 future directions suggest a paradigm shift from conventional modification approaches toward  
1752 digitally optimized, multifunctional, and circular bio-based remediation technologies, which hold  
1753 promise for addressing global pollution challenges in a sustainable and scalable manner.



1754

## 1755 **8. Conclusion**

1756 The tailored surface modified biomass and its carbon-rich derivatives offer tremendous  
1757 potential for enhanced environmental remediation applications. The innovative surface  
1758 modification techniques, such as chemical functionalization and nanoparticle deposition on  
1759 biomass materials can be engineered to exhibit the superior adsorption and degradation capacities,  
1760 selectivity, and stability for various environmental remediations. These modified biomaterials not  
1761 only demonstrate the remarkable efficiency for the removal of contaminants, but also present  
1762 several advantages, including cost-effectiveness, biodegradability, and sustainability. The  
1763 conversion of biomass into the carbon-rich derivatives, such as biochar and activated carbon, not  
1764 only mitigates waste, but also creates the valuable materials with exceptional adsorption properties  
1765 and pore structures. These carbonaceous materials serve as effective sorbents for a wide range of  
1766 contaminants, including inorganic and organic materials. Further immobilization of metal  
1767 nanocomposites presents a powerful approach for enhanced environmental remediation  
1768 applications, particularly in the activation of persulfate (PMS) for pollutant degradation. The  
1769 synergistic interactions between biomass-derived carbon matrices and metal nanoparticles exhibit  
1770 the enhanced catalytic activity, stability, and selectivity, thereby offering promising solutions for  
1771 addressing complex environmental challenges. The incorporation of metal nanoparticles onto  
1772 biomass-derived carbon substrates not only enhances the surface area and porosity, but also  
1773 facilitates electron transfer and reactive species generation, leading to efficient activation of PMS  
1774 and subsequent degradation of various contaminants. The surface modification of biomass allows  
1775 for precise control over surface chemistry and functional groups, further optimizing the  
1776 performance of these composites for specific contaminant removal.

1777

## 1778 **List of abbreviations**

1779

1780 MW, microwave assisted; HTC, hydrothermal carbonization; nZVI, nanoscale zerovalent iron;  
1781 BET, Brunauer-Emmett-Teller, TEM, transmission electron microscopy; SEM, scanning electron  
1782 microscopy; XRD, X-ray diffraction; TGA, thermogravimetric analysis; DTA, differential thermal  
1783 analysis; EDS, energy dispersive X-ray spectroscopy; FTIR, fourier-transform infrared  
1784 spectroscopy; XPS, X-ray photoelectron spectroscopy; EPR, electron paramagnetic resonance,  
1785 AC, activated carbon; BC, biochar; N-BC, nitrogen-doped biochar; PS, persulfate; PMS,  
1786 peroxymonosulfate; PDS, peroxydisulfate; PI, periodate; DFT, density functional theory; GC-MS,  
1787 gas chromatography-mass spectrometry; LC-MS, liquid chromatography-mass spectrometry;  
1788 HRMS, high-resolution mass spectrometry.



1789

**1790 Declarations****1791 Author contribution statement**

1792 All authors have made significant contributions to the formulation and composition of this review article.

1793 Conceptualization: Sandeep Kumar, Parminder Kaur, Chou-Yi Hsu, Mohammed Ahmed Mustafa, Jyoti

1794 Rani, Jasmeen Kaur, Sandeep Kaushal; Methodology: Sandeep Kumar, Parminder Kaur, Chou-Yi Hsu,

1795 Mohammed Ahmed Mustafa, Sandeep Kaushal; Writing - Original Draft: Sandeep Kumar, Parminder Kaur,

1796 Chou-Yi Hsu, Mohammed Ahmed Mustafa, Jyoti Rani, Jasmeen Kaur, Sandeep Kaushal; Visualization:

1797 Sandeep Kumar, Parminder Kaur, Chou-Yi Hsu, Mohammed Ahmed Mustafa, Sandeep Kaushal;;

1798 Supervision: Sandeep Kumar, Sandeep Kaushal.

1799

**1800 Funding statement**

1801 This research did not receive any specific grant from funding agencies in the public, commercial,

1802 or not-for-profit sectors.

**1803 Declaration of interest statement**

1804 The authors declare no conflict of interest.

**1805 Additional information**

1806 No additional information is available for this paper.

**1807 Acknowledgements**

1808 The authors of this manuscript are thankful to Akal University for providing research support and

1809 facilities.

**1810 Data availability**

1811 All data is available and will be provided on request.



1812 **Reference**

1813

1814 Abatal, M., Anastopoulos, I., Giannakoudakis, D. A., & Olguin, M. T. (2020). Carbonaceous material  
1815 obtained from bark biomass as adsorbent of phenolic compounds from aqueous solutions. *Journal*  
1816 *of Environmental Chemical Engineering*, 8(3), 103784. <https://doi.org/10.1016/j.jece.2020.103784>

1817 Abegunde, S. M., Idowu, K. S., Adejuwon, O. M., & Adeyemi-Adejolu, T. (2020). A review on the  
1818 influence of chemical modification on the performance of adsorbents. *Resources, Environment and*  
1819 *Sustainability*, 1, 100001. <https://doi.org/10.1016/j.resenv.2020.100001>

1820 Abo El Naga, A. O., El Saied, M., Shaban, S. A., & El Kady, F. Y. (2019). Fast removal of diclofenac  
1821 sodium from aqueous solution using sugar cane bagasse-derived activated carbon. *Journal of*  
1822 *Molecular Liquids*, 285, 9–19. <https://doi.org/10.1016/j.molliq.2019.04.062>

1823 Akhtar, K., Ali, F., Sohni, S., Kamal, T., Asiri, A. M., Bakhsh, E. M., & Khan, S. B. (2020). Lignocellulosic  
1824 biomass supported metal nanoparticles for the catalytic reduction of organic pollutants.  
1825 *Environmental Science and Pollution Research*, 27(1), 823–836. [https://doi.org/10.1007/s11356-](https://doi.org/10.1007/s11356-019-06908-y)  
1826 [019-06908-y](https://doi.org/10.1007/s11356-019-06908-y)

1827 Akram, M., Khan, B., Imran, M., Ahmad, I., Ajaz, H., Tahir, M., Rabbani, F., Kaleem, I., Nadeem Akhtar,  
1828 M., Ahmad, N., & Samad Shah, N. (2019). Biosorption of lead by cotton shells powder:  
1829 Characterization and equilibrium modeling study. *International Journal of Phytoremediation*,  
1830 *21*(2), 138–144. <https://doi.org/10.1080/15226514.2018.1488810>

1831 Ali Redha, A. (2020). Removal of heavy metals from aqueous media by biosorption. *Arab Journal of Basic*  
1832 *and Applied Sciences*, 27(1), 183–193. <https://doi.org/10.1080/25765299.2020.1756177>

1833 Al-Mokhalelati, K., Al-Bakri, I., & Al Shibeh Al Wattar, N. (2021). Adsorption of methylene blue onto  
1834 sugarcane bagasse-based adsorbent materials. *Journal of Physical Organic Chemistry*, 34(7),  
1835 e4193. <https://doi.org/10.1002/poc.4193>

1836 Al-sareji, O. J., Meiczinger, M., Al-Juboori, R. A., Grmasha, R. A., Andredaki, M., Somogyi, V., Idowu,  
1837 I. A., Stenger-Kovács, C., Jakab, M., Lengyel, E., & Hashim, K. S. (2023). Efficient removal of



- 1838 pharmaceutical contaminants from water and wastewater using immobilized laccase on activated  
1839 carbon derived from pomegranate peels. *Scientific Reports*, 13(1), 11933.  
1840 <https://doi.org/10.1038/s41598-023-38821-3>
- 1841 Altıntig, E., Altundag, H., Tuzen, M., & Sari, A. (2017). Effective removal of methylene blue from aqueous  
1842 solutions using magnetic loaded activated carbon as novel adsorbent. *Chemical Engineering*  
1843 *Research and Design*, 122, 151–163. <https://doi.org/10.1016/j.cherd.2017.03.035>
- 1844 Amenaghawon, A. N., Anyalewechi, C. L., Okieimen, C. O., & Kusuma, H. S. (2021). Biomass pyrolysis  
1845 technologies for value-added products: A state-of-the-art review. *Environment, Development and*  
1846 *Sustainability*, 23(10), 14324–14378. <https://doi.org/10.1007/s10668-021-01276-5>
- 1847 Amjith, L., & Bavanish, B. (2022). A review on biomass and wind as renewable energy for sustainable  
1848 environment. *Chemosphere*, 293, 133579. <https://doi.org/10.1016/j.chemosphere.2022.133579>
- 1849 Antar, M., Lyu, D., Nazari, M., Shah, A., Zhou, X., & Smith, D. L. (2021). Biomass for a sustainable  
1850 bioeconomy: An overview of world biomass production and utilization. *Renewable and*  
1851 *Sustainable Energy Reviews*, 139, 110691. <https://doi.org/10.1016/j.rser.2020.110691>
- 1852 Ao, W., Fu, J., Mao, X., Kang, Q., Ran, C., Liu, Y., Zhang, H., Gao, Z., Li, J., Liu, G., & Dai, J. (2018).  
1853 Microwave assisted preparation of activated carbon from biomass: A review. *Renewable and*  
1854 *Sustainable Energy Reviews*, 92, 958–979. <https://doi.org/10.1016/j.rser.2018.04.051>
- 1855 Astuti, W., Sulistyaningsih, T., Prastiyanto, D., Rusiyanto, Lanjar, Riayanti, F. I., Astuti, A. W., Wibowo,  
1856 W. T., Handayani, A. D., & Wulandari, D. A. (2023). Influence of lignocellulosic composition in  
1857 biomass waste on the microstructure and dye adsorption characteristics of microwave-assisted  
1858 ZnCl<sub>2</sub> activated carbon. *Biomass Conversion and Biorefinery*. [https://doi.org/10.1007/s13399-023-](https://doi.org/10.1007/s13399-023-04281-y)  
1859 [04281-y](https://doi.org/10.1007/s13399-023-04281-y)
- 1860 Baek, J., Lee, H.-M., An, K.-H., & Kim, B.-J. (2019). Preparation and characterization of highly  
1861 mesoporous activated short carbon fibers from kenaf precursors. *Carbon Letters*, 29(4), 393–399.  
1862 <https://doi.org/10.1007/s42823-019-00042-y>



- 1863 Baloo, L., Isa, M. H., Sapari, N. B., Jagaba, A. H., Wei, L. J., Yavari, S., Razali, R., & Vasu, R. (2021).  
1864 Adsorptive removal of methylene blue and acid orange 10 dyes from aqueous solutions using oil  
1865 palm wastes-derived activated carbons. *Alexandria Engineering Journal*, 60(6), 5611–5629.  
1866 <https://doi.org/10.1016/j.aej.2021.04.044>
- 1867 Banerjee, M., Bar, N., Basu, R. K., & Das, S. K. (2018). Removal of Cr(VI) from Its Aqueous Solution  
1868 Using Green Adsorbent Pistachio Shell: A Fixed Bed Column Study and GA-ANN Modeling.  
1869 *Water Conservation Science and Engineering*, 3(1), 19–31. [https://doi.org/10.1007/s41101-017-](https://doi.org/10.1007/s41101-017-0039-x)  
1870 [0039-x](https://doi.org/10.1007/s41101-017-0039-x)
- 1871 Bedia, J., Peñas-Garzón, M., Gómez-Avilés, A., Rodríguez, J., & Belver, C. (2018). A Review on the  
1872 Synthesis and Characterization of Biomass-Derived Carbons for Adsorption of Emerging  
1873 Contaminants from Water. *C*, 4(4), 63. <https://doi.org/10.3390/c4040063>
- 1874 Bhuyan, A., & Ahmaruzzaman, Md. (2023). Recent advances in new generation nanocomposite materials  
1875 for adsorption of pharmaceuticals from aqueous environment. *Environmental Science and*  
1876 *Pollution Research*, 30(14), 39377–39417. <https://doi.org/10.1007/s11356-023-25707-0>
- 1877 Bouzidi, M., Sellaoui, L., Mohamed, M., S. P. Franco, D., Erto, A., & Badawi, M. (2023). A comprehensive  
1878 study on paracetamol and ibuprofen adsorption onto biomass-derived activated carbon through  
1879 experimental and theoretical assessments. *Journal of Molecular Liquids*, 376, 121457.  
1880 <https://doi.org/10.1016/j.molliq.2023.121457>
- 1881 Cai, S., Zhang, Q., Wang, Z., Hua, S., Ding, D., Cai, T., & Zhang, R. (2021). Pyrrolic N-rich biochar  
1882 without exogenous nitrogen doping as a functional material for bisphenol A removal: Performance  
1883 and mechanism. *Applied Catalysis B: Environmental*, 291, 120093.  
1884 <https://doi.org/10.1016/j.apcatb.2021.120093>
- 1885 Cao, Y., Xiao, W., Shen, G., Ji, G., Zhang, Y., Gao, C., & Han, L. (2019). Carbonization and ball milling  
1886 on the enhancement of Pb(II) adsorption by wheat straw: Competitive effects of ion exchange and  
1887 precipitation. *Bioresource Technology*, 273, 70–76. <https://doi.org/10.1016/j.biortech.2018.10.065>



- 1888 Chai, Y., Bai, M., Chen, A., Xu, X., Tong, Z., Yuan, J., Peng, L., Shao, J., Xiong, J., & Peng, C. (2023).  
1889 Upcycling contaminated biomass into metal-supported heterogeneous catalyst for electro-Fenton  
1890 degradation of thiamethoxam: Preparation, mechanisms, and implications. *Chemical Engineering*  
1891 *Journal*, 453, 139814. <https://doi.org/10.1016/j.cej.2022.139814>
- 1892 Chavali, M. S., & Nikolova, M. P. (2019). Metal oxide nanoparticles and their applications in  
1893 nanotechnology. *SN Applied Sciences*, 1(6), 607. <https://doi.org/10.1007/s42452-019-0592-3>
- 1894 Chen, J., Deng, S., Jia, W., Li, X., Chang, J. (2021). Removal of multiple heavy metals from mining-  
1895 impacted water by biochar-filled constructed wetlands: Adsorption and biotic removal routes.  
1896 *Bioresource Technology*, 331, 125061. <https://doi.org/10.1016/j.biortech.2021.125061>
- 1897 Chen, D., Xie, S., Chen, C., Quan, H., Hua, L., Luo, X., & Guo, L. (2017). Activated biochar derived from  
1898 pomelo peel as a high-capacity sorbent for removal of carbamazepine from aqueous solution. *RSC*  
1899 *Advances*, 7(87), 54969–54979. <https://doi.org/10.1039/C7RA10805B>
- 1900 Chen, J., Bai, X., Yuan, Y., Zhang, Y., & Sun, J. (2022). Printing and dyeing sludge derived biochar for  
1901 activation of peroxymonosulfate to remove aqueous organic pollutants: Activation mechanisms  
1902 and environmental safety assessment. *Chemical Engineering Journal*, 446, 136942.  
1903 <https://doi.org/10.1016/j.cej.2022.136942>
- 1904 Chen, J., Li, H., Li, J., Chen, F., Lan, J., & Hou, H. (2021). Efficient removal of tetracycline from water by  
1905 tannic acid-modified rice straw-derived biochar: Kinetics and mechanisms. *Journal of Molecular*  
1906 *Liquids*, 340, 117237. <https://doi.org/10.1016/j.molliq.2021.117237>
- 1907 Chen, J., Yu, X., Li, C., Tang, X., & Sun, Y. (2020). Removal of tetracycline via the synergistic effect of  
1908 biochar adsorption and enhanced activation of persulfate. *Chemical Engineering Journal*, 382,  
1909 122916. <https://doi.org/10.1016/j.cej.2019.122916>
- 1910 Chen, L., Yang, S., Zuo, X., Huang, Y., Cai, T., & Ding, D. (2018). Biochar modification significantly  
1911 promotes the activity of Co<sub>3</sub>O<sub>4</sub> towards heterogeneous activation of peroxymonosulfate. *Chemical*  
1912 *Engineering Journal*, 354, 856–865. <https://doi.org/10.1016/j.cej.2018.08.098>
- 1913 Chen, M., Yang, T., Zhao, L., Shi, X., Li, R., Ma, L., Huang, Y., Wang, Y., & Lee, S. (2024). Manganese  
1914 oxide on activated carbon with peroxymonosulfate activation for enhanced ciprofloxacin



- 1915 degradation: Activation mechanism and degradation pathway. *Applied Surface Science*, 645,  
1916 158835. <https://doi.org/10.1016/j.apsusc.2023.158835>
- 1917 Chen, Y., Bai, X., Ji, Y., & Shen, T. (2022). Reduced graphene oxide-supported hollow Co<sub>3</sub>O<sub>4</sub>@N-doped  
1918 porous carbon as peroxymonosulfate activator for sulfamethoxazole degradation. *Chemical  
1919 Engineering Journal*, 430, 132951. <https://doi.org/10.1016/j.cej.2021.132951>
- 1920 Chen, Y., Wang, Z., Lin, S., Qin, Y., & Huang, X. (2023). A review on biomass thermal-oxidative  
1921 decomposition data and machine learning prediction of thermal analysis. *Cleaner Materials*, 9,  
1922 100206. <https://doi.org/10.1016/j.clema.2023.100206>
- 1923 Cui, C., Yang, M., Zhai, J., Bai, W., Dai, L., Liu, L., Jiang, S., Wang, W., Ren, E., Cheng, C., & Guo, R.  
1924 (2022). Bamboo cellulose-derived activated carbon aerogel with controllable mesoporous structure  
1925 as an effective adsorbent for tetracycline hydrochloride. *Environmental Science and Pollution  
1926 Research*, 30(5), 12558–12570. <https://doi.org/10.1007/s11356-022-22926-9>
- 1927 Dai, J., Meng, X., Zhang, Y., & Huang, Y. (2020). Effects of modification and magnetization of rice straw  
1928 derived biochar on adsorption of tetracycline from water. *Bioresource Technology*, 311, 123455.  
1929 <https://doi.org/10.1016/j.biortech.2020.123455>
- 1930 Dai, J., Wang, Z., Chen, K., Ding, D., Yang, S., & Cai, T. (2023). Applying a novel advanced oxidation  
1931 process of biochar activated periodate for the efficient degradation of bisphenol A: Two nonradical  
1932 pathways. *Chemical Engineering Journal*, 453, 139889. <https://doi.org/10.1016/j.cej.2022.139889>
- 1933 Dangwang Dikdim, J. M., Gong, Y., Noumi, G. B., Sieliechi, J. M., Zhao, X., Ma, N., Yang, M., &  
1934 Tchatchueng, J. B. (2019). Peroxymonosulfate improved photocatalytic degradation of atrazine by  
1935 activated carbon/graphitic carbon nitride composite under visible light irradiation. *Chemosphere*,  
1936 217, 833–842. <https://doi.org/10.1016/j.chemosphere.2018.10.177>
- 1937 Darweesh, T. M., & Ahmed, M. J. (2017). Batch and fixed bed adsorption of levofloxacin on granular  
1938 activated carbon from date ( *Phoenix dactylifera* L.) stones by KOH chemical activation.  
1939 *Environmental Toxicology and Pharmacology*, 50, 159–166.  
1940 <https://doi.org/10.1016/j.etap.2017.02.005>



- 1941 Demir, M., Saraswat, S. K., & Gupta, R. B. (2017). Hierarchical nitrogen-doped porous carbon derived  
1942 from lecithin for high-performance supercapacitors. *RSC Advances*, 7(67), 42430–42442.  
1943 <https://doi.org/10.1039/C7RA07984B>
- 1944 Demiral, İ., Samdan, C., & Demiral, H. (2021). Enrichment of the surface functional groups of activated  
1945 carbon by modification method. *Surfaces and Interfaces*, 22, 100873.  
1946 <https://doi.org/10.1016/j.surfin.2020.100873>
- 1947 Deng, H., Lu, J., Li, G., Zhang, G., & Wang, X. (2011). Adsorption of methylene blue on adsorbent  
1948 materials produced from cotton stalk. *Chemical Engineering Journal*, 172(1), 326–334.  
1949 <https://doi.org/10.1016/j.cej.2011.06.013>
- 1950 Deng, J., Dong, H., Zhang, C., Jiang, Z., Cheng, Y., Hou, K., Zhang, L., & Fan, C. (2018). Nanoscale zero-  
1951 valent iron/biochar composite as an activator for Fenton-like removal of sulfamethazine.  
1952 *Separation and Purification Technology*, 202, 130–137.  
1953 <https://doi.org/10.1016/j.seppur.2018.03.048>
- 1954 Dey, A. K., & Ahmaruzzaman, Md. (2023). Recent Advances in Nano-metal Oxide-Biochar Composites  
1955 for Efficient Removal of Environmental Contaminants. *Reviews of Environmental Contamination  
1956 and Toxicology*, 261(1), 6. <https://doi.org/10.1007/s44169-023-00030-4>
- 1957 Dias, S. L. P., Neto, C. L., Ferreira, V. G., Vagheti, J. C. P., Machado, G. B., & Bianchi, O. (2024).  
1958 Exploring the thermal degradation of pine nut shells: A study on biochar production and its efficacy  
1959 in cationic dye adsorption from water. *Biomass Conversion and Biorefinery*.  
1960 <https://doi.org/10.1007/s13399-024-05470-z>
- 1961 Ding, D., Yang, S., Qian, X., Chen, L., & Cai, T. (2020). Nitrogen-doping positively whilst sulfur-doping  
1962 negatively affect the catalytic activity of biochar for the degradation of organic contaminant.  
1963 *Applied Catalysis B: Environmental*, 263, 118348. <https://doi.org/10.1016/j.apcatb.2019.118348>
- 1964 Do Nascimento, R. K., Damasceno, B. S., De Melo, A. N., De Farias, P. H. M., Cavalcanti, J. V. F. L.,  
1965 Sales, D. C. S., Falcão, E. H. L., & De Araújo, A. C. V. (2023). Hybrid nanomaterial from



- 1966 pyrolyzed biomass and Fe<sub>3</sub>O<sub>4</sub> magnetic nanoparticles for the adsorption of textile dyes. *Cellulose*,  
1967 30(4), 2483–2501. <https://doi.org/10.1007/s10570-022-04978-9>
- 1968 Dong, S., Shen, X., Guo, Q., Cheng, H., Giannakis, S., He, Z., Wang, L., Wang, D., Song, S., & Ma, J.  
1969 (2023). Valorization of soybean plant wastes in preparation of N-doped biochar for catalytic  
1970 ozonation of organic contaminants: Atrazine degradation performance and mechanistic  
1971 considerations. *Chemical Engineering Journal*, 472, 145153.  
1972 <https://doi.org/10.1016/j.cej.2023.145153>
- 1973 El Mouchtari, E. M., Daou, C., Rafqah, S., Najjar, F., Anane, H., Piram, A., Hamade, A., Briche, S., &  
1974 Wong-Wah-Chung, P. (2020). TiO<sub>2</sub> and activated carbon of Argania Spinosa tree nutshells  
1975 composites for the adsorption photocatalysis removal of pharmaceuticals from aqueous solution.  
1976 *Journal of Photochemistry and Photobiology A: Chemistry*, 388, 112183.  
1977 <https://doi.org/10.1016/j.jphotochem.2019.112183>
- 1978 Eldhose, M., Roy, R., George, C., & Joseph, A. (2023). Physical Modification of Biomass. In S. Thomas,  
1979 M. Hosur, D. Pasquini, & C. Jose Chirayil (Eds.), *Handbook of Biomass* (pp. 1–20). Springer  
1980 Nature Singapore. [https://doi.org/10.1007/978-981-19-6772-6\\_17-1](https://doi.org/10.1007/978-981-19-6772-6_17-1)
- 1981 Elewa, A. M., Amer, A. A., Attallah, M. F., Gad, H. A., Al-Ahmed, Z. A. M., & Ahmed, I. A. (2023).  
1982 Chemically Activated Carbon Based on Biomass for Adsorption of Fe(III) and Mn(II) Ions from  
1983 Aqueous Solution. *Materials*, 16(3), 1251. <https://doi.org/10.3390/ma16031251>
- 1984 Eniola, J.O., & Sizirici, B. (2023). Investigation of biochar- modified biosand filter performance for  
1985 groundwater treatment for drinking water purposes: A laboratory and pilot scale study. *Journal of*  
1986 *Water Process Engineering* 53, 103914. <https://doi.org/10.1016/j.jwpe.2023.103914>
- 1987 Erdem, H., & Erdem, M. (2023). Ciprofloxacin Degradation with Persulfate Activated with the Synergistic  
1988 Effect of the Activated Carbon and Cobalt Dual Catalyst. *Arabian Journal for Science and*  
1989 *Engineering*, 48(7), 8401–8415. <https://doi.org/10.1007/s13369-022-06907-1>
- 1990 Ertaş, M., Acemioğlu, B., Alma, M. H., & Usta, M. (2010). Removal of methylene blue from aqueous  
1991 solution using cotton stalk, cotton waste and cotton dust. *Journal of Hazardous Materials*, 183(1–  
1992 3), 421–427. <https://doi.org/10.1016/j.jhazmat.2010.07.041>



- 1993 Ezeonuegbu, B. A., Machido, D. A., Whong, C. M. Z., Japhet, W. S., Alexiou, A., Elazab, S. T., Qusty, N.,  
1994 Yaro, C. A., & Batiha, G. E.-S. (2021). Agricultural waste of sugarcane bagasse as efficient  
1995 adsorbent for lead and nickel removal from untreated wastewater: Biosorption, equilibrium  
1996 isotherms, kinetics and desorption studies. *Biotechnology Reports*, 30, e00614.  
1997 <https://doi.org/10.1016/j.btre.2021.e00614>
- 1998 Fantini, M. (2017). Biomass Availability, Potential and Characteristics. In M. Rabaçal, A. F. Ferreira, C.  
1999 A. M. Silva, & M. Costa (Eds.), *Biorefineries* (Vol. 57, pp. 21–54). Springer International  
2000 Publishing. [https://doi.org/10.1007/978-3-319-48288-0\\_2](https://doi.org/10.1007/978-3-319-48288-0_2)
- 2001 Fu, H., Ma, S., Zhao, P., Xu, S., & Zhan, S. (2019). Activation of peroxymonosulfate by graphitized  
2002 hierarchical porous biochar and MnFe<sub>2</sub>O<sub>4</sub> magnetic nanoarchitecture for organic pollutants  
2003 degradation: Structure dependence and mechanism. *Chemical Engineering Journal*, 360, 157–170.  
2004 <https://doi.org/10.1016/j.cej.2018.11.207>
- 2005 Fu, S., Zhang, Y., Xu, X., Dai, X., & Zhu, L. (2022). Peroxymonosulfate activation by iron self-doped  
2006 sludge-derived biochar for degradation of perfluorooctanoic acid: A singlet oxygen-dominated  
2007 nonradical pathway. *Chemical Engineering Journal*, 450, 137953.  
2008 <https://doi.org/10.1016/j.cej.2022.137953>
- 2009 Gale, M., Nguyen, T., Moreno, M., & Gilliard-AbdulAziz, K. L. (2021). Physiochemical Properties of  
2010 Biochar and Activated Carbon from Biomass Residue: Influence of Process Conditions to  
2011 Adsorbent Properties. *ACS Omega*, 6(15), 10224–10233.  
2012 <https://doi.org/10.1021/acsomega.1c00530>
- 2013 Gao, X., Wu, L., Li, Z., Xu, Q., Tian, W., & Wang, R. (2018). Preparation and characterization of high  
2014 surface area activated carbon from pine wood sawdust by fast activation with H<sub>3</sub>PO<sub>4</sub> in a spouted  
2015 bed. *Journal of Material Cycles and Waste Management*, 20(2), 925–936.  
2016 <https://doi.org/10.1007/s10163-017-0653-x>
- 2017 Gao, Y., Chen, Y., Song, T., Su, R., & Luo, J. (2022). Activated peroxymonosulfate with ferric chloride-  
2018 modified biochar to degrade bisphenol A: Characteristics, influencing factors, reaction mechanism



- 2019 and reuse performance. *Separation and Purification Technology*, 300, 121857.
- 2020 <https://doi.org/10.1016/j.seppur.2022.121857>
- 2021 Gebrewold, B. D., Kijjanapanich, P., Rene, E. R., Lens, P. N. L., & Annachhatre, A. P. (2019). Fluoride
- 2022 removal from groundwater using chemically modified rice husk and corn cob activated carbon.
- 2023 *Environmental Technology*, 40(22), 2913–2927. <https://doi.org/10.1080/09593330.2018.1459871>
- 2024 Geczo, A., Giannakoudakis, D. A., Triantafyllidis, K., Elshaer, M. R., Rodríguez-Aguado, E., & Bashkova,
- 2025 S. (2021). Mechanistic insights into acetaminophen removal on cashew nut shell biomass-derived
- 2026 activated carbons. *Environmental Science and Pollution Research*, 28(42), 58969–58982.
- 2027 <https://doi.org/10.1007/s11356-019-07562-0>
- 2028 Girão, A. V., Caputo, G., & Ferro, M. C. (2017). Application of Scanning Electron Microscopy–Energy
- 2029 Dispersive X-Ray Spectroscopy (SEM-EDS). In *Comprehensive Analytical Chemistry* (Vol. 75,
- 2030 pp. 153–168). Elsevier. <https://doi.org/10.1016/bs.coac.2016.10.002>
- 2031 Han, H., Rafiq, M. K., Zhou, T., Xu, R., Mašek, O., & Li, X. (2019). A critical review of clay-based
- 2032 composites with enhanced adsorption performance for metal and organic pollutants. *Journal of*
- 2033 *Hazardous Materials*, 369, 780–796. <https://doi.org/10.1016/j.jhazmat.2019.02.003>
- 2034 Han, L., Yan, J., Qian, L., Zhang, W., & Chen, M. (2019). Multifunctional Pd/Fe-biochar composites for
- 2035 the complete removal of trichlorobenzene and its degradation products. *Journal of Environmental*
- 2036 *Management*, 245, 238–244. <https://doi.org/10.1016/j.jenvman.2019.05.079>
- 2037 Hao, D., Chen, Y., Zhang, Y., & You, N. (2021). Nanocomposites of zero-valent iron@biochar derived
- 2038 from agricultural wastes for adsorptive removal of tetracyclines. *Chemosphere*, 284, 131342.
- 2039 <https://doi.org/10.1016/j.chemosphere.2021.131342>
- 2040 Heidarinejad, Z., Dehghani, M. H., Heidari, M., Javedan, G., Ali, I., & Sillanpää, M. (2020). Methods for
- 2041 preparation and activation of activated carbon: A review. *Environmental Chemistry Letters*, 18(2),
- 2042 393–415. <https://doi.org/10.1007/s10311-019-00955-0>



- 2043 Homagai, P. L., Poudel, R., Poudel, S., & Bhattarai, A. (2022). Adsorption and removal of crystal violet  
2044 dye from aqueous solution by modified rice husk. *Heliyon*, 8(4), e09261.  
2045 <https://doi.org/10.1016/j.heliyon.2022.e09261>
- 2046 Hoslett, J., Ghazal, H., Katsou, E., & Jouhara, H. (2021). The removal of tetracycline from water using  
2047 biochar produced from agricultural discarded material. *Science of The Total Environment*, 751,  
2048 141755. <https://doi.org/10.1016/j.scitotenv.2020.141755>
- 2049 Hou, X., Dong, H., Li, Y., Xiao, J., Dong, Q., Xiang, S., & Chu, D. (2023). Activation of persulfate by  
2050 graphene/biochar composites for phenol degradation: Performance and nonradical dominated  
2051 reaction mechanism. *Journal of Environmental Chemical Engineering*, 11(2), 109348.  
2052 <https://doi.org/10.1016/j.jece.2023.109348>
- 2053 Hu, Y., Chen, D., Zhang, R., Ding, Y., Ren, Z., Fu, M., Cao, X., & Zeng, G. (2021). Singlet oxygen-  
2054 dominated activation of peroxymonosulfate by passion fruit shell derived biochar for catalytic  
2055 degradation of tetracycline through a non-radical oxidation pathway. *Journal of Hazardous*  
2056 *Materials*, 419, 126495. <https://doi.org/10.1016/j.jhazmat.2021.126495>
- 2057 Huang, H., Guo, T., Wang, K., Li, Y., & Zhang, G. (2021). Efficient activation of persulfate by a magnetic  
2058 recyclable rape straw biochar catalyst for the degradation of tetracycline hydrochloride in water.  
2059 *Science of The Total Environment*, 758, 143957. <https://doi.org/10.1016/j.scitotenv.2020.143957>
- 2060 Huang, K., Yang, S., Liu, X., Zhu, C., Qi, F., Wang, K., Wang, J., Wang, Q., Wang, T., & Ma, P. (2023).  
2061 Adsorption of antibiotics from wastewater by cabbage-based N, P co-doped mesoporous carbon  
2062 materials. *Journal of Cleaner Production*, 391, 136174.  
2063 <https://doi.org/10.1016/j.jclepro.2023.136174>
- 2064 Isikgor, F. H., & Becer, C. R. (2015). Lignocellulosic biomass: A sustainable platform for the production  
2065 of bio-based chemicals and polymers. *Polymer Chemistry*, 6(25), 4497–4559.  
2066 <https://doi.org/10.1039/C5PY00263J>
- 2067 Jiang, C., Yakaboylu, G. A., Yumak, T., Zondlo, J. W., Sabolsky, E. M., & Wang, J. (2020). Activated  
2068 carbons prepared by indirect and direct CO<sub>2</sub> activation of lignocellulosic biomass for



- 2069 supercapacitor electrodes. *Renewable Energy*, 155, 38–52.
- 2070 <https://doi.org/10.1016/j.renene.2020.03.111>
- 2071 Jiang, D., Li, H., Cheng, X., Ling, Q., Chen, H., Barati, B., Yao, Q., Abomohra, A., Hu, X., Bartocci, P., &
- 2072 Wang, S. (2023). A mechanism study of methylene blue adsorption on seaweed biomass derived
- 2073 carbon: From macroscopic to microscopic scale. *Process Safety and Environmental Protection*,
- 2074 172, 1132–1143. <https://doi.org/10.1016/j.psep.2023.02.044>
- 2075 Jiang, S.-F., Ling, L.-L., Chen, W.-J., Liu, W.-J., Li, D.-C., & Jiang, H. (2019). High efficient removal of
- 2076 bisphenol A in a peroxymonosulfate/iron functionalized biochar system: Mechanistic elucidation
- 2077 and quantification of the contributors. *Chemical Engineering Journal*, 359, 572–583.
- 2078 <https://doi.org/10.1016/j.cej.2018.11.124>
- 2079 Jiang, Z., Li, J., Jiang, D., Gao, Y., Chen, Y., Wang, W., Cao, B., Tao, Y., Wang, L., & Zhang, Y. (2020).
- 2080 Removal of atrazine by biochar-supported zero-valent iron catalyzed persulfate oxidation:
- 2081 Reactivity, radical production and transformation pathway. *Environmental Research*, 184, 109260.
- 2082 <https://doi.org/10.1016/j.envres.2020.109260>
- 2083 Jiang, Z.-R., Li, Y., Zhou, Y.-X., Liu, X., Wang, C., Lan, Y., & Li, Y. (2022). Co<sub>3</sub>O<sub>4</sub>-MnO<sub>2</sub> nanoparticles
- 2084 moored on biochar as a catalyst for activation of peroxymonosulfate to efficiently degrade
- 2085 sulfonamide antibiotics. *Separation and Purification Technology*, 281, 119935.
- 2086 <https://doi.org/10.1016/j.seppur.2021.119935>
- 2087 Joseph, A. M. (2023). Chemical Modifications of Biomass. In S. Thomas, M. Hosur, D. Pasquini, & C.
- 2088 Jose Chirayil (Eds.), *Handbook of Biomass* (pp. 1–29). Springer Nature Singapore.
- 2089 [https://doi.org/10.1007/978-981-19-6772-6\\_18-1](https://doi.org/10.1007/978-981-19-6772-6_18-1)
- 2090 Ju, M., Rao, P., Yan, L., Gu, D., Li, G., Chen, Q., Liu, S., Zeng, Z., Zhang, M., & Zhang, W. (2023).
- 2091 Synergistic adsorption and degradation of sulfamethazine by tobacco stalk-derived activated
- 2092 biochar: Preparation, mechanism insight and application. *Journal of Environmental Chemical*
- 2093 *Engineering*, 11(3), 110265. <https://doi.org/10.1016/j.jece.2023.110265>



- 2094 Jung, K.-W., Choi, B. H., Hwang, M.-J., Jeong, T.-U., & Ahn, K.-H. (2016). Fabrication of granular  
2095 activated carbons derived from spent coffee grounds by entrapment in calcium alginate beads for  
2096 adsorption of acid orange 7 and methylene blue. *Bioresource Technology*, *219*, 185–195.  
2097 <https://doi.org/10.1016/j.biortech.2016.07.098>
- 2098 Kainth, S., Sharma, P., & Pandey, O. P. (2024). Green sorbents from agricultural wastes: A review of  
2099 sustainable adsorption materials. *Applied Surface Science Advances*, *19*, 100562.  
2100 <https://doi.org/10.1016/j.apsadv.2023.100562>
- 2101 Kambo, H. S., & Dutta, A. (2015). A comparative review of biochar and hydrochar in terms of production,  
2102 physico-chemical properties and applications. *Renewable and Sustainable Energy Reviews*, *45*,  
2103 359–378. <https://doi.org/10.1016/j.rser.2015.01.050>
- 2104 Kandasamy, S., Madhusoodanan, N., Senthilkumar, P., Muneeswaran, V., Manickam, N., & Myneni, V. R.  
2105 (2023). Adsorption of methylene blue dye by animal dung biomass-derived activated carbon:  
2106 Optimization, isotherms and kinetic studies. *Biomass Conversion and Biorefinery*.  
2107 <https://doi.org/10.1007/s13399-023-04710-y>
- 2108 Kaur, P., Hussain, K., Kumar, A., Singh, J., Nagendra Babu, J., & Kumar, S. (2023). Evaluation of  
2109 synergistic adsorption approach for terbinafine removal by cotton shell powder immobilized  
2110 zerovalent copper: Adsorption kinetics and DFT simulation. *Environmental Nanotechnology,  
2111 Monitoring & Management*, *20*, 100875. <https://doi.org/10.1016/j.enmm.2023.100875>
- 2112 Kaur, P., Kalpana, Kumar, S., Kumar, A., & Kumar, A. (2023). Effect of various sodium hydroxide  
2113 treatment parameters on the adsorption efficiency of rice husk for removal of methylene blue from  
2114 water. *Emergent Materials*, *6*(6), 1809–1824. <https://doi.org/10.1007/s42247-023-00574-0>
- 2115 Kaur, P., Kumar, A., Babu, J. N., & Kumar, S. (2023). Tetracycline removal via three-way synergy between  
2116 pistachio shell powder, zerovalent copper or iron, and peroxymonosulfate activation. *Journal of  
2117 Hazardous Materials Advances*, *12*, 100385. <https://doi.org/10.1016/j.hazadv.2023.100385>
- 2118 Kaur, P., Kumar, S., Rani, J., Singh, J., Kaushal, S., Hussain, K., Nagendra Babu, J., & Mittal, S. (2024a).  
2119 Rationally tailored synergy between adsorption efficiency of cotton shell activated carbon and PMS



- 2120 activation via biogenic Fe<sup>0</sup> or Cu<sup>0</sup> for effective mitigation of triphenylmethane dyes. *Separation*  
2121 *and Purification Technology*, 342, 127010. <https://doi.org/10.1016/j.seppur.2024.127010>
- 2122 Kaur, P., Kumar, S., Rani, J., Babu, J., & Mittal, S. (2024b). Comparison of surface adsorption efficacies  
2123 of eco-sustainable agro/animal biomass-derived activated carbon for the removal of rhodamine B  
2124 and hexavalent chromium. *Environmental Science and Pollution Research*, 31(39), 52371-52390.  
2125 <https://doi.org/10.1007/s11356-024-34686-9>
- 2126 Katheresan, V., Kansedo, J., & Lau, S.Y. (2018). Efficiency of various recent wastewater dye removal  
2127 methods: A review. *Journal of Environmental Chemical Engineering*, 6(4), 4676–4697.  
2128 <https://doi.org/10.1016/j.jece.2018.06.060>
- 2129 Kebir, M., Tahraoui, H., Chabani, M., Trari, M., Noureddine, N., Assadi, A. A., Amrane, A., Ben Hamadi,  
2130 N., & Khezami, L. (2023). Water Cleaning by a Continuous Fixed-Bed Column for Cr(VI) Eco-  
2131 Adsorption with Green Adsorbent-Based Biomass: An Experimental Modeling Study. *Processes*,  
2132 11(2), 363. <https://doi.org/10.3390/pr11020363>
- 2133 Kharrazi, S. M., Soleimani, M., Jokar, M., Richards, T., Pettersson, A., & Mirghaffari, N. (2021).  
2134 Pretreatment of lignocellulosic waste as a precursor for synthesis of high porous activated carbon  
2135 and its application for Pb (II) and Cr (VI) adsorption from aqueous solutions. *International Journal*  
2136 *of Biological Macromolecules*, 180, 299–310. <https://doi.org/10.1016/j.ijbiomac.2021.03.078>
- 2137 Kumar Mishra, R., Singh, B., & Acharya, B. (2024). A comprehensive review on activated carbon from  
2138 pyrolysis of lignocellulosic biomass: An application for energy and the environment. *Carbon*  
2139 *Resources Conversion*, 7(4), 100228. <https://doi.org/10.1016/j.crcon.2024.100228>
- 2140 Kumar, S., Brar, R. S., Babu, J. N., Dahiya, A., Saha, S., & Kumar, A. (2021). Synergistic effect of pistachio  
2141 shell powder and nano-zerovalent copper for chromium remediation from aqueous solution.  
2142 *Environmental Science and Pollution Research*, 28(44), 63422–63436.  
2143 <https://doi.org/10.1007/s11356-021-15285-4>
- 2144 Kumar, S., Brar, R. S., Saha, S., Dahiya, A., Kalpana, & Babu, J. N. (2023). Synergistic effect of eco-  
2145 friendly pistachio shell biomass on nano-MnO<sub>2</sub> for crystal violet removal: Kinetic and equilibrium



- 2146 studies. *International Journal of Environmental Science and Technology*, 20(5), 5123–5140.  
2147 <https://doi.org/10.1007/s13762-022-04212-w>
- 2148 Kumar, S., Kaur, P., Brar, R. S., & Babu, J. N. (2022). Nanoscale zerovalent copper (nZVC) catalyzed  
2149 environmental remediation of organic and inorganic contaminants: A review. *Heliyon*, 8(8),  
2150 e10140. <https://doi.org/10.1016/j.heliyon.2022.e10140>
- 2151 Kumar, S., Kaur, P., Rani, J., Singh, J., Kaushal, S., Babu, J. N., & Mittal, S. (2025). Synergistic impact of  
2152 rice husk biomass derived carbon supports on the performance of biogenic Fe<sup>0</sup>-catalyzed advanced  
2153 oxidation processes for oxytetracycline remediation. *Environmental Science: Water Research &*  
2154 *Technology*, 11(2), 242-261. DOI: <https://doi.org/10.1039/d4ew00912f>
- 2155 Lai, C., Huang, F., Zeng, G., Huang, D., Qin, L., Cheng, M., Zhang, C., Li, B., Yi, H., Liu, S., Li, L., &  
2156 Chen, L. (2019). Fabrication of novel magnetic MnFe<sub>2</sub>O<sub>4</sub>/bio-char composite and heterogeneous  
2157 photo-Fenton degradation of tetracycline in near neutral pH. *Chemosphere*, 224, 910–921.  
2158 <https://doi.org/10.1016/j.chemosphere.2019.02.193>
- 2159 Leichtweis, J., Welter, N., Vieira, Y., Storck, T. R., Clasen, B., Silvestri, S., & Carissimi, E. (2023). Use of  
2160 a new ZnFe<sub>2</sub>O<sub>4</sub>/biochar composite for degradation and ecotoxicity assessment of effluent  
2161 containing methylene blue dye. *Journal of Photochemistry and Photobiology A: Chemistry*, 440,  
2162 114676. <https://doi.org/10.1016/j.jphotochem.2023.114676>
- 2163 Li, H., Qiu, Y., Wang, X., Yang, J., Yu, Y., Chen, Y., & Liu, Y. (2017). Biochar supported Ni/Fe bimetallic  
2164 nanoparticles to remove 1,1,1-trichloroethane under various reaction conditions. *Chemosphere*,  
2165 169, 534–541. <https://doi.org/10.1016/j.chemosphere.2016.11.117>
- 2166 Li, W., Liu, B., Wang, Z., Wang, K., Lan, Y., & Zhou, L. (2020). Efficient activation of peroxydisulfate  
2167 (PDS) by rice straw biochar modified by copper oxide (RSBC-CuO) for the degradation of  
2168 phenacetin (PNT). *Chemical Engineering Journal*, 395, 125094.  
2169 <https://doi.org/10.1016/j.cej.2020.125094>



- 2170 Li, X., Wang, C., Chen, X., Li, D., & Jin, Q. (2023). Enhanced oxidation and removal of As(III) from water  
2171 using biomass-derived porous carbon-supported nZVI with high iron utilization and fast  
2172 adsorption. *Journal of Environmental Chemical Engineering*, 11(1), 109038.  
2173 <https://doi.org/10.1016/j.jece.2022.109038>
- 2174 Li, X., Zhang, S., Zhang, M., Yu, M., Chen, H., Yang, H., & Xu, Q. (2021). One-step synthesis of mixed  
2175 valence FeOX nanoparticles supported on biomass activated carbon for degradation of bisphenol  
2176 A by activating peroxydisulfate. *Journal of Hazardous Materials*, 409, 124990.  
2177 <https://doi.org/10.1016/j.jhazmat.2020.124990>
- 2178 Li, Y., Yang, J., Zhang, M., Yang, Z., Shih, K., Ying, G.-G., & Feng, Y. (2023). Coupled Adsorption and  
2179 Surface-Bound Radical-Mediated Oxidation on Biomass-Derived Porous Carbon: A Selective  
2180 Approach for Sulfamethoxazole Removal. *Chemical Engineering Journal*, 452, 139484.  
2181 <https://doi.org/10.1016/j.cej.2022.139484>
- 2182 Li, Z., Deng, S., An, Q., Zhao, B., Yang, Z., Xu, B., & Zhang, W. (2024). Enhanced activation of persulfate  
2183 by modified red mud biochar for degradation of dye pollutant: Resource utilization and non-radical  
2184 activation. *Journal of Environmental Management*, 353, 120181.  
2185 <https://doi.org/10.1016/j.jenvman.2024.120181>
- 2186 Li, Z., Sun, Y., Yang, Y., Han, Y., Wang, T., Chen, J., & Tsang, D. C. W. (2020). Biochar-supported  
2187 nanoscale zero-valent iron as an efficient catalyst for organic degradation in groundwater. *Journal  
2188 of Hazardous Materials*, 383, 121240. <https://doi.org/10.1016/j.jhazmat.2019.121240>
- 2189 Liu, B., Guo, W., Wang, H., Si, Q., Zhao, Q., Luo, H., & Ren, N. (2020). Activation of peroxymonosulfate  
2190 by cobalt-impregnated biochar for atrazine degradation: The pivotal roles of persistent free radicals  
2191 and ecotoxicity assessment. *Journal of Hazardous Materials*, 398, 122768.  
2192 <https://doi.org/10.1016/j.jhazmat.2020.122768>
- 2193 Liu, J., Jiang, J., Wang, M., Kang, J., Zhang, J., Liu, S., Tang, Y., & Li, S. (2022). Peroxymonosulfate  
2194 activation by cobalt particles embedded into biochar for levofloxacin degradation: Efficiency,



- 2195 stability, and mechanism. *Separation and Purification Technology*, 294, 121082.
- 2196 <https://doi.org/10.1016/j.seppur.2022.121082>
- 2197 Liu, T., Wang, Q., Li, C., Cui, M., Chen, Y., Liu, R., Cui, K., Wu, K., Nie, X., & Wang, S. (2022).
- 2198 Synthesizing and characterizing Fe<sub>3</sub>O<sub>4</sub> embedded in N-doped carbon nanotubes-bridged biochar
- 2199 as a persulfate activator for sulfamethoxazole degradation. *Journal of Cleaner Production*, 353,
- 2200 131669. <https://doi.org/10.1016/j.jclepro.2022.131669>
- 2201 Liu, X., Li, Q., Zhang, Y., Zhong, F., Ding, X., & Yu, Z. (2024). Synthesis of micro-mesoporous
- 2202 hierarchical structure of coal-based activated carbon and its effect on methane adsorption. *Fuel*,
- 2203 365, 131239. <https://doi.org/10.1016/j.fuel.2024.131239>
- 2204 Liu, X., Shao, Z., Wang, Y., Liu, Y., Wang, S., Gao, F., & Dai, Y. (2023). New use for Lentinus edodes
- 2205 bran biochar for tetracycline removal. *Environmental Research*, 216, 114651.
- 2206 <https://doi.org/10.1016/j.envres.2022.114651>
- 2207 Liu, Y., Huang, B., Lin, X., & Xie, Z. (2017). Biomass-derived hierarchical porous carbons: Boosting the
- 2208 energy density of supercapacitors via an ionothermal approach. *Journal of Materials Chemistry A*,
- 2209 5(25), 13009–13018. <https://doi.org/10.1039/C7TA03639F>
- 2210 Liu, Y., Sohi, S. P., Liu, S., Guan, J., Zhou, J., & Chen, J. (2019). Adsorption and reductive degradation of
- 2211 Cr(VI) and TCE by a simply synthesized zero valent iron magnetic biochar. *Journal of*
- 2212 *Environmental Management*, 235, 276–281. <https://doi.org/10.1016/j.jenvman.2019.01.045>
- 2213 Loo, W. W., Pang, Y. L., Lim, S., Wong, K. H., Lai, C. W., & Abdullah, A. Z. (2021). Enhancement of
- 2214 photocatalytic degradation of Malachite Green using iron doped titanium dioxide loaded on oil
- 2215 palm empty fruit bunch-derived activated carbon. *Chemosphere*, 272, 129588.
- 2216 <https://doi.org/10.1016/j.chemosphere.2021.129588>
- 2217 Lu, L., Yu, W., Wang, Y., Zhang, K., Zhu, X., Zhang, Y., Wu, Y., Ullah, H., Xiao, X., & Chen, B. (2020).
- 2218 Application of biochar-based materials in environmental remediation: From multi-level structures
- 2219 to specific devices. *Biochar*, 2(1), 1–31. <https://doi.org/10.1007/s42773-020-00041-7>



- 2220 Ma, D., Yang, Y., Liu, B., Xie, G., Chen, C., Ren, N., & Xing, D. (2021). Zero-valent iron and biochar  
2221 composite with high specific surface area via K<sub>2</sub>FeO<sub>4</sub> fabrication enhances sulfadiazine removal  
2222 by persulfate activation. *Chemical Engineering Journal*, 408, 127992.  
2223 <https://doi.org/10.1016/j.cej.2020.127992>
- 2224 Mahmood-ul-Hassan, M., Suthor, V., Rafique, E., & Yasin, M. (2015). Removal of Cd, Cr, and Pb from  
2225 aqueous solution by unmodified and modified agricultural wastes. *Environmental Monitoring and*  
2226 *Assessment*, 187(2), 19. <https://doi.org/10.1007/s10661-014-4258-8>
- 2227 Maia, L. S., Da Silva, A. I. C., Carneiro, E. S., Monticelli, F. M., Pinhati, F. R., & Mulinari, D. R. (2021).  
2228 Activated Carbon From Palm Fibres Used as an Adsorbent for Methylene Blue Removal. *Journal*  
2229 *of Polymers and the Environment*, 29(4), 1162–1175. [https://doi.org/10.1007/s10924-020-01951-](https://doi.org/10.1007/s10924-020-01951-0)  
2230 [0](https://doi.org/10.1007/s10924-020-01951-0)
- 2231 Mankar, A. R., Pandey, A., Modak, A., & Pant, K. K. (2021). Pretreatment of lignocellulosic biomass: A  
2232 review on recent advances. *Bioresource Technology*, 334, 125235.  
2233 <https://doi.org/10.1016/j.biortech.2021.125235>
- 2234 Mao, Q., Zhou, Y., Yang, Y., Zhang, J., Liang, L., Wang, H., Luo, S., Luo, L., Jeyakumar, P., Ok, Y. S., &  
2235 Rizwan, M. (2019). Experimental and theoretical aspects of biochar-supported nanoscale zero-  
2236 valent iron activating H<sub>2</sub>O<sub>2</sub> for ciprofloxacin removal from aqueous solution. *Journal of*  
2237 *Hazardous Materials*, 380, 120848. <https://doi.org/10.1016/j.jhazmat.2019.120848>
- 2238 Masoudian, N., Rajabi, M., & Ghaedi, M. (2019). Titanium oxide nanoparticles loaded onto activated  
2239 carbon prepared from bio-waste watermelon rind for the efficient ultrasonic-assisted adsorption of  
2240 congo red and phenol red dyes from wastewaters. *Polyhedron*, 173, 114105.  
2241 <https://doi.org/10.1016/j.poly.2019.114105>
- 2242 Masoumi, S., Borugadda, V. B., Nanda, S., & Dalai, A. K. (2021). Hydrochar: A Review on Its Production  
2243 Technologies and Applications. *Catalysts*, 11(8), 939. <https://doi.org/10.3390/catal11080939>
- 2244 Mazarji, M., Bayero, M. T., Minkina, T., Sushkova, S., Mandzhieva, S., Bauer, T. V., Soldatov, A.,  
2245 Sillanpää, M., & Wong, M. H. (2023). Nanomaterials in biochar: Review of their effectiveness in



- 2246 remediating heavy metal-contaminated soils. *Science of The Total Environment*, 880, 163330.  
2247 <https://doi.org/10.1016/j.scitotenv.2023.163330>
- 2248 Menéndez, J. A., Arenillas, A., Fidalgo, B., Fernández, Y., Zubizarreta, L., Calvo, E. G., & Bermúdez, J.  
2249 M. (2010). Microwave heating processes involving carbon materials. *Fuel Processing Technology*,  
2250 91(1), 1–8. <https://doi.org/10.1016/j.fuproc.2009.08.021>
- 2251 Mishra, S., Cheng, L., & Maiti, A. (2021). The utilization of agro-biomass/byproducts for effective bio-  
2252 removal of dyes from dyeing wastewater: A comprehensive review. *Journal of Environmental*  
2253 *Chemical Engineering*, 9(1), 104901. <https://doi.org/10.1016/j.jece.2020.104901>
- 2254 Mishra, S., & Upadhyay, R. K. (2021). Review on biomass gasification: Gasifiers, gasifying mediums, and  
2255 operational parameters. *Materials Science for Energy Technologies*, 4, 329–340.  
2256 <https://doi.org/10.1016/j.mset.2021.08.009>
- 2257 Mujtaba, M., Fernandes Fraceto, L., Fazeli, M., Mukherjee, S., Savassa, S. M., Araujo De Medeiros, G.,  
2258 Do Espírito Santo Pereira, A., Mancini, S. D., Lipponen, J., & Vilaplana, F. (2023). Lignocellulosic  
2259 biomass from agricultural waste to the circular economy: A review with focus on biofuels,  
2260 biocomposites and bioplastics. *Journal of Cleaner Production*, 402, 136815.  
2261 <https://doi.org/10.1016/j.jclepro.2023.136815>
- 2262 Nair, R. R., Mondal, M. M., Srinivasan, S. V., & Weichgrebe, D. (2022). Biochar Synthesis from Mineral-  
2263 and Ash-Rich Waste Biomass, Part 1: Investigation of Thermal Decomposition Mechanism during  
2264 Slow Pyrolysis. *Materials*, 15(12), 4130. <https://doi.org/10.3390/ma15124130>
- 2265 Nayak, A., Bhushan, B., & Kotnala, S. (2024). Fundamentals and mechanism of adsorption. In *Sustainable*  
2266 *Technologies for Remediation of Emerging Pollutants from Aqueous Environment* (pp. 29–62).  
2267 Elsevier. <https://doi.org/10.1016/B978-0-443-18618-9.00002-4>
- 2268 Neolaka, Y. A. B., Lawa, Y., Naat, J., Riwu, A. A. P., Darmokoesoemo, H., Widyaningrum, B. A., Iqbal,  
2269 M., & Kusuma, H. S. (2021). Indonesian Kesambi wood (*Schleichera oleosa*) activated with  
2270 pyrolysis and H<sub>2</sub>SO<sub>4</sub> combination methods to produce mesoporous activated carbon for Pb(II)



- 2271 adsorption from aqueous solution. *Environmental Technology & Innovation*, 24, 101997.  
2272 <https://doi.org/10.1016/j.eti.2021.101997>
- 2273 Nguyen, D. V., Nguyen, H. M., Bui, Q. L. N., Do, T. V. T., Lam, H. H., Tran-Thuy, T.-M., & Nguyen, L.  
2274 Q. (2023). Magnetic Activated Carbon from ZnCl<sub>2</sub> and FeCl<sub>3</sub> Coactivation of Lotus Seedpod:  
2275 One-Pot Preparation, Characterization, and Catalytic Activity towards Robust Degradation of Acid  
2276 Orange 10. *Bioinorganic Chemistry and Applications*, 2023, 1–17.  
2277 <https://doi.org/10.1155/2023/3848456>
- 2278 Nguyen, T. A., & Oh, S. (2019). Biochar-mediated oxidation of phenol by persulfate activated with  
2279 zero-valent iron. *Journal of Chemical Technology & Biotechnology*, 94(12), 3932–3940.  
2280 <https://doi.org/10.1002/jctb.6194>
- 2281 Nguyen, V.-T., Nguyen, T.-B., Chen, C.-W., Hung, C.-M., Huang, C. P., & Dong, C.-D. (2019). Cobalt-  
2282 impregnated biochar (Co-SCG) for heterogeneous activation of peroxymonosulfate for removal of  
2283 tetracycline in water. *Bioresource Technology*, 292, 121954.  
2284 <https://doi.org/10.1016/j.biortech.2019.121954>
- 2285 Norouzi, S., Heidari, M., Alipour, V., Rahmanian, O., Fazlzadeh, M., Mohammadi-moghadam, F.,  
2286 Nourmoradi, H., Goudarzi, B., & Dindarloo, K. (2018). Preparation, characterization and Cr(VI)  
2287 adsorption evaluation of NaOH-activated carbon produced from Date Press Cake; an agro-  
2288 industrial waste. *Bioresource Technology*, 258, 48–56.  
2289 <https://doi.org/10.1016/j.biortech.2018.02.106>
- 2290 Nyirenda, J., Kalaba, G., & Munyati, O. (2022). Synthesis and characterization of an activated carbon-  
2291 supported silver-silica nanocomposite for adsorption of heavy metal ions from water. *Results in*  
2292 *Engineering*, 15, 100553. <https://doi.org/10.1016/j.rineng.2022.100553>
- 2293 Oginni, O., Singh, K., Oporto, G., Dawson-Andoh, B., McDonald, L., & Sabolsky, E. (2019). Effect of  
2294 one-step and two-step H<sub>3</sub>PO<sub>4</sub> activation on activated carbon characteristics. *Bioresource*  
2295 *Technology Reports*, 8, 100307. <https://doi.org/10.1016/j.biteb.2019.100307>



- 2296 Ogungbenro, A. E., Quang, D. V., Al-Ali, K. A., Vega, L. F., & Abu-Zahra, M. R. M. (2020). Synthesis  
2297 and characterization of activated carbon from biomass date seeds for carbon dioxide adsorption.  
2298 *Journal of Environmental Chemical Engineering*, 8(5), 104257.  
2299 <https://doi.org/10.1016/j.jece.2020.104257>
- 2300 Oh, S.-Y., Seo, Y.-D., Ryu, K.-S., Park, D.-J., & Lee, S.-H. (2017). Redox and catalytic properties of  
2301 biochar-coated zero-valent iron for the removal of nitro explosives and halogenated phenols.  
2302 *Environmental Science: Processes & Impacts*, 19(5), 711–719.  
2303 <https://doi.org/10.1039/C7EM00035A>
- 2304 Pallarés, J., González-Cencerrado, A., & Arauzo, I. (2018). Production and characterization of activated  
2305 carbon from barley straw by physical activation with carbon dioxide and steam. *Biomass and*  
2306 *Bioenergy*, 115, 64–73. <https://doi.org/10.1016/j.biombioe.2018.04.015>
- 2307 Pérez-Millán, T. M., Mendoza-Castillo, D. I., Aguayo-Villarreal, I. A., Rojas-Mayorga, C. K., Villanueva-  
2308 Mejía, F., & Bonilla-Petriciolet, A. (2023). Application of DFT and Response Surface Models to  
2309 analyze the adsorption process of basic blue 3 and reactive blue 19 dyes on sugarcane bagasse and  
2310 coconut endocarp biomass. *Journal of Molecular Structure*, 1287, 135658.  
2311 <https://doi.org/10.1016/j.molstruc.2023.135658>
- 2312 Phiri, R., Mavinkere Rangappa, S., & Siengchin, S. (2024). Agro-waste for renewable and sustainable green  
2313 production: A review. *Journal of Cleaner Production*, 434, 139989.  
2314 <https://doi.org/10.1016/j.jclepro.2023.139989>
- 2315 Qian, L., Liu, S., Zhang, W., Chen, Y., Ouyang, D., Han, L., Yan, J., & Chen, M. (2019). Enhanced  
2316 reduction and adsorption of hexavalent chromium by palladium and silicon rich biochar supported  
2317 nanoscale zero-valent iron. *Journal of Colloid and Interface Science*, 533, 428–436.  
2318 <https://doi.org/10.1016/j.jcis.2018.08.075>
- 2319 Qin, F., Peng, Y., Song, G., Fang, Q., Wang, R., Zhang, C., Zeng, G., Huang, D., Lai, C., Zhou, Y., Tan,  
2320 X., Cheng, M., & Liu, S. (2020). Degradation of sulfamethazine by biochar-supported bimetallic



- 2321 oxide/persulfate system in natural water: Performance and reaction mechanism. *Journal of*  
2322 *Hazardous Materials*, 398, 122816. <https://doi.org/10.1016/j.jhazmat.2020.122816>
- 2323 Qin, Y., Chai, B., Wang, C., Yan, J., Fan, G., & Song, G. (2022). Removal of tetracycline onto KOH-  
2324 activated biochar derived from rape straw: Affecting factors, mechanisms and reusability  
2325 inspection. *Colloids and Surfaces A: Physicochemical and Engineering Aspects*, 640, 128466.  
2326 <https://doi.org/10.1016/j.colsurfa.2022.128466>
- 2327 Qu, H., Chen, L., Yang, F., Zhu, J., Qi, C., & Peng, G. (2023). Synthesis of an Environmentally Friendly  
2328 Modified Mulberry Branch-Derived Biochar Composite: High Degradation Efficiency of BPA and  
2329 Mitigation of Toxicity in Silkworm Larvae. *International Journal of Molecular Sciences*, 24(4),  
2330 3609. <https://doi.org/10.3390/ijms24043609>
- 2331 Qu, K., Huang, L., Hu, S., Liu, C., Yang, Q., Liu, L., Li, K., Zhao, Z., & Wang, Z. (2023). TiO<sub>2</sub> supported  
2332 on rice straw biochar as an adsorptive and photocatalytic composite for the efficient removal of  
2333 ciprofloxacin in aqueous matrices. *Journal of Environmental Chemical Engineering*, 11(2),  
2334 109430. <https://doi.org/10.1016/j.jece.2023.109430>
- 2335 Rane, A. V., Kanny, K., Abitha, V. K., & Thomas, S. (2018). Methods for Synthesis of Nanoparticles and  
2336 Fabrication of Nanocomposites. In *Synthesis of Inorganic Nanomaterials* (pp. 121–139). Elsevier.  
2337 <https://doi.org/10.1016/B978-0-08-101975-7.00005-1>
- 2338 Rani, J., Goyal, T., Kaur, A., Ganesan, S., Sharma, A. K., Chauhan, A. S. Kaushal, S., Kumar, S. (2025a).  
2339 Bimetallic nanoparticles as pioneering eco-friendly catalysts for remediation of pharmaceuticals  
2340 and personal care products (PPCPs). *Nanoscale Advances*. 7, 3160–3188.  
2341 <https://doi.org/10.1039/D5NA00151J>
- 2342 Rani, J., Kumar, S., Goyal, T., Sharma, A., Singh, J., Kaushal, S., Hussain, K., Babu, J. N. (2025b).  
2343 Multifunctional Fe and Fe-Mn nanostructured graphitic carbon nitrides (g-C<sub>3</sub>N<sub>4</sub>): Photocatalytic  
2344 degradation of Tetracycline and Radiation shielding. *Surfaces and Interfaces*, 73, 107595.  
2345 <https://doi.org/10.1016/j.surfin.2025.107595>



- 2346 Reguyal, F., & Sarmah, A. K. (2018). Adsorption of sulfamethoxazole by magnetic biochar: Effects of pH,  
2347 ionic strength, natural organic matter and 17 $\alpha$ -ethinylestradiol. *Science of The Total Environment*,  
2348 628–629, 722–730. <https://doi.org/10.1016/j.scitotenv.2018.01.323>
- 2349 Saini, J., Garg, V. K., Gupta, R. K., & Kataria, N. (2017). Removal of Orange G and Rhodamine B dyes  
2350 from aqueous system using hydrothermally synthesized zinc oxide loaded activated carbon (ZnO-  
2351 AC). *Journal of Environmental Chemical Engineering*, 5(1), 884–892.  
2352 <https://doi.org/10.1016/j.jece.2017.01.012>
- 2353 Sajjadi, S.-A., Mohammadzadeh, A., Tran, H. N., Anastopoulos, I., Dotto, G. L., Lopičić, Z. R., Sivamani,  
2354 S., Rahmani-Sani, A., Ivanets, A., & Hosseini-Bandegharai, A. (2018). Efficient mercury removal  
2355 from wastewater by pistachio wood wastes-derived activated carbon prepared by chemical  
2356 activation using a novel activating agent. *Journal of Environmental Management*, 223, 1001–1009.  
2357 <https://doi.org/10.1016/j.jenvman.2018.06.077>
- 2358 Salomón-Negrete, M. Á., Reynel-Ávila, H. E., Mendoza-Castillo, D. I., Bonilla-Petriciolet, A., & Duran-  
2359 Valle, C. J. (2018). Water defluoridation with avocado-based adsorbents: Synthesis,  
2360 physicochemical characterization and thermodynamic studies. *Journal of Molecular Liquids*, 254,  
2361 188–197. <https://doi.org/10.1016/j.molliq.2018.01.084>
- 2362 Sang, F., Yin, Z., Wang, W., Almatrafi, E., Wang, Y., Zhao, B., Gong, J., Zhou, C., Zhang, C., Zeng, G.,  
2363 & Song, B. (2022). Degradation of ciprofloxacin using heterogeneous Fenton catalysts derived  
2364 from natural pyrite and rice straw biochar. *Journal of Cleaner Production*, 378, 134459.  
2365 <https://doi.org/10.1016/j.jclepro.2022.134459>
- 2366 Sangeetha Piriya, R., Jayabalakrishnan, R. M., Maheswari, M., Boomiraj, K., & Oumabady, S. (2021).  
2367 Coconut shell derived ZnCl<sub>2</sub> activated carbon for malachite green dye removal. *Water Science and*  
2368 *Technology*, 83(5), 1167–1182. <https://doi.org/10.2166/wst.2021.050>
- 2369 Sargazi, G., Afzali, D., Mostafavi, A., Shadman, A., Rezaee, B., Zarrintaj, P., Saeb, M. R., Ramakrishna,  
2370 S., & Mozafari, M. (2019). Chitosan/polyvinyl alcohol nanofibrous membranes: Towards green



- 2371 super-adsorbents for toxic gases. *Heliyon*, 5(4), e01527.  
2372 <https://doi.org/10.1016/j.heliyon.2019.e01527>
- 2373 Schlumberger, C., & Thommes, M. (2021). Characterization of Hierarchically Ordered Porous Materials  
2374 by Physisorption and Mercury Porosimetry—A Tutorial Review. *Advanced Materials Interfaces*,  
2375 8(4), 2002181. <https://doi.org/10.1002/admi.202002181>
- 2376 Sen, T. K. (2023). Application of Synthesized Biomass Bamboo Charcoal–Iron Oxide “BC/Fe”  
2377 Nanocomposite Adsorbents in the Removal of Cationic Methylene Blue Dye Contaminants from  
2378 Wastewater by Adsorption. *Sustainability*, 15(11), 8841. <https://doi.org/10.3390/su15118841>
- 2379 Seo, G., Annamalai, S., & Shin, W. S. (2023). Enhancement of peroxydisulfate activation by inherent nature  
2380 of Fe-N-P/C biochar derived from *Capsosiphon fulvescens* as a green biomass material for organic  
2381 pollutants degradation. *Chemical Engineering Journal*, 475, 146445.  
2382 <https://doi.org/10.1016/j.ccej.2023.146445>
- 2383 Shang, X., Yang, L., Ouyang, D., Zhang, B., Zhang, W., Gu, M., Li, J., Chen, M., Huang, L., & Qian, L.  
2384 (2020). Enhanced removal of 1,2,4-trichlorobenzene by modified biochar supported nanoscale  
2385 zero-valent iron and palladium. *Chemosphere*, 249, 126518.  
2386 <https://doi.org/10.1016/j.chemosphere.2020.126518>
- 2387 Shao, Y., Li, J., Fang, X., Yang, Z., Qu, Y., Yang, M., Tan, W., Li, G., & Wang, H. (2022). Chemical  
2388 modification of bamboo activated carbon surface and its adsorption property of simultaneous  
2389 removal of phosphate and nitrate. *Chemosphere*, 287, 132118.  
2390 <https://doi.org/10.1016/j.chemosphere.2021.132118>
- 2391 Shi, J., Dai, B., Shen, X., Xu, L., Zhang, Y., & Gan, L. (2023). Wood induced preparation of Fe<sub>3</sub>C decorated  
2392 biochar for peroxymonosulfate activation towards bisphenol a degradation with low ion leaching.  
2393 *Journal of Environmental Management*, 340, 117978.  
2394 <https://doi.org/10.1016/j.jenvman.2023.117978>
- 2395 Sing, K. S. W. (1995). Physisorption of nitrogen by porous materials. *Journal of Porous Materials*, 2(1),  
2396 5–8. <https://doi.org/10.1007/BF00486564>



- 2397 Singh, M. (2023). Engineered Biochar-Based Nanocomposites: A Sustainable Solution for Smart  
2398 Agriculture. In D. Mishra, R. Singh, & P. Khare (Eds.), *Biochar-Based Nanocomposites for*  
2399 *Contaminant Management* (pp. 119–131). Springer International Publishing.  
2400 [https://doi.org/10.1007/978-3-031-28873-9\\_10](https://doi.org/10.1007/978-3-031-28873-9_10)
- 2401 Srinivasan, P., John Bosco, A., Kalaivizhi, R., Arockia Selvi, J., & Sivakumar, P. (2021). Adsorption  
2402 isotherm and kinetic study of Direct Orange 102 dyes on TNJ activated carbon. *Materials Today:*  
2403 *Proceedings*, 34, 389–394. <https://doi.org/10.1016/j.matpr.2020.02.198>
- 2404 Suárez, L., & Centeno, T. A. (2020). Unravelling the volumetric performance of activated carbons from  
2405 biomass wastes in supercapacitors. *Journal of Power Sources*, 448, 227413.  
2406 <https://doi.org/10.1016/j.jpowsour.2019.227413>
- 2407 Sutradhar, S., Mondal, A., Kuehne, F., Krueger, O., Rakshit, S. K., & Kang, K. (2024). Comparison of Oil-  
2408 Seed Shell Biomass-Based Biochar for the Removal of Anionic Dyes—Characterization and  
2409 Adsorption Efficiency Studies. *Plants*, 13(6), 820. <https://doi.org/10.3390/plants13060820>
- 2410 Tang, Q., Meng, X., Bao, W., Fan, Y., Gao, Y., Sun, Y., & Liu, H. (2023). Synergistic activation of  
2411 peroxydisulfate by nitrogen-doped biochar loaded with mixed-valence iron nanoparticles for  
2412 tetracycline degradation. *Colloids and Surfaces A: Physicochemical and Engineering Aspects*, 669,  
2413 131490. <https://doi.org/10.1016/j.colsurfa.2023.131490>
- 2414 Tang, R., Dai, C., Li, C., Liu, W., Gao, S., & Wang, C. (2017). Removal of Methylene Blue from Aqueous  
2415 Solution Using Agricultural Residue Walnut Shell: Equilibrium, Kinetic, and Thermodynamic  
2416 Studies. *Journal of Chemistry*, 1–10. <https://doi.org/10.1155/2017/8404965>
- 2417 Thamarai, P., Karishma, S., Deivayanai, V. C., Saravanan, A., & Yaashikaa, P. R. (2024a). Theoretical and  
2418 experimental analysis of Pb (II) ion adsorption using surface modified macroalgal biosorbents:  
2419 modelling and desorption study. *Industrial & Engineering Chemistry Research*, 63(49), 21505-  
2420 21518. <https://doi/10.1021/acs.iecr.4c02591>
- 2421 Thamarai, P., Deivayanai, V. C., Karishma, S., Saravanan, A., Yaashikaa, P. R., & Vickram, A. S. (2024b).  
2422 Adsorption strategies in surface modification techniques for seaweeds in wastewater treatment:



- 2423 exploring environmental applications. *Reviews of Environmental Contamination and*  
2424 *Toxicology*, 262(1), 18. <https://doi.org/10.1007/s44169-024-00071-3>
- 2425 Thamarai, P., Deivayanai, V. C., Swaminaathan, P., Karishma, S., Vickram, A. S., & Yaashikaa, P. R.  
2426 (2024c). Experimental investigation of Cd (II) ion adsorption on surface-modified mixed seaweed  
2427 Biosorbent: A study on analytical interpretation and thermodynamics. *Environmental*  
2428 *research*, 260, 119670. <https://doi.org/10.1016/j.envres.2024.119670>
- 2429 Thompson, C. O., Ndukwe, A. O., & Asadu, C. O. (2020). Application of activated biomass waste as an  
2430 adsorbent for the removal of lead (II) ion from wastewater. *Emerging Contaminants*, 6, 259–267.  
2431 <https://doi.org/10.1016/j.emcon.2020.07.003>
- 2432 Tian, H., Cui, K., Sun, S., Liu, J., & Cui, M. (2023). Sequential doping of exogenous iron and nitrogen to  
2433 prepare Fe-N structured biochar to enhance the activity of OTC degradation. *Separation and*  
2434 *Purification Technology*, 322, 124249. <https://doi.org/10.1016/j.seppur.2023.124249>
- 2435 Tian, H., Peng, S., Zhao, L., Chen, Y., & Cui, K. (2023). Simultaneous adsorption of Cd(II) and degradation  
2436 of OTC by activated biochar with ferrate: Efficiency and mechanism. *Journal of Hazardous*  
2437 *Materials*, 447, 130711. <https://doi.org/10.1016/j.jhazmat.2022.130711>
- 2438 Tomczyk, A., & Szewczuk-Karpisz, K. (2022). Effect of Biochar Modification by Vitamin C, Hydrogen  
2439 Peroxide or Silver Nanoparticles on Its Physicochemistry and Tetracycline Removal. *Materials*,  
2440 15(15), 5379. <https://doi.org/10.3390/ma15155379>
- 2441 Tran, H. N., Tomul, F., Thi Hoang Ha, N., Nguyen, D. T., Lima, E. C., Le, G. T., Chang, C.-T., Masindi,  
2442 V., & Woo, S. H. (2020). Innovative spherical biochar for pharmaceutical removal from water:  
2443 Insight into adsorption mechanism. *Journal of Hazardous Materials*, 394, 122255.  
2444 <https://doi.org/10.1016/j.jhazmat.2020.122255>
- 2445 Uddin, M. J., Ampiauw, R. E., & Lee, W. (2021). Adsorptive removal of dyes from wastewater using a  
2446 metal-organic framework: A review. *Chemosphere*, 284, 131314.  
2447 <https://doi.org/10.1016/j.chemosphere.2021.131314>



- 2448 Varsihini C, J. S., Das, D., & Das, N. (2014). Optimization of parameters for cerium(III) biosorption onto  
2449 biowaste materials of animal and plant origin using 5-level Box-Behnken design: Equilibrium,  
2450 kinetic, thermodynamic and regeneration studies. *Journal of Rare Earths*, 32(8), 745–758.  
2451 [https://doi.org/10.1016/S1002-0721\(14\)60136-8](https://doi.org/10.1016/S1002-0721(14)60136-8)
- 2452 Vo, A. T., Nguyen, V. P., Ouakouak, A., Nieva, A., Doma, B. T., Tran, H. N., & Chao, H.-P. (2019).  
2453 Efficient Removal of Cr(VI) from Water by Biochar and Activated Carbon Prepared through  
2454 Hydrothermal Carbonization and Pyrolysis: Adsorption-Coupled Reduction Mechanism. *Water*,  
2455 11(6), 1164. <https://doi.org/10.3390/w11061164>
- 2456 Vunain, E., Kenneth, D., & Biswick, T. (2017). Synthesis and characterization of low-cost activated carbon  
2457 prepared from Malawian baobab fruit shells by H<sub>3</sub>PO<sub>4</sub> activation for removal of Cu(II) ions:  
2458 Equilibrium and kinetics studies. *Applied Water Science*, 7(8), 4301–4319.  
2459 <https://doi.org/10.1007/s13201-017-0573-x>
- 2460 Wan, C., Shen, G. Q., & Choi, S. (2019). Waste Management Strategies for Sustainable Development. In  
2461 W. Leal Filho (Ed.), *Encyclopedia of Sustainability in Higher Education* (pp. 1–9). Springer  
2462 International Publishing. [https://doi.org/10.1007/978-3-319-63951-2\\_194-1](https://doi.org/10.1007/978-3-319-63951-2_194-1)
- 2463 Wang, C., Liu, H., Sun, P., Cai, J., Sun, M., Xie, H., & Shen, G. (2023). A novel peroxymonosulfate  
2464 activation process by single-atom iron catalyst from waste biomass for efficient singlet oxygen-  
2465 mediated degradation of organic pollutants. *Journal of Hazardous Materials*, 453, 131333.  
2466 <https://doi.org/10.1016/j.jhazmat.2023.131333>
- 2467 Wang, W., & Chen, M. (2022). Catalytic degradation of sulfamethoxazole by peroxymonosulfate activation  
2468 system composed of nitrogen-doped biochar from pomelo peel: Important roles of defects and  
2469 nitrogen, and detoxification of intermediates. *Journal of Colloid and Interface Science*, 613, 57–  
2470 70. <https://doi.org/10.1016/j.jcis.2022.01.006>
- 2471 Wang, Y., Peng, C., Padilla-Ortega, E., Robledo-Cabrera, A., & López-Valdivieso, A. (2020). Cr(VI)  
2472 adsorption on activated carbon: Mechanisms, modeling and limitations in water treatment. *Journal*  
2473 *of Environmental Chemical Engineering*, 8(4), 104031. <https://doi.org/10.1016/j.jece.2020.104031>



- 2474 Wang, L., Chang, Y., Liu, Q. (2019). Fate and distribution of nutrients and heavy metals during  
2475 hydrothermal carbonization of sewage sludge with implication to land application. *Journal of*  
2476 *Cleaner Production*, 225, 972-983. <https://doi.org/10.1016/j.jclepro.2019.03.347>
- 2477 Wu, H., Feng, Q., Lu, P., Chen, M., & Yang, H. (2018). Degradation mechanisms of cefotaxime using  
2478 biochar supported Co/Fe bimetallic nanoparticles. *Environmental Science: Water Research &*  
2479 *Technology*, 4(7), 964–975. <https://doi.org/10.1039/C8EW00163D>
- 2480 Wu, H., Feng, Q., Yang, H., Alam, E., Gao, B., & Gu, D. (2017). Modified biochar supported Ag/Fe  
2481 nanoparticles used for removal of cephalexin in solution: Characterization, kinetics and  
2482 mechanisms. *Colloids and Surfaces A: Physicochemical and Engineering Aspects*, 517, 63–71.  
2483 <https://doi.org/10.1016/j.colsurfa.2017.01.005>
- 2484 Wu, S., Shi, W., Li, K., Cai, J., & Chen, L. (2022). Recent advances on sustainable bio-based materials for  
2485 water treatment: Fabrication, modification and application. *Journal of Environmental Chemical*  
2486 *Engineering*, 10(6), 108921. <https://doi.org/10.1016/j.jece.2022.108921>
- 2487 Xiao, K., Liang, F., Liang, J., Xu, W., Liu, Z., Chen, B., Jiang, X., Wu, X., Xu, J., Beiyuan, J., & Wang, H.  
2488 (2022). Magnetic bimetallic Fe, Ce-embedded N-enriched porous biochar for peroxydisulfate  
2489 activation in metronidazole degradation: Applications, mechanism insight and toxicity evaluation.  
2490 *Chemical Engineering Journal*, 433, 134387. <https://doi.org/10.1016/j.cej.2021.134387>
- 2491 Xing, X., Jiang, W., Li, S., Zhang, X., & Wang, W. (2019). Preparation and analysis of straw activated  
2492 carbon synergetic catalyzed by ZnCl<sub>2</sub>-H<sub>3</sub>PO<sub>4</sub> through hydrothermal carbonization combined with  
2493 ultrasonic assisted immersion pyrolysis. *Waste Management*, 89, 64–72.  
2494 <https://doi.org/10.1016/j.wasman.2019.04.002>
- 2495 Xiong, M., Yan, J., Fan, G., Liu, Y., Chai, B., Wang, C., & Song, G. (2022). Built-in electric field mediated  
2496 peroxydisulfate activation over biochar supported-Co<sub>3</sub>O<sub>4</sub> catalyst for tetracycline  
2497 hydrochloride degradation. *Chemical Engineering Journal*, 444, 136589.  
2498 <https://doi.org/10.1016/j.cej.2022.136589>



- 2499 Xu, L., Wu, C., Liu, P., Bai, X., Du, X., Jin, P., Yang, L., Jin, X., Shi, X., & Wang, Y. (2020).  
2500 Peroxymonosulfate activation by nitrogen-doped biochar from sawdust for the efficient  
2501 degradation of organic pollutants. *Chemical Engineering Journal*, 387, 124065.  
2502 <https://doi.org/10.1016/j.cej.2020.124065>
- 2503 Xu, L., Ye, Z., Pan, Y., Zhang, Y., Gong, H., Mei, X., Qiao, W., & Gan, L. (2023). Effect of lignocellulosic  
2504 biomass composition on the performance of biochar for the activation of peroxymonosulfate to  
2505 degrade diclofenac. *Separation and Purification Technology*, 311, 123312.  
2506 <https://doi.org/10.1016/j.seppur.2023.123312>
- 2507 Yaashikaa, P. R., Kumar, P. S., Varjani, S., & Saravanan, A. (2020). A critical review on the biochar  
2508 production techniques, characterization, stability and applications for circular bioeconomy.  
2509 *Biotechnology Reports*, 28, e00570. <https://doi.org/10.1016/j.btre.2020.e00570>
- 2510 Yang, Q., Wu, P., Liu, J., Rehman, S., Ahmed, Z., Ruan, B., & Zhu, N. (2020). Batch interaction of  
2511 emerging tetracycline contaminant with novel phosphoric acid activated corn straw porous carbon:  
2512 Adsorption rate and nature of mechanism. *Environmental Research*, 181, 108899.  
2513 <https://doi.org/10.1016/j.envres.2019.108899>
- 2514 Yang, X., Wang, L., Shao, X., Tong, J., Zhou, J., Feng, Y., Chen, R., Yang, Q., Han, Y., Yang, X., Ding,  
2515 F., Meng, Q., Yu, J., Zimmerman, A. R., & Gao, B. (2022). Characteristics and aqueous dye  
2516 removal ability of novel biosorbents derived from acidic and alkaline one-step ball milling of  
2517 hickory wood. *Chemosphere*, 309, 136610. <https://doi.org/10.1016/j.chemosphere.2022.136610>
- 2518 Yang, Y., Xu, X., Zhang, S., Wang, G., Yang, Z., Cheng, Z., Xian, J., Li, T., Pu, Y., Zhou, W., & Xiang,  
2519 G. (2022). Two novel and efficient plant composites for the degradation of oxytetracycline:  
2520 Nanoscale ferrous sulphide supported on rape straw waste. *Environmental Science and Pollution*  
2521 *Research*, 29(42), 63545–63559. <https://doi.org/10.1007/s11356-022-20063-x>
- 2522 Yang, Y., Zhu, J., Zeng, Q., Zeng, X., Zhang, G., & Niu, Y. (2023). Enhanced activation of peroxydisulfate  
2523 by regulating pyrolysis temperature of biochar supported nZVI for the degradation of



- 2524 oxytetracycline. *Journal of the Taiwan Institute of Chemical Engineers*, 145, 104775.
- 2525 <https://doi.org/10.1016/j.jtice.2023.104775>
- 2526 Yang, Z., An, Q., Deng, S., Xu, B., Li, Z., Deng, S., Zhao, B., & Ye, Z. (2023). Efficient activation of
- 2527 peroxydisulfate by modified red mud biochar derived from waste corn straw for levofloxacin
- 2528 degradation: Efficiencies and mechanisms. *Journal of Environmental Chemical Engineering*,
- 2529 11(6), 111609. <https://doi.org/10.1016/j.jece.2023.111609>
- 2530 Yang, Z., Li, Y., Zhang, X., Cui, X., He, S., Liang, H., & Ding, A. (2020). Sludge activated carbon-based
- 2531 CoFe<sub>2</sub>O<sub>4</sub>-SAC nanocomposites used as heterogeneous catalysts for degrading antibiotic
- 2532 norfloxacin through activating peroxymonosulfate. *Chemical Engineering Journal*, 384, 123319.
- 2533 <https://doi.org/10.1016/j.cej.2019.123319>
- 2534 Yao, Y., Hu, H., Zheng, H., Hu, H., Tang, Y., Liu, X., & Wang, S. (2022). Nonprecious bimetallic Fe, Mo-
- 2535 embedded N-enriched porous biochar for efficient oxidation of aqueous organic contaminants.
- 2536 *Journal of Hazardous Materials*, 422, 126776. <https://doi.org/10.1016/j.jhazmat.2021.126776>
- 2537 Yardımcı, B., & Kanmaz, N. (2023). An effective-green strategy of methylene blue adsorption: Sustainable
- 2538 and low-cost waste cinnamon bark biomass enhanced via MnO<sub>2</sub>. *Journal of Environmental*
- 2539 *Chemical Engineering*, 11(3), 110254. <https://doi.org/10.1016/j.jece.2023.110254>
- 2540 Ye, H., Zhu, Q., & Du, D. (2010). Adsorptive removal of Cd(II) from aqueous solution using natural and
- 2541 modified rice husk. *Bioresource Technology*, 101(14), 5175–5179.
- 2542 <https://doi.org/10.1016/j.biortech.2010.02.027>
- 2543 Yi, Y., Wu, J., Wei, Y., Fang, Z., & Tsang, E. P. (2017). The key role of biochar in the rapid removal of
- 2544 decabromodiphenyl ether from aqueous solution by biochar-supported Ni/Fe bimetallic
- 2545 nanoparticles. *Journal of Nanoparticle Research*, 19(7), 245. [https://doi.org/10.1007/s11051-017-](https://doi.org/10.1007/s11051-017-3927-2)
- 2546 [3927-2](https://doi.org/10.1007/s11051-017-3927-2)
- 2547 Yurtay, A., & Kılıç, M. (2023). Biomass-based activated carbon by flash heating as a novel preparation
- 2548 route and its application in high efficiency adsorption of metronidazole. *Diamond and Related*
- 2549 *Materials*, 131, 109603. <https://doi.org/10.1016/j.diamond.2022.109603>



- 2550 Yusop, M. F. M., Ahmad, M. A., Rosli, N. A., & Manaf, M. E. A. (2021). Adsorption of cationic methylene  
2551 blue dye using microwave-assisted activated carbon derived from acacia wood: Optimization and  
2552 batch studies. *Arabian Journal of Chemistry*, *14*(6), 103122.  
2553 <https://doi.org/10.1016/j.arabjc.2021.103122>
- 2554 Zeng, S., Li, K., Xu, X., Zhang, J., & Xue, Y. (2023). Efficiently catalytic degradation of tetracycline via  
2555 persulfate activation with plant-based biochars: Insight into endogenous mineral self-template  
2556 effect and pyrolysis catalysis. *Chemosphere*, *337*, 139309.  
2557 <https://doi.org/10.1016/j.chemosphere.2023.139309>
- 2558 Zhang, B., & Wang, D. (2019). Preparation of Biomass Activated Carbon Supported Nanoscale Zero-  
2559 Valent Iron (Nzvi) and Its Application in Decolorization of Methyl Orange from Aqueous Solution.  
2560 *Water*, *11*(8), 1671. <https://doi.org/10.3390/w11081671>
- 2561 Zhang, H., Ruan, Y., Liang, A., Shih, K., Diao, Z., Su, M., Hou, L., Chen, D., Lu, H., & Kong, L. (2019).  
2562 Carbothermal reduction for preparing nZVI/BC to extract uranium: Insight into the iron species  
2563 dependent uranium adsorption behavior. *Journal of Cleaner Production*, *239*, 117873.  
2564 <https://doi.org/10.1016/j.jclepro.2019.117873>
- 2565 Zhang, L., Tu, L., Liang, Y., Chen, Q., Li, Z., Li, C., Wang, Z., & Li, W. (2018). Coconut-based activated  
2566 carbon fibers for efficient adsorption of various organic dyes. *RSC Advances*, *8*(74), 42280–42291.  
2567 <https://doi.org/10.1039/C8RA08990F>
- 2568 Zhang, P., Duan, W., Peng, H., Pan, B., & Xing, B. (2022). Functional Biochar and Its Balanced Design.  
2569 *ACS Environmental Au*, *2*(2), 115–127. <https://doi.org/10.1021/acsenvironau.1c00032>
- 2570 Zhang, P., Li, Y., Cao, Y., & Han, L. (2019). Characteristics of tetracycline adsorption by cow manure  
2571 biochar prepared at different pyrolysis temperatures. *Bioresource Technology*, *285*, 121348.  
2572 <https://doi.org/10.1016/j.biortech.2019.121348>
- 2573 Zhang, P., Zhang, P. J., Feng, S., Li, H., Li, J., Du, W., Duan, W., Li, X., Zhang, C., Li, H., Song, S., &  
2574 Pan, B. (2023). The mechanism of p-nitrophenol degradation by dissolved organic matter derived



- 2575 from biochar. *Science of The Total Environment*, 868, 161693.  
2576 <https://doi.org/10.1016/j.scitotenv.2023.161693>
- 2577 Zhang, X., Sun, P., Wei, K., Huang, X., & Zhang, X. (2020). Enhanced H<sub>2</sub>O<sub>2</sub> activation and  
2578 sulfamethoxazole degradation by Fe-impregnated biochar. *Chemical Engineering Journal*, 385,  
2579 123921. <https://doi.org/10.1016/j.cej.2019.123921>
- 2580 Zhang, Y., Cheng, L., & Ji, Y. (2022). A novel amorphous porous biochar for adsorption of antibiotics:  
2581 Adsorption mechanism analysis via experiment coupled with theoretical calculations. *Chemical*  
2582 *Engineering Research and Design*, 186, 362–373. <https://doi.org/10.1016/j.cherd.2022.07.049>
- 2583 Zhao, J., Sun, Y., Zhang, Y., Zhang, B.-T., Yin, M., & Chen, L. (2021). Heterogeneous activation of  
2584 persulfate by activated carbon supported iron for efficient amoxicillin degradation. *Environmental*  
2585 *Technology & Innovation*, 21, 101259. <https://doi.org/10.1016/j.eti.2020.101259>
- 2586 Zhong, Y., Wang, Y., Ji, Y., Zhang, X., & Wang, X. (2023). Biomass carbon-based composites for  
2587 adsorption/photocatalysis degradation of VOCs: A comprehensive review. *Colloid and Interface*  
2588 *Science Communications*, 57, 100749. <https://doi.org/10.1016/j.colcom.2023.100749>
- 2589 Zhou, Q., Qin, L., Liu, H., Zhao, D., Yang, M., Sun, B., Gao, X., & Jiang, H. (2024). Microwave assisted  
2590 biomass derived carbon aerogel for highly efficient oxytetracycline hydrochloride degradation:  
2591 Singlet oxygen mechanism and C vacancies accelerated electron transfer. *Chemical Engineering*  
2592 *Journal*, 487, 150370. <https://doi.org/10.1016/j.cej.2024.150370>
- 2593 Zhou, X., Wang, Y., Liu, H., Zhang, Y., Fan, Y., Mo, S., Li, H., Wang, J., Lin, H. (2023). Novel amino-  
2594 modified bamboo-derived biochar-supported nano-zero-valent iron (AMBBC-nZVI) composite  
2595 for efficient Cr (VI) removal from aqueous solution. *Environmental Science and Pollution*  
2596 *Research*, 30(57), 119935-119946. <https://doi.org/10.1007/s11356-023-30351-9>
- 2597 Zhou, Y., Zhang, L., & Cheng, Z. (2015). Removal of organic pollutants from aqueous solution using  
2598 agricultural wastes: A review. *Journal of Molecular Liquids*, 212, 739–762.  
2599 <https://doi.org/10.1016/j.molliq.2015.10.023>
- 2600



2601  
2602  
2603  
2604

Open Access Article. Published on 09 October 2025. Downloaded on 10/10/2025 21:44:58.  
This article is licensed under a Creative Commons Attribution 3.0 Unported Licence.



No new data were created or analyzed in this study. Data sharing is not applicable to this article as it is a review of existing literature.

